Development of Silicon Oxide as Electron Selective Passivating Contact Layer in Silicon Heterojunction Solar Cells

Wessel Willem Andries van Ekeren

Delft
University of
Technology

Challenge the future

Development of Silicon Oxide as Electron Selective Passivating Contact Layer in Silicon Heterojunction Solar Cells

by

Wessel Willem Andries van Ekeren

in fulfilment of the requirements for the degree of

Master of Science
in Materials Science and Engineering

at the Delft University of Technology,
to be defended publicly on Tuesday May 22, 2018 at 14:00.

Daily Supervisor:	Dr. P.C.P. Bronsveld,	ECN-Solar Energy
Thesis committee:	Dr. A.J. Böttger,	TU Delft
	Dr. Y. Gonzalez-Garcia,	TU Delft
	Prof. A.W. Weeber,	TU Delft & ECN-Solar Energy

Abstract

Within the photovoltaic industry, a lot of research is done in order to minimize losses which are created during the conversion of solar light to electrical energy. In a crystalline silicon solar cell light has to pass through several layers before it enters the silicon wafer where the electron-hole pairs are generated. As one can imagine, if more light reaches the active layer, more electron-hole pairs can be generated. It is highly desired that only one layer, the active layer, is absorbing photons of the solar spectrum. The active layers at the sunny side of the silicon wafer should be highly transparent for solar light. In addition to being transparent, these layers should be conductive to extract the generated charge carriers to the metal contacts. Current layers applied at the sunny side are not optimally transparent, so it is still possible to increase the efficiencies in the crystalline silicon solar cells. In this study, doped silicon oxide layers have been explored as a potential more transparent layer for passivation of both the silicon surface and the metal contacts. Two routes for the fabrication of doped silicon oxide layers were investigated: post-oxidation of doped polycrystalline silicon layers and post-doping of in-situ grown silicon oxide layers. To characterize this new type of material, several different measurement techniques have been applied to improve our understanding of Low-Pressure Chemical Vapor Deposition deposited silicon oxide passivating contact layers. It was found that the structure and composition of the layers is very different for these different routes. However, very good and stable surface passivation (minority carrier lifetime of >3 ms) can be achieved with both types of silicon oxide layers. Also, sheet resistance measurements have indicated that phosphorus doping in silicon oxides is possible. For better insight into the electrical properties of these layers, further testing in electronic test structures is advised.

Wessel Willem Andries van Ekeren
Delft, May 2018

Nomenclature

Abbreviation	
a-Si	Amorphous silicon
CZ	Czochralski
E_C	Conduction band energy
ECV	Electrochemical Capacitance-Voltage
EDX	Energy Dispersive X-ray
E_G	Bandgap energy
E_F	Fermi level energy
E_V	Valence band energy
FPP	Four Point Probe
FTIR	Fourier Transform Infrared Spectroscopy
FZ	Float Zone
LPCVD	Low-Pressure Chemical Vapor Deposition
n-type	Negative charged semiconductor
SiN_x	Silicon nitride
PECVD	Plasma Enhanced Chemical Vapor Deposition
PERC	Passivated Emitter and Rear Cell
PERL	Passivated Emitter and Rear Locally diffused
PL	Photoluminescence
poly-Si	Polycrystalline silicon
PSG	Phosphor silicate glass
p-type	Postive charged semiconductor
PV	Photovoltaic
QSS	Quasi-Steady-State
QSSPC	Quasi-Steady-State Photoconductance
R_S	Sheet resistance
SE	Spectroscopic Ellipsometry
SEM	Scanning Electron Microscope
Si	Silicon
SiO_2	Silicon dioxide
SiO_x	Substoichiometric silicon oxide
SRH	Shockley-Read-Hall
τ_{eff}	Minority carrier lifetime
XPS	X-ray Photoelectron Spectroscopy
XRD	X-Ray Diffraction

List of Figures

List of Tables

Contents

1

Introduction

One of the aims of the Paris Agreement is to limit global temperature rise well below 2 °C, with efforts to limit the warming to 1.5 °C [1]. In the road towards sucessful realization of this agreement, all types of renewable energy sources need to become cheaper and more efficient. Solar energy has already become the cheapest and fastest-growing energy resource on earth [2]. Its future potential is still huge, because every hour the sun radiates more energy onto earth than the entire world uses in one year and nowadays only 0.1% of this amount is being used. The photovoltaic (PV) industry is one of the most promising emerging technologies. Due to the worldwide growing interest in renewable energy, and to compete with other renewable energy sources, the photovoltaic industry strives to develop the most efficient and cheapest solar cells. The majority of the silicon solar cells which are on the market nowadays are based on p-type electron selective contacts. Despite that at the moment the mainstream PV technology still relies on p-type crystalline silicon wafers, a gradual but significant shift can be observed towards n-type silicon PV technology in the near future [2]. Because of its higher efficiency and lower price per Watt-peak potential many PV companies are currently adopting n-type technology as the next step, or are already producing bifacial n-type solar cells. These companies ask for ready-to-implement and cost-effective improvements on their n-type technology. In order to fulfill their requirements and to develop high efficiency solar cells a considerable amount of research is done. Most studies are focused on reducing the amount of optical and recombination losses [3] [4] [5]. Especially, reduction of recombination at metal contacts plays a major role towards the successful realization of high-efficiency c-Si solar cells. For this reason, there is an increasing interest in the field of so-called passivating contacts. In a passivating contact, a sheet is placed below the metal contacts to reduce recombination at the silicon-metal interface. The sheet needs to be electrically conductive for the type of charge carrier (electron or hole) to be collected at the contact. Traditional solutions are based on **p**assivated **e**mitter and **r**ear **c**ontact (PERC), or related architectures such as **p**assivated **e**mitter and **r**ear **l**ocally diffused (PERL)[6] [7]. In figure 1.1 a schematic drawing of an industrial widely produced PERC solar cell is shown. This PERC solar cell is based on doped poly-Si passivating contacts, which has excellent performance when employed as rear contact. The major drawback of this structure is the parasitic absorption that takes place in the poly-Si layer at the front side. Consequently, if more transparent and carrier selective materials can be developed, this material can reduce losses and replace both front side and back side emitters which will further increase the solar cell efficiency.

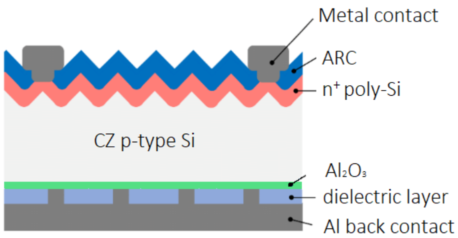

Figure 1.1: Schematic of the passivated emitted rear cell structure is shown. Image adapted from [6].

Research in the field of passivating contacts has so far been focused on amorphous silicon (a-Si) or doped polysilicon (poly-Si, p-type or n-type), in combination with SiO_x or a-Si:H oxide. Such stacks of doped and passivating layers provide excellent surface passivation, however, they also absorb photons of wavelengths within the spectral response range of crystalline silicon. Incoming photons that are not absorbed in the silicon wafer do not contribute to the current generated by the solar cell; therefore, the need to improve the transmission of passivating contact layers is high. The best known passivation technique is based on an amorphous to crystalline heterojunction structure. By implementation of a stack of intrinsic and doped hydrogenated amorphous silicon (a-Si:H) layers at the interface of the c-Si wafer and the metal contact, a so called heterojunction intrinsic thin film (HIT) structure is formed [8]. Recently, researchers of Kaneka achieved a new world-record efficiency of 26.7% with these type of solar cells [9] (enhancement of 0.4%, previous record was 26.3% by Yoshikawa et al. [10]). Although this conversion efficiency is close to the maximum theoretical efficiency of 29.43%, both contacts were placed at the rear for this record cell to reduce the parasitic absorption in these layers, which requires very complex patterning methods that are not cost-effective to introduce in PV industry. The efficiency can still be increased by using more transparent passivating layers and by reducing recombination losses at metal contacts. Recently, the development of doped silicon oxides to replace both the passivating and the selective interface layer received a lot of attention [11] [12] [13]. Due to its tunable optical bandgap (a larger bandgap means enhanced transparency) and tunable refractive index it can be applied in silicon solar cells as window layer, intermediate reflector or back reflector. Although devices fabricated with a SiO_x passivating contact layer are showing promising efficiencies, the material properties of these layers are not yet very well understood.

Doped poly-SiO_x is more transparent than poly-Si or a-Si:H for the relevant part of the solar spectrum and can also be produced using LPCVD equipment that is readily available in PV industry. Other materials, such as MoO_x (molybdenum oxide) [14] and SiC (silicon carbide) [15], also show great potential as passivating contact layers, but industrial equipment for manufacturing of such layers is not yet readily available.

This work focuses on the development of SiO_x layers that can reduce metal contact recombination and minimizes optical losses in c-Si solar cells. Two approaches for fabrication of LPCVD SiO_x layers will be investigated. These methods will be referred to as post-oxidation and post-doping, and will be explained in more detail in the methodology chapter 3.

1.1. Motivation to Develop Doped Silicon Oxide Layers

Silicon oxide based passivating contact layers in bifacial solar cells are getting increased attention in the development towards high efficient solar cells. Previous studies have shown that the application of silicon oxides result in higher current output, because of an increase in optical bandgap and decrease of refractive index [11] [16]. The optical bandgap is a measure of the ease of electron excitation from the valence to the conduction band. The size of the atoms and the number of protons in the atom are the primary predictors of the strength and layout of the bandgaps. Materials consisting of small atoms and strong, electronegative atomic bonds are associated with wide bandgaps. More specifically, the bond energy determines the width of the bonding and anti-bonding states. The more tightly atoms are bonded to one another, the more difficult it becomes to excite an electron in the material. Upon increase in bond-energy, the bonding and anti-bonding states widen up and thus increases the bandgap (enhanced optical transparency). The Si–O bond energy in SiO_2 is 4.8 eV, whereas the Si–Si bond energy in crystalline Si is 2.3 eV [17] [18]. When many Si–O bonds are formed the respective bonding and antibonding states widen. The optical bandgap of intrinsic silicon is about 1.12 eV and that of SiO_2 is about 9 eV [19] [20]. So any substoichiomtetric oxide (SiO_x) will have an optical gap within the range 1.7 eV to 10 eV, depending on the oxygen content. The optical bandgap increases monotonically with the increase of oxygen content [11]. To summarize, silicon oxides have a larger bandgap than silicon which reduces the amount of parasitic absorption. Because the bandgap of SiO_x is larger than the bandgap of poly-Si, it becomes interesting to investigate the replacement of doped poly-Si with doped SiO_x layers.

Silicon oxide layers have been widely developed by LPCVD, but were not yet optimized for PV. In solar cell research the most commonly used technique to develop these layers is based on PECVD. However, PECVD is not yet industrially applied due to production limitations (low throughput, large downtime and use of toxic gases). Since large quantities of solar cells can be processed by LPCVD, it becomes interesting for industry to investigate the development of SiO_x layers by LPCVD. Furthermore, studies about adding dopants to the silicon oxide layers are currently gaining interest, but the doping process is still not very well understood. The purpose of this research is to investigate possible routes of LPCVD developed doped SiO_x layers.

The silicon oxide layer needs to be selective, passivating and conductive in the lateral direction. In the most ideal case, the silicon oxide layer has a refractive index similar to that of SiN_x (2.1) [21], so that it can also function as anti-reflective coating. The biggest challenge is to make the silicon oxide layer conductive in the lateral direction. If this challenge is not being met, extra in-diffusion needs to compensate for increased resistance or a transparent conductive oxide needs to be placed on top of the silicon oxide layer can enhance lateral conductivity. In figure 1.2 a schematic is shown which visualizes the different functions.

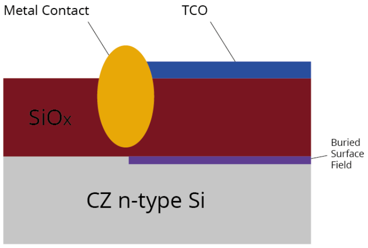

Figure 1.2: Schematic of the application of SiO_x layer as passivating contact. The schematic also shows which layers need to be added if the SiO_x does not fulfil the sheet resistance requirement.

The primary objective of this study is to investigate the development of doped SiO_x passivating contact layers deposited by LPCVD. The secondary objectives are set to realize the primary objective, and are listed below:

- Is post-oxidation, either by dry or wet oxidation, of phosphorus doped poly-Si a successful method to produce doped SiO_x layers?
  - Determine the quality of the layer for application in a passivating contact and discuss most relevant material properties contributing this quality.
- Is post-doping of in situ oxidised SiO_x layers a successful method to produce doped SiO_x layers?
  - Determine the quality of the layer for application in a passivating contact and discuss most relevant material properties contributing this quality.
- Which route, post-oxidation or post-doping, leads to the the most promising SiO_x passivating contact layer?

1.1.1. Outline of Thesis

The goal of the work in this thesis is to investigate two different routes for producing doped SiO_x layers and to determine the applicability of the resulting layers. In seven chapters the reader will be provided with the findings of this study. The outline of the coming chapters of the thesis is given below:

Chapter 2 provides the reader with background information required to understand the research and thesis.

Chapter 3 describes the fabrication process of the symmetrical samples and gives an overview of the characterization techniques used to determine the electric and structural properties of the developed SiO_x layers.

Chapter 4 discusses the results of doped SiO_x layers developed by dry and wet post-oxidation of poly-Si.

Chapter 5 discusses the results of doped SiO_x layers developed by in-situ oxidation and post-doping.

Chapter 6 reviews the highlights of this thesis, draws general conclusions and presents an outlook for future research.

2

Background

This chapter will provide the reader with all required (state-of-the-art) knowledge about silicon solar cells in order to understand the performed/executed research. Also, the motivation behind this research will be explained.

2.1. Working Principle of a Crystalline Silicon Solar Cells

Before an accurate description of the working principle of solar cells is given, the reader will be provided with a brief description of semiconductor physics. The behaviour of semiconductor materials can be described according to solid state physics. This theory postulates that electrons within a solid are arranged according to an electronic band structure. The band structure describes the energy levels which may, or may not be occupied by electrons. The allowed energy levels are known as energy bands and the prohibited energy ranges are known as band gaps. Two types of energy bands can be distinguished: the conduction band and the valence band. The difference in energy of electrons in the conduction and valence band is the bandgap energy, $E_G = E_C - E_V$. The distribution of electrons within these energy bands depends on the type of material (i.e. semiconductor, insulator or conductor). The last crucial energy level in the understanding of electrical properties of solid materials, is the Fermi energy (E_F). This level is defined as such that at 0 K all energy levels are filled up to E_F, but no electrons can exceed the E_F. If an atom is isolated, the electrons have well defined discrete energy levels. However, when atoms are brought together to form molecules, these discrete energy levels split up into multiple energy levels grouped as bands. This change of electron's discrete energy levels when atoms are brought together is visualized in figure 2.1. It should be noticed that the energy bands are separated from each other by an energy gap.

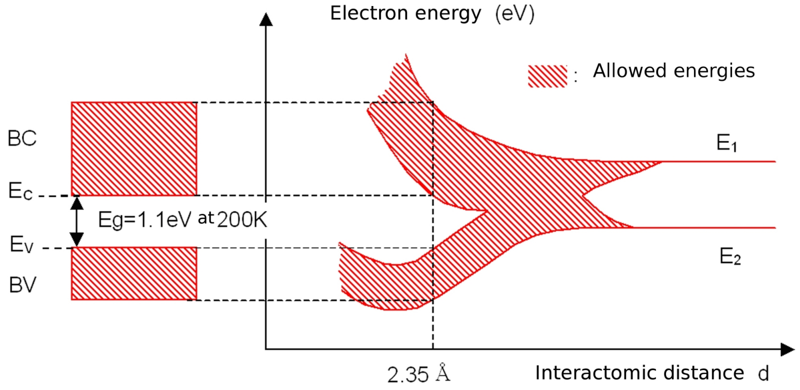

Figure 2.1: Schematic energy bands for electrons in a silicon crystal. On the y-axis the electron energy is plotted, whereas on the x-axis the interatomic distance is shown. Image taken from [22].

The energy band theory described above can be applied to three different types of materials. In figure 2.2 a schematic view of the band structures of conductors, insulators and semiconductors is shown. Figure 2.2 shows that no bandgap is present for metals, a moderate bandgap is present for semiconductors and a large bandgap is present for insulators. In materials where no or a negligible bandgap is present (the valence and conduction bands overlap) free carriers move freely through the crystal lattice. These materials are known as metals and are the best conductors compared to semiconductors and insulators. Large bandgap materials, also known as insulators, require the largest amount of energy to excite electrons from the valence band to the conduction band and thus have the highest electrical resistance to current flow. Semiconductors have a moderate bandgap, in which a small amount of energy supplied to the material can generate free carriers, altering the conductivity of the material significantly (i.e. conductivity will increase).

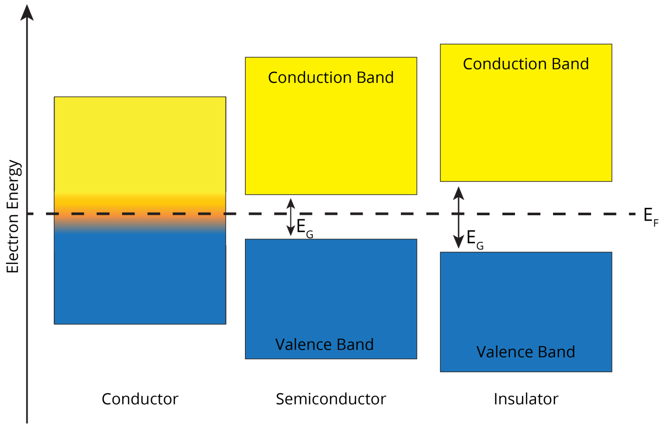

Figure 2.2: Schematic overview of energy band diagram of conductor, semiconductor and insulator [23]. E_G is indicating the forbidden energy range and known as the bandgap energy. For insulators the bandgap is > 2 eV, for semiconductors this value is 0 eV < 2 eV and for conductors the bandgap is absent. E_C and E_V are both continuous energy levels and are respectively known as conduction band energy and valence band energy. The position of E_F is dependent on the doping level in the semiconductor. For intrinsic semiconductors E_F lies in the middle, whereas for n- and p-type the Fermi level is shifted towards the conduction band and valence band, respectively.

The only group of materials which responds to solar light, in terms of electrical energy generation, are semiconductors. The band gap in insulators is too large for (sunlight) photons to excite electrons from the valence to the conduction band. In conductors free electrons always exist, but they can move randomly and hence they cannot contribute to current (movement of electrons in a specific direction is required for current). As only semiconductors can convert solar energy, from now on we will focus on the behaviour of semiconductors. Two types of semiconductors can be distinguished: direct and indirect semiconductors. Direct and indirect semiconductors differ in terms of alignment of the maximum of the valence and minimum of the conduction band in momentum space. If the maximum of the valence band and the minimum of the conduction band occur at the same crystal momentum, an electron can be excited from the valence band to the conduction band without applying momentum. Semiconductors in which this type of valence and conduction band alignment occurs are known as a direct bandgap materials. Examples of direct bandgap materials are gallium arsenide and indium arsenide, also known as III-V materials.

However, if the maximum energy of the valence band and minimum of the conduction band occur at different values of the wave vector, an electron needs to change its momentum. Materials with a shifted valence and conduction band maximum and minimum are known as indirect bandgap materials. In these type of materials both a photon and a phonon are required to excite electrons from the valence to the conduction band. Since in direct semiconductor materials only a photon can excite an electron into the conduction band and in indirect semiconductor materials both a photon and a phonon are needed, the former has a much higher absorption coefficient than the latter. Examples of indirect bandgap materials are silicon and germanium. It is important to realize the difference in electron excitement for direct and indirect bandgap materials when it comes to the types of losses, which will be explained in the next section 2.2.

By keeping the bandgap theory in mind, it is possible to understand the working principle of the solar cell. The working principle of solar cells is based on the photovoltaic effect, discovered in 1839 by French physicist Edmund Bequerel [24]. This effect can be divided into three simple processes:

1. Charge carrier generation upon photon absorption. If a photon with energy equal or larger than the material's bandgap energy (E_G) enters the solar cell, electrons in the absorbing material (shortly, absorber) will be excited from the valence band to the conduction band. The excited electrons can move through the material and will be referred to as free charge carriers. Inherent to the excitement of an electron to the conduction band, is the creation of a hole in the valence band. A so called electron-hole pair is generated (consisting of a negatively charged electron and a positively charged hole).

2. Separation of the generated charge carriers. The electron-hole pair that is generated after photon absorption has to be separated to create a potential difference over the two terminals of the solar cell. The separation of these carriers takes place by introduction of an electron collecting region and a hole collecting region at the surface of the absorber (the silicon wafer). A more detailed description of selectivity will be given in 2.3.

3. Charge carrier extraction by metal contacts. The last step involves the collection of the electrons at the metal contacts, where the charge carriers will enter an external circuit. After collection they can supply electric energy to an external system.

2.2. Loss Mechanisms

As explained above, a so-called electron-hole pair is generated when a photon is absorbed by the absorber. However, after this absorption various loss mechanisms reduce the solar cell's power output. These loss mechanisms can be divided into two categories, intrinsic and extrinsic losses. When referring to single-junction solar cells, intrinsic losses cannot be avoided whereas extrinsic losses are avoidable. The intrinsic losses are below bandgap losses($E_{Photon} < E_G$), thermalisation losses ($E_{Photon} > E_G$, holds for about 30% of photons), Carnot losses (thermal energy into electrical energy loss), Boltzmann losses (inequality of absorption and emission angles results in entropy generation because of expansion of photon modes). The extrinsic losses are theoretically avoidable, but always present in solar cells. Extrinsic losses are optical losses (parasitic absorption, reflection losses, shading) and electrical losses. Electrical losses can be divided into ohmic and recombination losses. The latter will be discussed in more detail, since it has a prominent role in the design of surface passivation layers. By careful design and material development, recombination losses can be minimized. Three types of charge carrier recombination should be distinguished: radiative recombination, Shockley-Read-Hall recombination and Auger recombination. In figure 2.3 these losses are shown.

Radiative recombination occurs is dominant in direct bandgap material, and as silicon is an indirect bandgap material this type of recombination will not be discussed in further detail.

Shockley-Read-Hall recombination occurs if charge carriers get trapped at ”trap” levels. For example, defects and impurities in the bulk or at the surface of the wafer can introduce energy states (trap states, E_T) becomes dominant when trap states are introduced, for example due to defects in the material. In this research the amount of dangling bonds at the silicon surface are reduced by hydrogenation, so that SRH reduces and minority carrier lifetime increases.

Auger recombination takes place if an electron recombines with a hole, whereby the released energy is transmitted to another electron that gets excited and relaxes the extra energy as phonon. This mechanism becomes dominant if high doping concentrations are reached, due to increased amount of free carriers in the conduction band. A carrier density of at least $10 \times 10^{17}\,\text{cm}^{-3}$ is required.

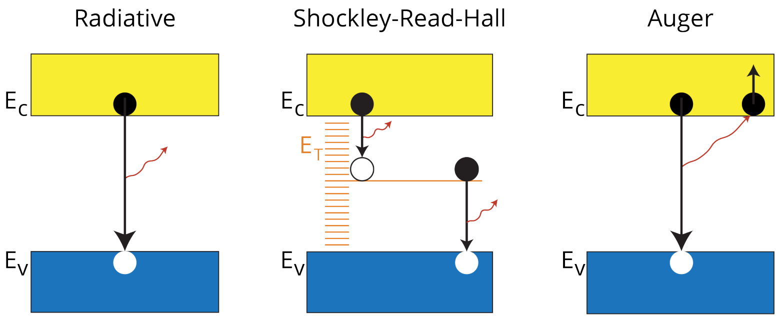

Figure 2.3: Schematic of radiative, SRH and auger recombination. E_T are trapping states introduced in the bulk or at the surface of the wafer. Please note that the electron that recombines with a hole in a trapping state during SRH is occurring separately from the electron recombining with a hole in the valence band.

The highest theoretical efficiency of a solar cell (the intrinsic limit) has been evaluated in 1961 when Shockley and Queisser developed their well known Shockley-Queisser limit [25]. The Shockley-Queisser limit describes the efficiency limit of a single junction solar cell assuming that the solar cell's temperature is 300 K, that the sun has a perfect black body spectrum with a surface temperature of 6000 K and that the only loss mechanism in the cells is radiative combination. With these assumptions the maximum efficiency was found to be 30% for an energy gap of 1.1 eV. However, today the solar cell efficiencies are reported at operating temperatures of 298.15 K and air mass 1.5 (AM1.5) which slightly changes the detailed balance limit of solar cells. In figure 2.4 the effect of these changes is shown, with also taking into account the non-radiative recombination paths (such as Auger recombination and Shockley-Read-Hall). The lower the number f_c, the higher the fraction of non-radiative recombination.

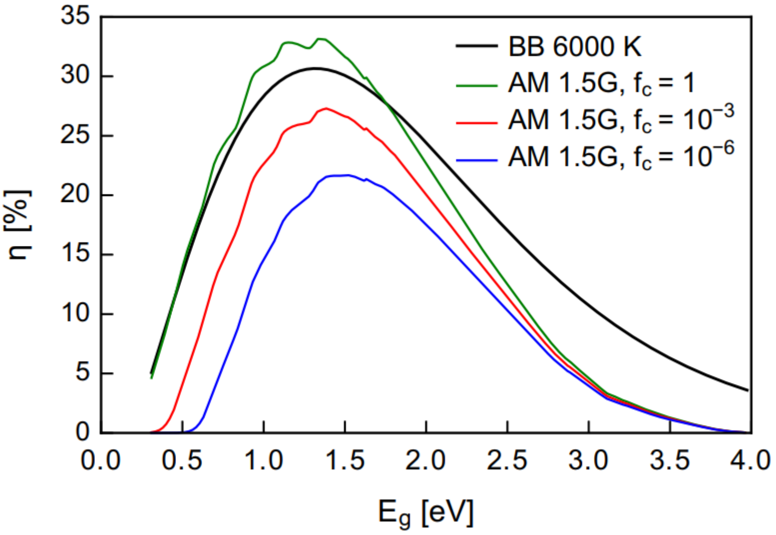

Figure 2.4: Graphical overview of solar cell efficiency versus bandgap. It includes the Shockley-Queisser limit (black curve) and updated Shockley-Queisser limits for standard test conditions (all colored curves) and taking into account non-radiative recombination (red and blue curves). The green curve represents detailed balance limit for standard test conditions. The ed curve shows limit with non-radiative recombination 10^3 times stronger than radiative recombination. Blue curve shows limit with non-radiative recombination 10^6 times stronger. Image taken from [26].

2.3. Selective Passivating Layers at Metal Contacts

In order to reduce the amount of losses in the solar cell, the recombination mechanisms have to be minimized. In this section the mechanism behind the reduction of recombination at the metal contacts will be addressed. Special attention will be given to passivation of the silicon substrate material (by electron and hole contacts) and the selectivity of electron and hole contacts. Passivation may be defined as the process which suppresses the surface recombination, caused by surface defects. The main purpose of passivation is to reduce recombination of photo-generated carriers at the silicon surface. The surface of a silicon substrate contains approximately 10×10^{14} cm^{-2} defects in the form of dangling bonds [27]. These dangling bonds introduce intermediate states within the bandgap which act as prominent sites for charge carriers to recombine. Passivation of these dangling bonds can reduce the amount of surface recombination. If the layers on both sides of the silicon absorber material are passivating properly, the minority carrier lifetime increases significantly and thus charge carriers will be successfully extracted from the absorber layer. In addition to being a passivating layer, the layer should be carrier-selective. A layer which is carrier selective transmits one type of carrier, while it blocks the other type of carrier. For example, the front layer should be electron-selective, whereas the back layer should be hole-selective. A layer which possesses both passivation and carrier-selectivity properties is referred to as a selective passivating contact.

2.3.1. Selectivity

Selectivity can be obtained by introducing a high concentration of dopants into the layer, thereby increasing the conductivity solely for one type of charge carrier. Depending on the type of dopant, i.e. donor (n-type) or acceptor (p-type), respectively electron or hole selective layers will be obtained. To illustrate the selectivity mechanism in n-type silicon, the energy band diagram of an electron selective passivating contact is shown in figure 2.5.

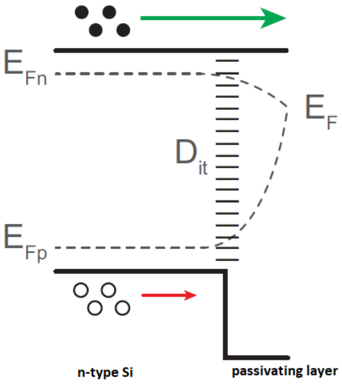

Figure 2.5: Schematic of idealized energy band diagram of an electron selective passivating contact layer (in practice the conduction band offset is not zero). D_{it} reperesent the defect density at the interface between the surface and the passivating layer. The green arrow represents the dominant electron flow and the red arrow represents the suppressed hole flow due to band offset through passivating layer with large band gap. Image taken from [28].

2.3.2. Passivation

Passivation mechanisms can be divided into two main techniques; (1) reduction of the surface defect density (chemical passivation) and/or (2) reduction of the electron or hole concentration at the surface (field-effect passivation).
To summarize, the prerequisites for useful selective passivating contact layers are as follows:

- Selective for one type of charge carrier. This can be obtained by doping with either donor or acceptor impurities.
- Reduce the amount of dangling bonds at the silicon surface and metal contact.
- Transparent layer for solar light.

A wide band gap material that significantly reduces the number of dangling bonds at the surface and can conduct one type of charge carrier (selectivity) has to be searched for.

2.4. Doping Mechanism in Semiconductors

There are three well known types of semiconductors; intrinsic, n-type and p-type. They are distinguished from one another by whether doping with active impurities is incorporated in the silicon crystal, and in the case of n-type and p-type, which types of impurities are used. Intrinsic semiconductors do not contain a measurable concentration of dopant atoms. Doping is the process in which impurities are added to an intrinsic semiconductor to locally increase the conductivity for one type of charge carrier.. The impurities that are added to the intrinsic material either supply or accept electrons, whereby respectively additional occupied states or vacant states are introduced. The dopants that introduce additional occupied states are referred to as donors and the dopants that introduce additional vacant states are referred to as acceptors.

This theory will now be applied to silicon, which is still the most widely used doped semiconductor (and also used in this thesis). N-type silicon is doped with pentavalent dopants that contain one valence electron more than silicon. Common donor impurities in silicon are the pentavelent atoms antimony, phosphorous and arsenic. Four covalent electrons form bonds with the surrounding silicon atoms, while the fifth valence electron is free to move. This electron is characterized with a higher energy level and requires much less energy to be excited from the valence to the conduction band compared to electrons of phosphorus sharing bonds with silicon. As the doped semiconductor has a surplus of **n**egative charge carriers (electrons) this type of semiconductor is named **n**-type. P-type silicon is doped with trivalent dopants, having one valence electron less than silicon. The most commonly used acceptor impurities are trivalent impurities such as boron, aluminium, gallium and indium. Three covalent electrons of these elements form bonds with silicon, which leaves one covalent electron of a neighbouring atom unbound. This unbound electron creates an electron vacancy, called a hole, in the silicon valence band. As the semiconductor doped with trivalent dopants has a surplus of **p**ositive charge carriers (holes), this type of semiconductor is named **p**-type. For clarity, since no charge is added to the total system, the net charge in all types of semiconductors remains neutral after doping.

A simple visualization of the replacement of silicon atoms by pentavalent atoms (like phosphorus) and trivalent atoms (like boron), is respectively shown in figures 2.6 and 2.7. The effect of this replacement in terms of band gap, i.e. extra states near the conduction band in n-type and extra states near the valence band in p-type, is shown in figure 2.8.

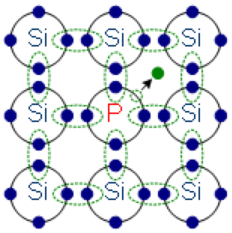

Figure 2.6: Schematic view of how phosphorus donates an extra electron to silicon. The blue filled circles represent shared atoms, and the green filled circle represents the extra electron donated by phosphorus.

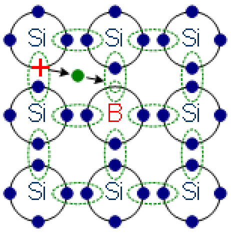

Figure 2.7: Schematic view of how boron accepts an electron from silicon. The blue filled circles represent shared atoms, and the green filled circle represents the electron accepted by boron.

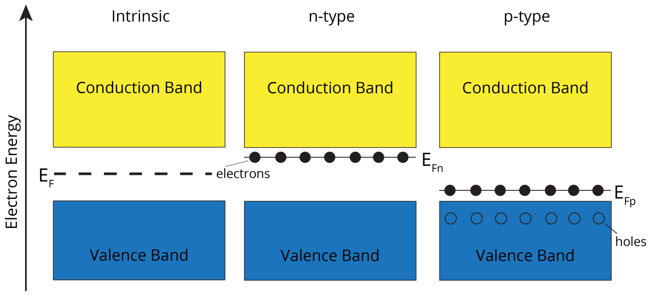

Figure 2.8: Schematic illustration of the effect of doping on the Fermi level in semiconductors.

Diffusion Mechanism of Phosphorus

In this research phosphorus doped silicon or SiO_x layers are investigated. To gain more understanding of the phosphorus doping process, the phosphorus doping (and diffusion) mechanism in both silicon and silicon oxide will be discussed. A general method to add n-type dopants to the silicon is to expose silicon wafers in a quartz furnace to phosphoryl chloride ($POCl_3$) and O_2 (with N_2 is typically added as carrier gas). Once the silicon wafers are loaded in the tube, the furnace is heated to the desired process temperature. Then, the carrier gas is passed through a bubbler containing the liquid $POCl_3$. The liquid $POCl_3$ is subsequently brought into the process chamber where it evaporates and reacts with externally supplied O_2. This reaction results in the formation of a thin liquid P_2O_5 layer according to reaction equation 2.1a. The Cl_2 is continuously ventilated from the system during the deposition step. The next step is the formation of phosphosilicate glass (P_2O_5, PSG) through reaction equation 2.1b.

$$4\,\mathrm{POCl_3}\,(g) + 3\,\mathrm{O_2}\,(g) \longrightarrow 2\,\mathrm{P_2O_5}\,(l) + 6\,\mathrm{Cl_2}\,(g) \tag{2.1a}$$

$$2\,\mathrm{P_2O_5}\,(l) + 5\,\mathrm{Si}\,(s) \longrightarrow 5\,\mathrm{SiO_2}\,(s) + 4\,\mathrm{P}\,(s), \tag{2.1b}$$

The PSG layer is the source of phosphorus during the next step, which will be referred to as the drive-in step. The drive-in step can be seen as the doping step, and consists of the phosphorus diffusion from the PSG layer into the silicon wafer. It should be made clear that reaction 2.1a already starts to occur during pre-deposition, since the temperature during this process is near the diffusion temperature of phosphorus (T=790 °C or higher).

In order to find an effective doping process of the poly-SiO_x layers developed in this study, it is important to understand the phosphorus diffusion processes that are used for doping of silicon (oxide). First the procedure of the phosphorous diffusion in silicon will be described. After that, the effect of the oxide content on the phosphorus diffusion in silicon oxide will be discussed.

Phosphorus can either diffuse to interstitial sites or to substitutional sites, depending on the process conditions (temperature, $POCl_3/O_2$ flow) and on the concentration. The solubility limit of dopants depends on the temperature and is plotted against the temperature for several dopants in figure 2.9. Note that the solubility limit includes both the electrically active and inactive dopants.

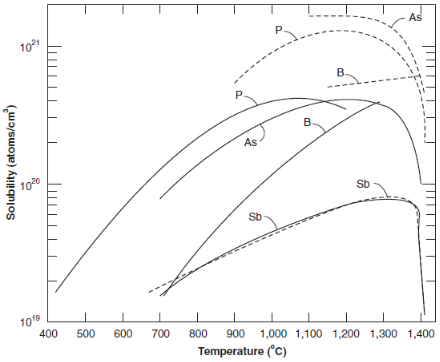

Figure 2.9: Overview of the solubility limit in silicon for most important dopant atoms. Solid line represents study of Borisenko and Yudin [29] and dotted line represents the study of Trumbore [30].

The solubility limit of phosphorus in silicon for 800 °C to 900 °C, i.e. the temperature range of the $POCl_3$ treatments used in this study, is found to be about $3 \times 10^{20}\,\mathrm{cm}^{-3}$ [31]. Phosphorus atoms that are present in the silicon layer at interstitial sites are not active dopants, since the atoms are not built into the lattice. The number of phosphorus atoms at interstitial sites should be kept as low as possible, since at these sites the dopants are not electrically active but may contribute to Shockley-Read-Hall recombination [32]. On the contrary, the phosphorus atoms that replace silicon atoms at substitutional sites are known to be electrically active, which is the desired state.

If the surface concentration of phosphorus is sufficiently high, for example in a silicon solar cell's diffused region, the phosphorus profile of electrically active phosphorus has a flat plateau near the surface. If highly doped poly-Si is used as a selective layer, the poly-Si thickness can be estimated from the depth of this plateau region, since the poly-Si layer itself will be saturated and further in-diffusion is blocked in large part by the thin oxide below the poly-Si layer. Further phosphorus in-diffusion in silicon,

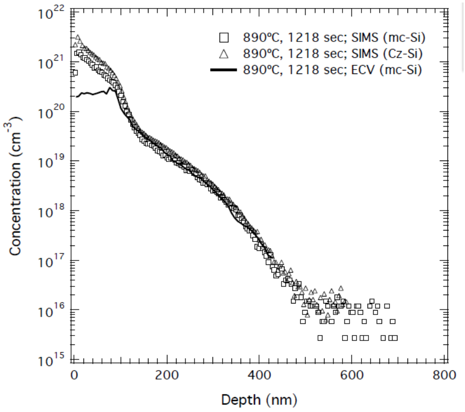

Figure 2.10: Classical phosphorus concentration profile in Si, measured by Electrochemical Capacitance Voltage (ECV, explained in 3.2.1) and Secondary Ion Mass Spectroscopy. Please note the inactive phosphorus concentration at the surface measured by SIMS.

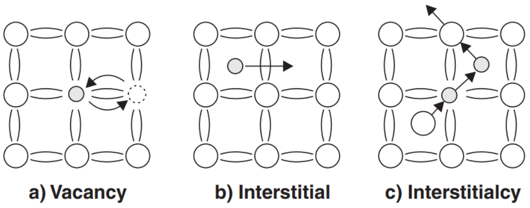

Figure 2.11: Schematic representation of how phosphorus diffuses in silicon. From left to right: vacancy mechanism, interstitial mechanism, interstitialcy mechanism (also known as dual mechanism).

occurring during process steps that involve high temperatures (such as thermal oxidation), will result in a characteristic kink- and tail doping profile. In-diffusion causes a reduction of chemical passivation at the interface and increases free carrier absorption [33].

The classical phosphorus-diffusion profile, consisting of plateau-kink-tail shape, is shown in figure 2.10. Three regions can be distinguished in this characteristic phosphorus doping profile:

1. High concentration region (typically above $3 \times 10^{20}\,\mathrm{cm^{-3}}$). When phosphorus levels are exceeding a characteristic value, the diffusion is dominated by the vacancy mechanism via double negative vacancies. The diffusion reaction may be related to the vacancy concentration and is described as

$$\mathrm{P_{Si}}^{+} + \mathrm{V}'' \rightleftharpoons (\mathrm{P_{Si}} - \mathrm{V})' \tag{2.2}$$

   where P_{Si}^{+} is an an ionized substitutional P atom, V'' is a double negative vacancy and $(P_{Si} - V)'$ is the nearest neighbour pair configuration.

2. Intermediate concentration region. When the phosphorus concentration is in the range of $1 \times 10^{19}\,\mathrm{cm^{-3}}$ to $3 \times 10^{20}\,\mathrm{cm^{-3}}$. In the transition region the diffusion mechanism is undergoing a changeover from an interstitial-driven diffusion (low concentrations) to vacancy-based diffusion (high concentrations).

3. Low concentration region (typically below $1 \times 10^{20}\,\mathrm{cm^{-3}}$). The phosphorus diffuses in the silicon via an interstitial mechanism. Via a so called ”kick-out” mechanism silicon atoms are kicked-out from lattice sites to interstitial sites. Phosphorus then becomes electrically active.

$$\mathrm{Si_{Si}} + \mathrm{P_i} \rightleftharpoons (\mathrm{P_{Si}}^{+} + \mathrm{Si_i} + \mathrm{e}^{-}), \tag{2.3}$$

   where e^{-} is an electron, P_{Si}^{+} is an ionized substitutional P atom, $\mathrm{P_i}$ is an interstitial and $\mathrm{Si_{Si}}$ is a substitutional Si atom and $\mathrm{Si_i}$ is a self-interstitial.

2.5. Oxidation Mechanisms

n this study two different types of oxidation, known as dry oxidation and wet oxidation, have been analysed. Basic understanding of these mechanisms is required to be able to discuss the quality of the developed SiO_x layers.

The chemical reactions taking place during dry- and wet oxidation, are shown in equations 2.4a and 2.4b.

$$\mathrm{Si} + \mathrm{O_2} \longrightarrow \mathrm{SiO_2}, \tag{2.4a}$$
$$\mathrm{Si} + 2\,\mathrm{H_2O} \longrightarrow \mathrm{SiO_2} + 2\,\mathrm{H_2}, \tag{2.4b}$$

Oxidation takes place upon inward diffusion of the oxidant (oxygen or water vapour) whereby silicon is consumed. For every unit thickness of SiO_2 growth, about 0.45 unit thickness of Si is consumed and the volume expanses about 2.2 times, causing compressive stresses in SiO_2. During oxidation a $SiO_2|Si$ interface is created, which moves towards the silicon substrate. The growth rate of dry oxidation and wet oxidation is differs a lot. The growth rate of dry oxidation is known to be slow, whereas the growth rate of wet oxidation is quite large. Of course, the oxidation rate may be influenced by temperature. In figures 2.12 and 2.13, the oxide thickness is plotted as function of oxidation time for different temperatures. The dry oxidation process is not exceeding growth rates of about 100 nm h^{-1}, where wet oxidation can operate up to approximately 600 nm. The diffusivity of the oxidant is the rate limiting step during oxidation. Since the diffusivity, in the growing oxide, of the wet oxidant (hydroxide) is much larger than of the dry oxidant, wet oxides grow much quicker than dry oxides. It is well-known that the oxidation rate increases significantly in heavy doped silicon layers increases the rate of oxidation. This effect is greater in boron doped silicon than in phosphorus doped silicon [34]. Dry oxidation of silicon results in dense SiO_2 layers, whereas the SiO_2 layers obtained by wet oxidation of silicon result in porous layers.

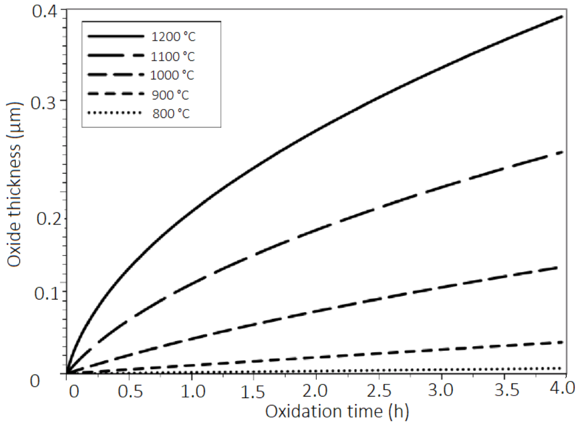

Figure 2.12: Growth kinetics of dry oxidation process. Oxide thickness is plotted versus oxidation time. Image modified from [35], based on [36].

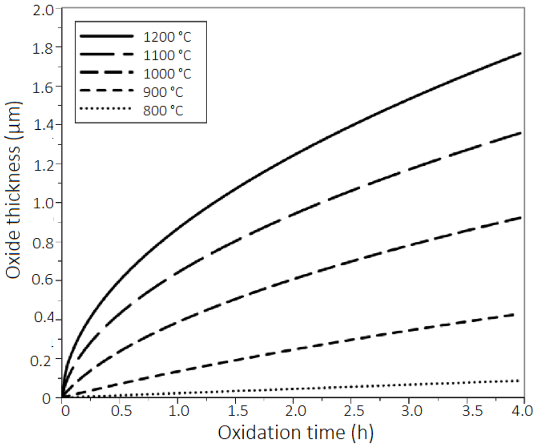

Figure 2.13: Growth kinetics of wet oxidation process. Oxide thickness is plotted versus oxidation time. Image modified from [35], based on [36].

2.6. Low Pressure Chemical Vapor Deposition (LPCVD)

The technique which is used in this study to deposit the layers on the Czochralski (CZ) and Float-Zone (FZ) n-type silicon wafers is called Low-Pressure Chemical Vapor Deposition (LPCVD). As its name implies, "low pressure" chemical vapor deposition distinguishes itself from other chemical vapor deposition techniques by the low pressure environment in the furnace, typically around 10×10^{-3} mbar to 3×10^{-1} mbar. Nowadays, most $\mathrm{SiO_x}$ layers are deposited by means of Plasma-Enhanced Chemical Vapor Deposition (PECVD). PECVD is operating at extremely low pressures, around the vacuum level (1×10^{-8} mbar). The main reason to use LPCVD over PECVD is that the former is known as low-cost industrial process and thus can be applied on large scale. Furthermore, when the pressure is increased the mass transport velocity will decrease proportionally to the pressure. In general, low deposition rates result in highly uniform layers with low concentration of defects [37]. Since LPCVD processing takes place at relatively low deposition rates, i.e. high pressures, when compared to PECVD, more uniform layers can be formed with LPCVD. However, relatively high deposition temperatures ($> 500\,^{\circ}\mathrm{C}$) and relatively long deposition times are required to obtain similar layer thickness as obtained with PECVD. The horizontal furnaces generally consist of three large modules: the load station where the loading of the wafers occurs; the furnace section, which is comprised of one to four reactor chambers; and the gas distribution cabinet where the flow of gases into the reactor chambers is controlled, and often customized to meet the requirements of a customer's particular processes. In this study the inlets needed to be modified in such a way that it was possible to let both nitrous gas and silane gas flow into the tube at the same time.

3

Methodology

In this study two different routes for manufacturing of doped SiO_x layers have been investigated: a post oxidation route, including both wet and dry oxidation, and a post doping route. The quality of the SiO_x layers made with the different routes was determined by analysis of both electrical and material (structure/homogeneity/morphology/grain size/phases) properties. The post-oxidation route is based upon an ex-situ oxidation process, whereas the post-doping route is based upon an in-situ oxidation process. In this study CZ <100> n-type silicon wafers and FZ <110> n-type silicon wafers have been used as substrate material. The choice of (chemically polished) CZ or (mechanically polished) FZ wafers was dependent on the characterization method that was used after deposition of the SiO_x layer. For example, for spectroscopic ellipsometry mechanically polished FZ wafers were preferred.

3.1. Production Methods

3.1.1. Post-Oxidation of LPCVD Doped Poly-Si Using Dry and Wet Oxygen

In the first experiment, the first fabrication route for manufacturing of doped SiO_x layers was examined. Here, silicon oxide layers were formed by oxidation of phosphorus doped poly-Si layers. To achieve this, symmetrical samples were made using a seven step process. An overview of the process steps is given in figure 3.1. In the first step the CZ n-type Si wafers were cleaned using 1% hydrofluoric acid (HF) and polished in an alkaline chemical bath. Surface cleaning is required to remove the native oxide and contaminants (organic and metallic) from the wafer surface. In the second step, an ultra-thin tunnel oxide (SiO_x) has been created on both sides of a CZ n-type Si wafer by thermal oxidation and intrinsic poly-Si layers were deposited on top by deposition in a LPCVD furnace at 650 °C using silane (SiH_4) as source gas. The third step consisted of phosphorus (dopant) diffusion into the poly-Si layer during a high temperature 850 °C $POCl_3$ treatment. During this $POCl_3$ treatment, first a PSG layer is grown, which will be removed in the fourth step by a 9% HF dip, followed by a drive-in step at 850 °C during which the phosphorus diffuses from the PSG layer into the poly-Si layers to create the n-type doping. It should be noted that during the doping process ($POCl_3$) about 15 nm on top of the poly-Si is oxidised because of the PSG growth. In the fifth step, the SiO_x layer was formed at the expense of the poly-Si layer during a dry or wet post-oxidation LPCVD process. After post-oxidation some samples were already characterized to study the properties of the SiO_x layers. Most of the samples were further processed in steps six and seven, the hydrogenation and firing steps. During the hydrogenation step SiO_x layers are encapsulated by an SiN:H layer that was deposited on top by a remote PECVD at 375 °C. Hereby, hydrogen diffuses to dangling bonds in the SiO_x layer and to the interface between the silicon and SiO_x. Finally, a rapid high temperature anneal at 830 °C was performed in a belt furnace, more commonly known as the firing process. This process is used in the manufacturing of the metal contacts in solar cells and the properties of the layers should be stable or improving during this step.

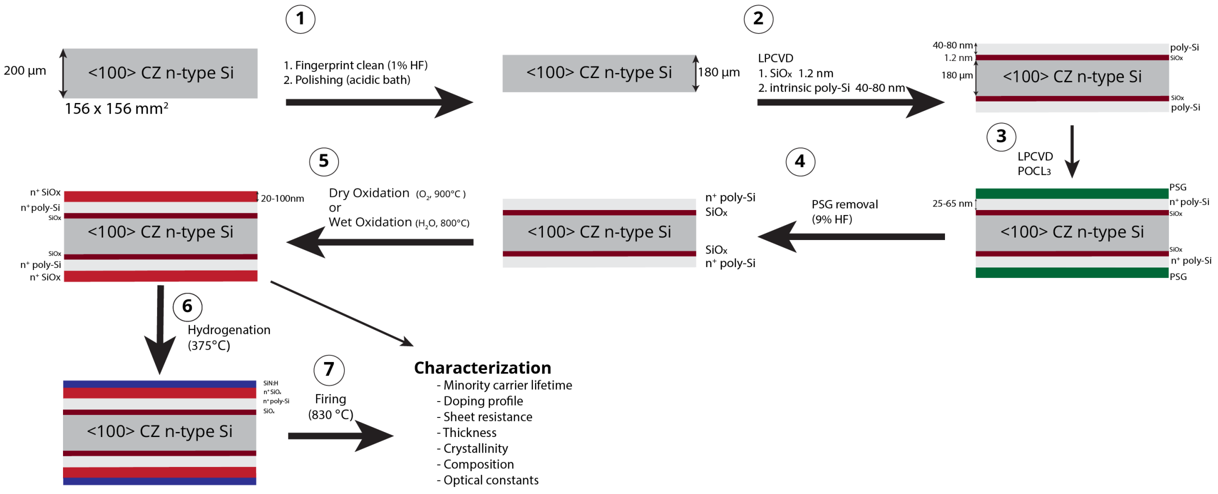

Figure 3.1: Process flow which show the steps to produce the symmetrical samples with SiO_x layer by dry or wet oxidation.

Please note that the thickness of the remaining poly-Si layer depends on the oxidation time and can be much less than the thickness shown after step five in the process overview. With respect to transparency the most favourable situation is that the poly-Si is completely oxidised, which results in a symmetrical sample with only phosphorus doped SiO_x on both sides of the wafer. However, it might be more promising in terms of conducting properties to still have some remaining doped poly-Si for lateral transport of charge carriers. This results in a stacking sequence of poly-Si and SiO_x on top of the CZ wafer.

The dry- and wet oxidation processes have been investigated respectively at 800 °C and 900 °C. The different temperatures have been chosen as such that desirable thickness could be obtained in a reasonable time range (with an eye on future industrial applications). For both oxidation processes three different oxidation times have been examined which differed per initial poly-Si thickness. An overview of the applied oxidation times for each initial poly-Si thickness is shown in table 3.1.

Table 3.1: Overview of oxidation times per oxidation method.

Initial poly-Si thickness (nm)	**Dry oxidation times** (min)	**Wet oxidation time** (min)
25	6, 16, 108	6, 12, 45
45	16, 108, 300	12, 30, 45
65	16	12, 30, 45

3.1.2. Post-Doping of LPCVD Poly-SiO$_x$ Layers

In the second experiment, the second manufacturing route was examined, i.e. in-situ growth of LPCVD SiO$_x$. This experiment is based on a study of da Silva Zambom et al., who deposited SiO$_x$ layers by means of LPCVD under different process conditions [38]. The tested in-situ oxidation and post-doping process consists of five steps. An overview of the process steps is given in figure 3.2. The pre-cleaning and polishing steps of the CZ n-type silicon wafers are exactly the same as for the previously described post-oxidation sequence. After the cleaning and polishing of the silicon wafers, the wafers were placed in the LPCVD furnace and exposed to different ratios of nitrous and silane gas. The N_2O/SiH_4 gas flow ratio determines the oxide fraction in the SiO$_x$ layer. So, by adjusting the N_2O/SiH_4 flow ratio, the oxide fraction can be varied. In this experiment, the silane gas flow was kept constant and the nitrous gas flow was varied. Before the main experiment was executed, one test sample was developed to check the effect of process parameters. The SiO$_x$ layer in the test sample was formed by 30 min exposure of a CZ n-type wafer to a gas flow ratio of 0.33. After the test measurements, the In total four different flow ratios were investigated; 0.33, 0.42, 0.50 and 0.58. Also, two different deposition times have been examined, i.e. 90 min and 120 min. After deposition, the as-deposited SiO$_x$ layers were doped with phosphorus during a $POCl_3$ treatment at 870 °C. This drive-in process is executed at 20 °C higher temperature than the $POCl_3$ process of wet and dry oxidised samples, since it is expected that the oxides are blocking the phosphorus diffusion making the doping of SiO$_x$ more difficult than of poly-Si.

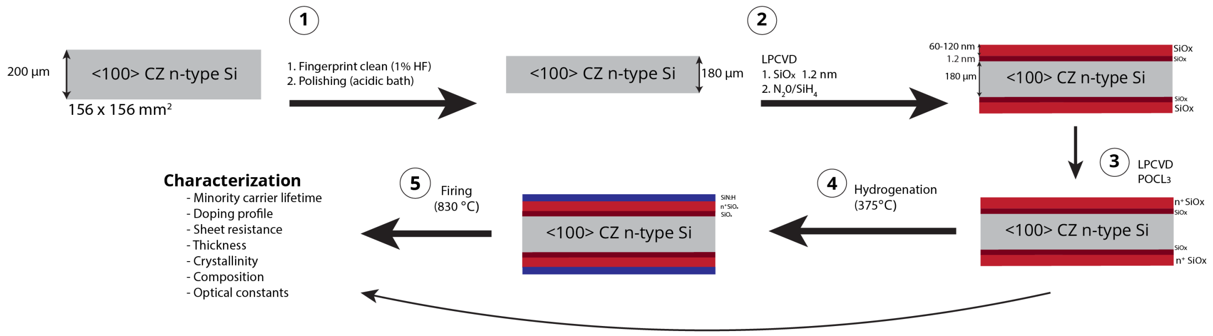

Figure 3.2: Process flow which show the steps to produce the symmetrical samples with SiO$_x$ by varying N_2O/SiH_4 gas flow ratio.

3.2. Characterization Techniques

The characterization techniques that have been used to analyse the SiO$_x$ layers are described in this section. In table 3.2 an overview is given of the techniques that have been used to obtain results of certain material properties.

Table 3.2: Experimental matrix which shows the techniques used to obtain information about the properties of the SiO$_x$ layers.

Property	**ECV**	**QSSPC**	**FPP**	**PL**	**SE**	**SEM**	**FTIR**	**XRD**
Passivation	✓							
Doping profile		✓						
Sheet resistance		✓	✓					
Thickness	✓				✓	✓		
Crystallinity						✓		✓
Composition				✓		✓	✓	
Optical constants					✓			

3.2.1. Electrochemical Capacitance-Voltage (ECV)

Electrochemical capacitance voltage measurements were done to obtain a doping concentration profile along a certain depth, with a depth resolution in the nm range. A schematic impression of the ECV set-up is shown in figure 3.3.

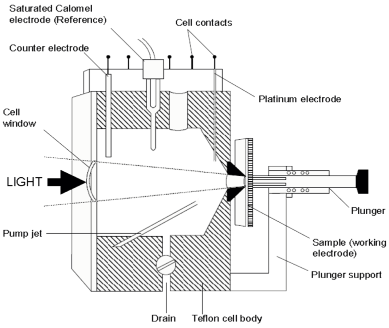

Figure 3.3: Schematic of electrochemical capacitance voltage measurement set-up.

The semiconductor is placed in contact with a specific electrolyte on a small area (A) in the order of 1 mm^2. The electrolyte has a dual role in both the formation of a Schottky barrier and as an etchant. The Schottky barrier provides the basis of the measurement of the doping profile and the ething process is requried to obtain a depth profile [39]. At the junction a depletion region develops, which is a region depleted from electrons and holes, but may contain the dopant atoms and/or electrically active defects. This region behaves like a capacitor and the capacitance of this system can be measured which can then be related to the doping profile (which will be shown later). By varying the applied voltage to this junction the depletion width will vary accordingly. In order to vary the width of depletion region either a reverse or forward bias needs to be applied depending on the type of semiconductor, n- or p-type, respectively. The capacitance is defined as the ratio of the change in electric charge in a system (the depletion region) to the corresponding change in electric potential (space charge). The capacitance measurement has either a positive or a negative value depending on whether the system is reversed or forward biased, respectively. The doping concentration, N_A, is a function of this capacitance and is calculated according to equation 3.1.The complete derivation of this equation can be find in the study of U. Hashim et. al. [40].

$$N_A(W_d) = \frac{C^3}{q\epsilon_0\epsilon_r A^2 \frac{dC}{dV}}, \tag{3.1}$$

where N_A is the doping concentration, W_d is the depletion region width, C is the capacitance, q is the electronic charge, ϵ is the relative permittivity, ϵ_0 is the vacuum permittivity, A is the measured wafer area and dV is the bias (potential increment).

It should be noted that ECV is only able to measure substitutional (active) dopants and thus interstitial (inactive) dopants will not be accounted for. The doping concentration is measured at certain depths. These depths are reached by electrolytically etching the semiconductor sample. The dissolution of the semiconductor is reliant on the presence of holes. As in p-type material holes are the majority carriers, the holes are readily present. However in n-type material these holes need to be created. This is done by an extra illumination step. The thickness of the material dissolved is calculated by integrating the dissolution current and subsequently applying Faraday's law. The total depth shown in the ECV graphs, is a combination of the removed thickness and depletion depth. The etched depth, W_r, is calculated according to equation 3.2 [41].

$$W_r = \frac{M}{ZF\rho A}\int_0^t Idt, \tag{3.2}$$

where M is the molecular weight, Z is the dissolution number (number of charge carriers transferred per molecule), F is Faraday's constant, ρ is the density of the material, I is the dissolution current and t is time.

The dissolution and capacitance measurements are continuously repeated by etch/measure cycles to profile the carrier concentration as a function of depth. The depth profile is obtained by electrolytically etching of the semiconductor between the capacitance measurements. In this study the electrolyte being used is ammonium fluoride (NH_4F) and the metallic liquid as contact being used is gallium indium (GaIn). As this electrolyte is optimized for silicon dissolution and not for silicon oxide dissolution, it was not possible to etch the silicon oxide properly. Therefore, the silicon oxide layer was removed in order to conduct ECV measurements. Although it was not possible to determine the phosphorus concentration in the silicon oxide layers, it was still useful to perform ECV measurements as it revealed information about the in-diffusion in the silicon wafer.

3.2.2. Quasi-Steady-State Photoconductance (QSSPC)

In this research the passivation quality of the developed layers were checked by measurements with the Sinton WCT-120. The set-up of this equipment is shown in 3.4 below.

Figure 3.4: Quasi-steady state photoconductance measurement tool from Sinton instruments (Sinton WTC-120).

The quasi-steady-state photoconductance measurement tool provides information about the minority carrier lifetime at a specific spot in the sample (diameter of about 2 cm) [42].

In the squared sample holder a radio frequency coil is created which sends electromagnetic waves to the sample (silicon wafer). When the flash lamp pulses light into the sample, excess charge carriers will be generated, which causes a change in photo-conductance (current) of the wafer. The time-varying conductance is detected by inductive coupling. The inductive coupling occurs in the coil because the excess charge carriers interact with the coil by changing the resistance of the coil and thus induces a voltage across the coil. The charge carriers recombine resulting in a decay of the eddy current. The decay of eddy current can be monitored (phase and amplitude of AC current) and compared with the time dependent intensity of the flash light. Since the minority carrier lifetime is related to this change, an indication of the minority carrier lifetime can be given. Two distinct measurement modes should be distinguished. The Quasi-Steady-State (QSS) relation and the transient relation. In QSS the generation rate is equal to the recombination rate, whereas in transient generation rate is much larger than the recombination rate. The QSS measurement mode is applied for samples where the minority carrier lifetime is less than 100 µs, and the transient measurement mode is applied for samples where the minority carrier lifetime is larger than 100 µs. The minority carrier lifetime in QSS is calculated according to equation 3.3.

$$\tau_{\mathrm{eff}} = \frac{\delta p}{G}, \tag{3.3}$$

where δp is the excess minority carrier density and G is the photogeneration of the minority charge carriers. The effective minority carrier lifetime in samples which obey the transient requirements can be described by equation 3.4.

$$\tau_{\mathrm{eff}} = -\frac{\delta p}{\frac{d\delta p}{dt}} \tag{3.4}$$

The minority carrier lifetime values at an excess minority carrier density of 1×10^{15} cm^{-3} are taken as a measure for the interface passivation quality, which is a chosen representative injection level at which Shockley-Read-Hall recombination is dominant, but trapping effects can be ignored. An example of the datasheet obtained during this measurement is added to the appendix. Please note that, although the reflection of the light pulse (more specifically, the refractive index of the top layer) has little effect on the minority carrier lifetime, is taken into account when measuring in QSS. Also, all mentioned minority carrier lifetimes are averages of four measurements. On top of that, the measurements of the minority carrier lifetimes in the post-doped samples were measured at five spots on the silicon wafer (middle, left top corner, left bottom corner, right top corner and right bottom corner).

3.2.3. Sherescan (FPP)

The sheet resistance measurement is based on a four-point-probe instrument. The four-point-probe is able to measure the average resistance of a thin layer or a sheet. A simple schematic of the set up is shown in figure 3.5. A DC current is applied to the outer two probes (1 and 4) and a voltage drop is measured between the two inner probes (2 and 3). The voltage drop is large for insulating layers and is low for conducting layers. The sheet resistance (R_S, Ω/sq) is defined as

$$R_S = \frac{\pi}{ln(2)} \frac{\delta V}{I}, \tag{3.5}$$

where $\frac{\pi}{ln(2)}$ is a geometrical factor, δV is the voltage difference between inner probes (2 and 3) and I is the current applied between the outer probes (1 and 4).

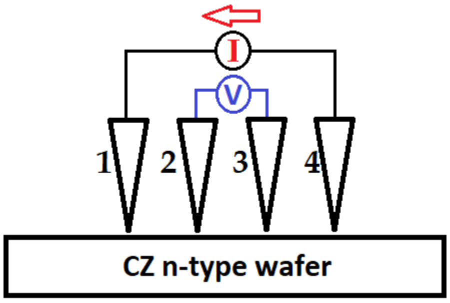

Figure 3.5: Simple schematic visualization of the principle of the sherescan apparatus.

It is expected that the sheet resistance decreases when the silicon oxide layer is properly doped, whereas it is expected that the sheet resistance increases when the silicon oxide layer is not properly doped. During the oxidation step the phosphorus may diffuse from substitutional silicon lattice sites to interstitial sites or it diffuses into the bulk silicon. In both cases the active phosphorus concentration in the silicon oxide layer, and thus sheet resistance value, decreases. On the contrary, if the inactive phosphorus atoms present in the poly-Si layer diffuse to substitutional sites or active phosphorus atoms remain in the silicon oxide layer while oxide atoms are incorporated in the poly-Si layer, the silicon oxide layer will contribute to lateral conductivity. In that case the sheet resistance will decrease when the silicon oxide layer is removed.

3.2.4. Scanning Electron Microscope (SEM)

A Scanning Electron Microscope was used to analyse the SiO_x layers in terms of homogeneity, thickness, different phases and elemental distribution. High resolution images of surface topography can be quickly obtained by top view analysis, which indicates the grain size and crystal structure (amorphous or crystalline). In this way the SEM measurements revealed information about the morphology and structure of the SiO_x layer. Also, SEM was used to estimate the thickness of the layers. The layers in the symmetrical samples can be distinguished because of their difference in conductivity. The larger the conductivity of the sample, the less the layer charges and thus it will appear darker in the SEM image. Within this study, the SEM samples were prepared by simply breaking of the silicon wafer along the crystallographic direction.

Energy Dispersive X-ray (EDX)

The elemental composition in a sample may be determined by a specific analysis method that is built into the SEM, called Energy Dispersive X-ray spectroscopy (EDX). Electrons are accelerated towards the sample surface and if sufficient energy is gained by the electrons upon acceleration they can excite electrons from the inner shell to the outer shell. Subsequently, an excited electron from the outer shell will fall back to the energy of the inner shell whereby energy is emitted in the form of element characteristic X-rays. The intensity of the X-rays is related to the number of emitted x-rays transitions, and therewith the number of atoms of a certain element, and is represented on the y-axis of the EDX spectrum. The intensity peak appears at the element specific energy level, shown on the x-axis, based on which the different elements are recognized. A typical SiO_x EDX spectrum is shown in figure 3.6.

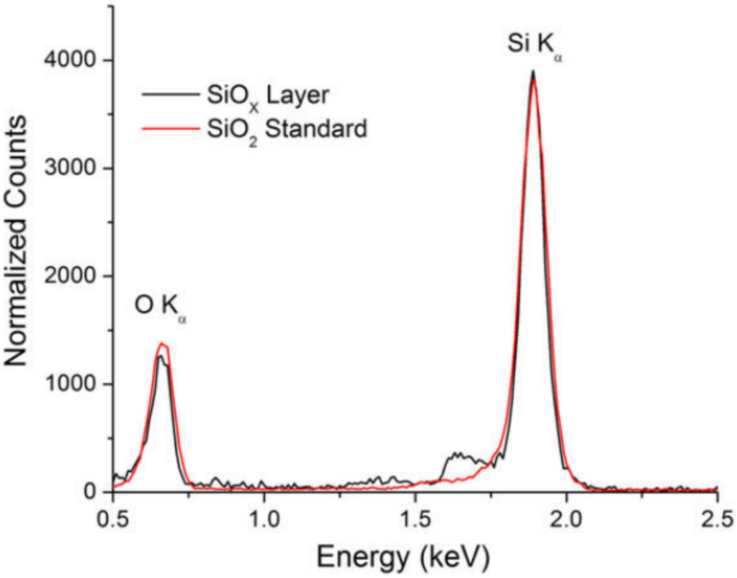

Figure 3.6: Typical EDX spectrum of SiO_x. Spectrum obtained from [43].

As SiO_x is an insulating material, charge build-up will take place if the sample is not prepared properly. To prevent charge build-up, the insulating SiO_x surface is coated with a thin layer of a conductive material.

3.2.5. Fourier Transform Infrared Spectroscopy (FTIR)

Fourier Transform Infrared Spectroscopy, shortly FTIR, is technique used to reveal information about the absorption of a material at a specific wavelength. The FTIR apparatus used in this study was one of the type Nicolet 5700, equipped with a transmission accessory.

During a FTIR measurement, multiple frequency infrared light is shined at the sample. The molecules in the sample interact with the light whereby characteristic molecular vibrations take place at a specific wavelength, which are associated with a change in dipole moment. FTIR measurements will reveal information about the type of bonds present and may be related to specific properties. For example, the absence of the characteristic Si-H peak before hydrogenation and the presence of this peak after hydrogenation may be associated with a successful hydrogenation process. In figure 3.7 normalized FTIR spectra are shown of SiO_x layers with oxide content (x) varying between 0.1 and 2 (stoichiometric silicon dioxide). It should be clear that the peak position and the shape of the peak absorption are affected by the mixing of the Si and O atoms. The more oxygen is incorporated in the SiO_x layer (i.e. the higher the value for x), the more pronounced the shoulder on $1150\,\mathrm{cm}^{-1}$ becomes.

In advance of collection of the sample spectrum a background measurement is done. The background measurement contains contributions of the environment which do not represent the information about the sample. For the FTIR measurements of the post-oxidised samples, a CZ n-type wafer with symmetrically deposited tunnel oxide and 45 nm poly-Si was chosen as a reference sample. For the FTIR measurements of the post-doped samples, a bare FZ n-type wafer was chosen as reference sample.

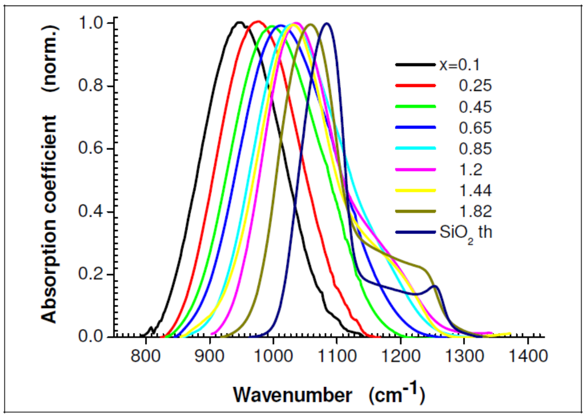

Figure 3.7: Normalized FTIR spectra of SiO_x layers, showing that position and shape of absorption peak are dependent on oxygen content. Image taken from [44].

3.2.6. X-ray Diffraction (XRD)

X-ray Diffraction, or shortly XRD, is a non-destructive technique based on interaction between monochromatic X-rays and atoms within the sample material. X-ray diffraction can be used to reveal information about the crystal structure, chemical composition and physical properties of a sample. In this study XRD will be used to determine the crystallinity of the sample. The scattered X-rays can either undergo constructive or destructive interference, or a combination of both. This scattering process is known as diffraction and is described by Bragg's law, according to equation 3.6, shown below.

$$n = 2d \times sin\,(\theta) \tag{3.6}$$

In this formula n is an integer, *d* is the interplanar spacing between rows of similar atoms and θ is the angle of the X-ray beam with respect to the atomic planes. Only the atoms which are fulfilling Bragg's law are in phase and will cause diffraction. If the atoms are arranged in a crystalline way, the material has long range order and thus X-rays will be scattered in few directions leading to narrow peaks. If, however, the atoms are arranged in an amorphous way, the material does not possess long range order and thus X-rays will be scattered in many directions leading to wide range distribution. Also, when more symmetry is present in the material, less peaks will be expected. So, when crystalline silicon is present few sharp peaks are expected, whereas more (and broader) peaks are expected for amorphous silicon (and silicon oxides). In this experiment both conventional and parallel beam XRD has been applied. With the parallel geometry the sample position can be varied and thus varying the distance between X-ray source and sample, as well as the distance between the sample and the detector. Hereby the contribution of the thin film will be enlarged, but the detection limit is decreased.

Also, from XRD measurements it was possible to determine average grain size (d) by applying the Scherrer equation, shown below in equation 3.7 [45].

$$d = \frac{k\lambda}{\beta cos\,(\theta)} \tag{3.7}$$

In this equation, k is a constant=0.94, λ the characteristic wavelength of the X-rays impinging on the sample (λ =0.154 nm), β is the full width at half-maximum of the diffraction peak and θ is the Bragg angle.

3.2.7. X-ray Photoelectron Spectroscopy (XPS)

X-ray Photoelectron Spectroscopy (XPS) is a quantitative analysis technique which is used for surface analysis (up to a depth of 5 nm. A typical XPS setup is shown in figure 3.8. The technique is based on the excitement and emittance of photoelectrons after bombarding the sample surface with Al-K$_\alpha$) or Mg-K$_\alpha$) X-rays, in an ultra high vacuum environment ($<5 \times 10^{-9}$ mbar). The energy of the emitted photoelectrons is characteristic for a specific element. Subsequently the surface composition can be calculated from the peak areas of the identified elements. In this research unmonochromatized Mg-K$_\alpha$ X-rays were used as a source which was operating at an acceleration voltage of 13 kV and a power of 200 W.

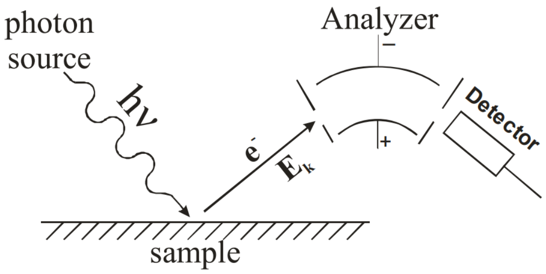

Figure 3.8: Schematic view of XPS setup. Image taken from [46], based on [47].

3.2.8. Spectroscopic Ellipsomsetry (SE)

Spectroscopic ellipsometry is a measurement technique which uses polarized light to determine optical properties and thickness of thin layers (several nm). The detector is able to measure a change in polarization as light reflects from, or transmits through a material structure. The polarization change is associated with a specific amplitude ratio (Psi, ψ) and phase difference (Delta, δ). These parameters can be related to optical properties and thickness of the measured sample. Besides the determination of optical properties and thickness, ellipsometry can also be applied to characterize other material properties associated with a change in spectral response, such as crystallinity, roughness and doping concentration. An important criterion for the created model is that it may not result into any unphysical shapes of the optical constants. The index n (index of refraction) must increase toward shorter wavelengths when a transparent material (extinction coefficient k=0) is analysed, whereas it must decrease toward shorter wavelengths when a more opaque (stronger absorbing, k increases) material is analysed. The optical constants of silicon are shown in figure 3.9, which meet these requirements.

In this study ellipsometry was used to get insight in the optical constants of the SiO$_x$ layer. First a Cauchy model was applied to determine the thickness. The mathematical description of this model can be found in the appendix. The model was validated by comparing the thickness value of the model with the thickness estimated from the SEM cross-sections. Subsequently the thickness was set as constant, and a model was made to determine the optical constants of the layer.

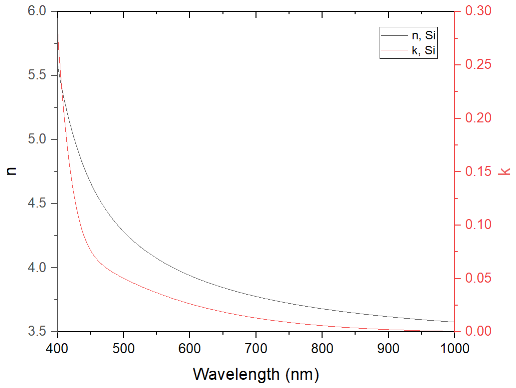

Figure 3.9: Refractive index and extinction coefficient for silicon.

3.2.9. Weighing Method to Calculate Oxygen Fraction

The oxygen fraction in the in-situ oxidised SiO_x layers was determined by a weighing test. For each in-situ SiO_x growth recipe, four test samples were used to increase the reliability of the weighing measurement. A SiN_x layer was deposited on a test wafer by PECVD, to protect the silicon wafer against oxidation during subsequent oxidation steps. After SiN_x deposition, the test wafer was placed in the same LPCVD tube and exposed to one of the in-situ SiO_x growth recipes of the post-doping tests. Finally, the SiO_x layer was completely oxidised to stoichiometric SiO_2 at 1000 °C for 1 hour by wet oxidation. The weight of the test sample was measured on a microbalance after each consecutive deposition step (after SiN, SiO_x and SiO_2). The difference in weight between the stoichiometric (SiO_2) and substoichiometric (SiO_x) oxide layers is completely due to oxygen incorporation. This gain in oxygen incorporation is used to determine the oxide fraction in the SiO_x layer. The contribution of silicon to the weight of the layer is known ($28\,\mathrm{g\,mol^{-1}}$), and the oxide fraction is known to be $16\,\mathrm{g\,mol^{-1}}$ for every oxygen atom incorporated. The oxide fraction (x) in the silicon oxide layer can be calculated by:

$$x = \frac{60}{16} \times \frac{m_{Sio_{\mathrm{x}}} - m_{wafer}}{m_{\mathrm{SiO_2}} - m_{wafer}} - \frac{28}{16}, \qquad (3.8)$$

where $m_{Sio_{\mathrm{x}}}$ is the weight of the wafer after deposition of the SiO_x layer, m_{wafer} is the wafer after SiN_x deposition and $m_{\mathrm{SiO_2}}$ is the weight after complete oxidation of the SiO_x layer. The complete derivation of this equation is shown in the appendix.

In figure 3.10 a schematic overview is given to show how the layers are deposited on the wafer.

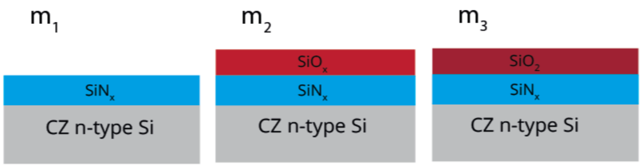

Figure 3.10: Samples used for each consecutive weight measurement. m_1 is the weight of the SiNx capped wafer, m_2 is the weight of the SiO_x layer on SiN_x capped wafer, and m_3 is the weight of the completely oxidised SiO_2 layer on SiN_x capped wafer.

4

Post-Oxidation of LPCVD Doped Poly-Si Using Dry and Wet Oxygen

In this chapter the reader will be provided with the results of the post-oxidation of poly-Si using dry and wet oxygen. The results will be described in terms of material properties whereby information of different analysis techniques is combined. As it became clear quite soon that dry oxidised samples were less promising than wet oxidised samples in terms of lifetime, more experiments have been performed on the wet oxidised samples.

4.1. Results

4.1.1. Minority Carrier Lifetime in Post-Oxidised Doped Poly-Si

In figure 4.1 the results of lifetime measurements for three different oxidation times and three different starting thicknesses of the poly-Si layer are shown. It should be mentioned that the connections between the different measurement points are guidelines, but only the specific indicated oxidation times were applied. If the poly-Si layer is thicker, the effective lifetime increases significantly. This is quite an extreme effect: the lifetime in samples with poly-Si thickness of 25 nm is about 2 ms, while with poly-Si thickness of 65 nm the lifetime is already close to 8 ms. Also, the effect of SiNx hydrogenation is stronger for thicker poly-Si layers. As one can see hardly any lifetime enhancement is observed for 25 nm poly-Si, whereas for poly-Si thickness of 45 nm and 65 nm an increase of at least 4 ms is observed. This improvement is, however, almost completely removed after firing.

For short and intermediate dry oxidation times, the initial charge carrier lifetime is comparable but slightly higher than that of poly-Si for all thicknesses. For very long oxidation times, the lifetime is reduced to close to 0 ms. Hydrogenation does have a small positive effect on the lifetime in the 45 nm and 65 nm dry oxidised samples. However, hydrogenation does not increase the lifetime for the 25 nm dry oxidised samples. After firing the lifetime of the minority charge carriers, is enhanced for all samples, which indicates a good firing stability.

After wet oxidation, the initial lifetime decreases already at short oxidation times. A noteworthy lifetime enhancement takes place after both hydrogenation and firing. The effect is relatively small for the 25 nm poly-Si wet oxidised samples, larger for the 45 nm poly-Si wet oxidised samples, and largest for the 65 nm poly-Si wet oxidised samples. The lifetime in the 30 min wet oxidised 45 nm poly-Si sample after hydrogenation and firing is increased with more than 6 ms. The lifetime in the 45 min wet oxidised 65 nm poly-Si sample after hydrogenation and firing is even increased with about 8 ms.

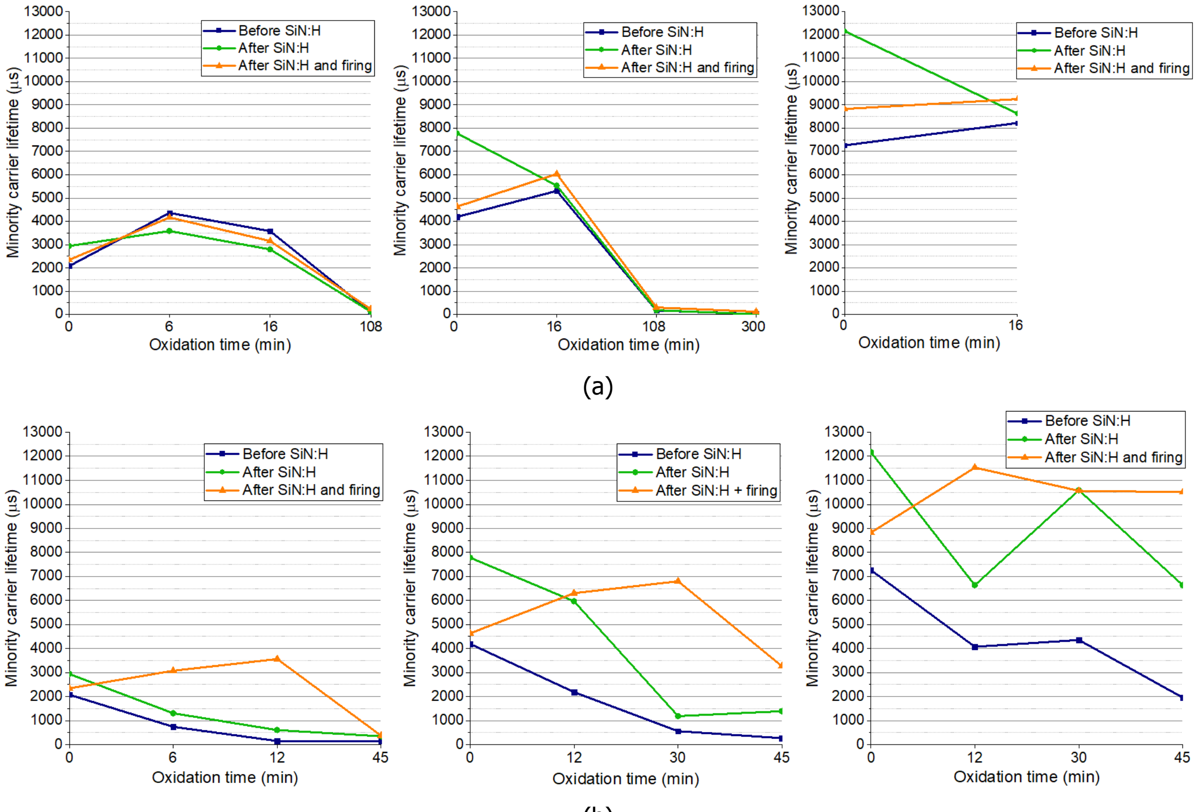

(a)

(b)

Figure 4.1: (a) From left to right the graphs represent the minority carrier lifetimes of the dry oxidised 25 nm, 45 nm and 65 nm samples. The lifetime after $POCl_3$, hydrogenation and firing is indicated by respectively blue, green and orange lines. (b) From left to right the graphs show the minority carrier lifetimes of the wet oxidised 25 nm, 45 nm and 65 nm samples.

4.1.2. Doping Profile and Sheet Resistance (ECV and FPP)

Doping Profile

In figure 4.2 the phosphorus doping profile in the doped unoxidised poly-Si samples is shown. The doping profile in these samples shows similar tail behaviour. The phosphorus concentration is found to be constant at about $3 \times 10^{20}\,\text{cm}^{-3}$ until a certain depth, known as the plateau region. This concentration is equal to the phosphorus solubility limit in silicon for the temperature range of 800 °C to 900 °C. After this region the phosphorus concentration decreases sharply because of the SiO_x blocking mechanism. The sharp decrease is followed by a tail, which can be related to the amount of in-diffusion in the wafer. The higher the phosphorus concentration in this tail, the more in-diffusion has occurred. The tail levels out to a phosphorus concentration which is equal to the known bulk concentration of the wafer, approximately $1.5 \times 10^{15}\,\text{cm}^{-3}$.

In figure 4.3a and 4.3b, the doping profile in the dry and wet oxidised 25 nm doped poly-Si samples are respectively shown. As mentioned in the methodology section, it should be emphasized that the SiO_x layer was removed before ECV measurements were performed. Compared to the unoxidised 25 nm poly-Si sample it is observed that the active phosphorus concentration in the poly-Si is decreased (from approximately $5.0 \times 10^{20}\,\text{cm}^{-3}$ to $2.7 \times 10^{20}\,\text{cm}^{-3}$) in the 6 min and 16 min oxidised samples. After an oxidation time of 108 min no plateau region is present, which indicates that the poly-Si is completely oxidised. Also, a significant amount of in-diffusion takes place when poly-Si is completely oxidised.

The plateau region with a constant phosphorus concentration is not present for any of the wet oxidised samples. Already for the shortest oxidation time, i.e. 6 min, the poly-Si is completely oxidised. Furthermore, less in-diffusion takes place in the wet oxidised samples, compared to the dry oxidised samples with similar initial poly-Si thickness. The longest wet oxidised sample, i.e. 45 min, has the largest amount of in-diffusion.

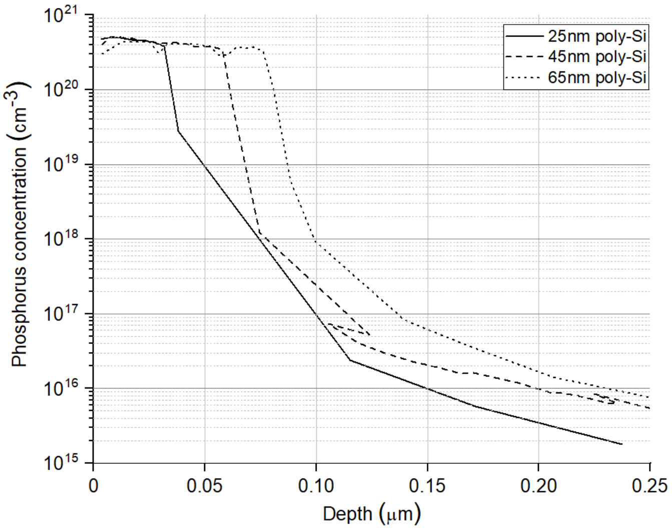

Figure 4.2: Phosphorus concentration profile in as-deposited poly-Si samples. The solid line represents the 25 nm poly-Si sample, the dashed line the 45 nm poly-Si sample and the dotted line the 65 nm poly-Si sample.

In figure 4.3c, shown below, the diffusion profile of the dry oxidised 45 nm poly-Si samples are shown. Similar behaviour as with the dry oxidised 25 nm poly-Si samples is observed. As it is desired to completely oxidise the poly-Si layer and have no remaining poly-Si, the process times during oxidation of 45 nm poly-Si were increased compared to the process times of 25 nm poly-Si. It should be noted that a very small kink is still present for the 108 min oxidised sample, indicated by the green arrow, which is also observed in previous studies. It is suggested that the tunnel oxide is still acting as blocking barrier for phosphorus diffusion, but it is less effective as in short oxidised samples. It is not yet completely understood how the tunnel oxide behaves, but it is assumed that the tunnel oxide is damaged when oxidation times are increased. The tunnel oxide might damaged because of phosphorus pile up in front of the tunnel oxide, whereby stresses are developed and act on the tunnel oxide. In figure 4.3d the wet oxidised 45 nm poly-Si samples are presented. Again, the plateau region with constant phosphorus concentration is disappearing after already short oxidation times. Besides the absence of the plateau region, the doping profile of the wet oxidised samples is similar to the unoxidised 45 nm poly-Si sample.

The doping profiles of the dry oxidised 65 nm poly-Si samples show similar behaviour as the 45 nm and 25 nm dry oxidised poly-Si samples. The active phosphorus concentration does increase in the absorber silicon layer upon increase in oxidation time. The graphical visualization can be found in figures 4.3e and 4.3f. It is noticed that for these samples longer oxidation times are required to oxidise the poly-Si completely compared to 25 nm and 45 nm poly-Si samples. Again, with exception of the plateau region, not much difference is observed in the phosphorus profile between the wet oxidised and unoxidised samples.

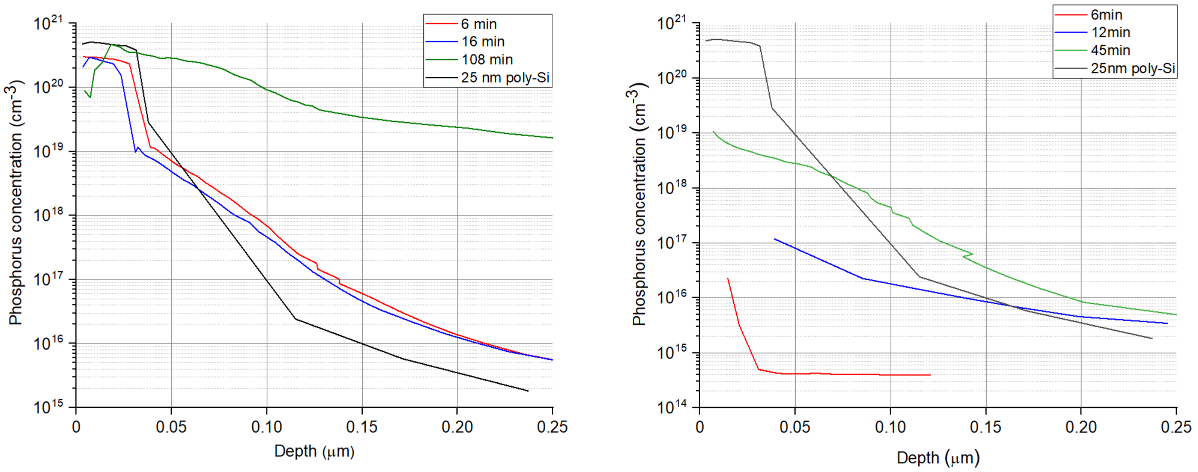

(a) Doping profile of dry oxidised 25 nm poly-Si.

(b) Doping profile of wet oxidised 25 nm poly-Si.

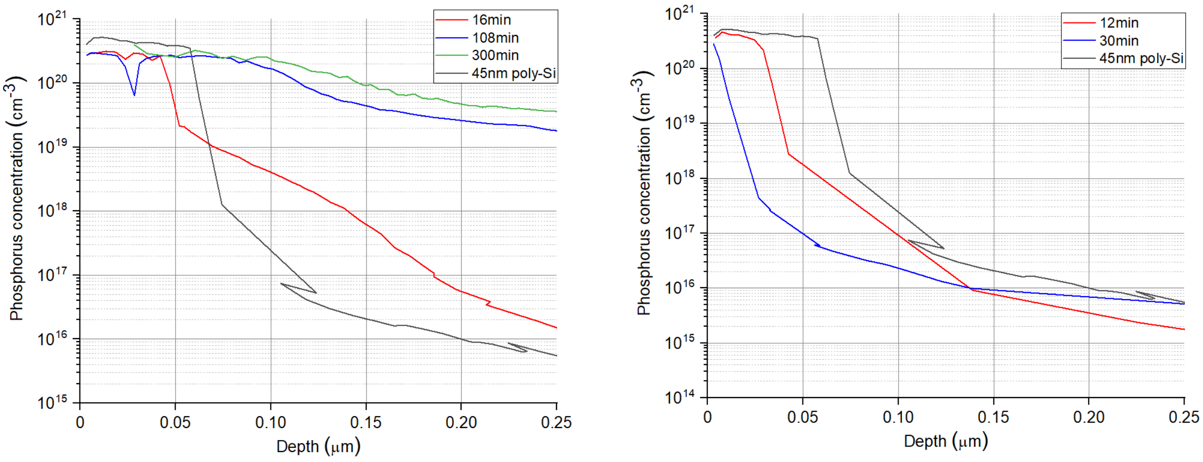

(c) Doping profile of dry oxidised 45 nm poly-Si.

(d) Doping profile of wet oxidised 45 nm poly-Si.

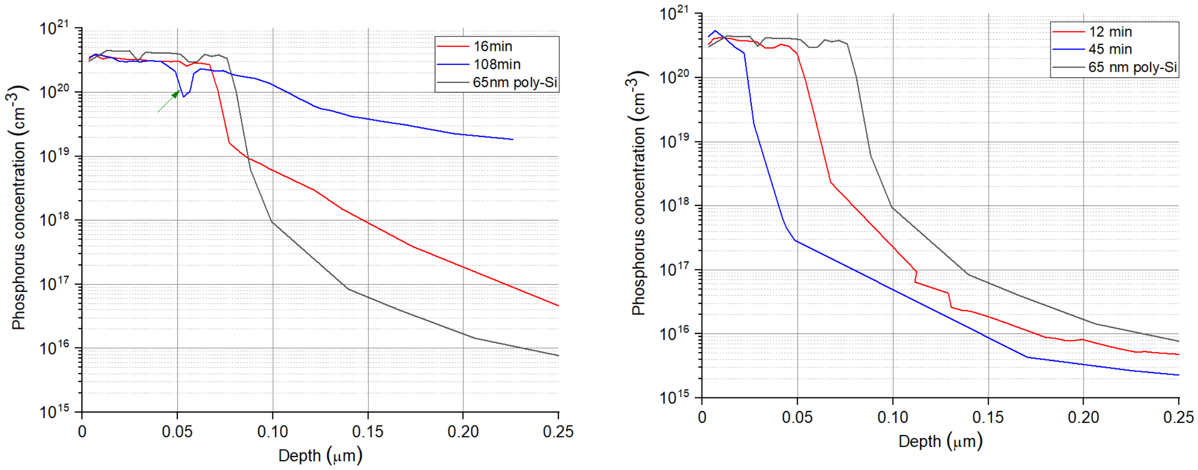

(e) Doping profile of dry oxidised 65 nm poly-Si.

(f) Doping profile of wet oxidised 65 nm poly-Si samples.

Figure 4.3: Phosphorus doping profiles measured by ECV.

Sheet Resistance

The sheet resistance values for the doped poly-Si samples are shown in figure 4.4 below. With increasing poly-Si thickness the sheet resistance of the symmetrical samples decreased. An acceptable sheet resistance of 176 Ω/sq was measured for very thin poly-Si thickness.

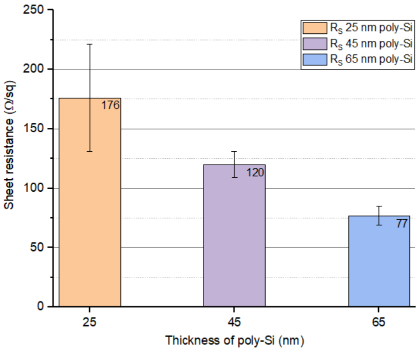

Figure 4.4: Sheet resistance of as-deposited poly-Si samples.

The sheet resistance values after dry oxidation of the poly-Si samples are shown in figure 4.5 below. The sheet resistance of the dry oxidised samples is decreasing upon an increase in oxidation time. The effect is largest when the oxidation times are increased to 108 min. This behaviour was also analysed with QSSPC, which showed a similar trend.

The sheet resistance values of the wet oxidised samples are represented in figures 4.8 and 4.9 below. The 25 nm and 45 nm poly-Si wet oxidised samples first show an increase in sheet resistance when oxidation time is increased, but upon further oxidation the sheet resistance is decreased. The decrease in sheet resistance is observed after 45 min. This behaviour is not observed for the 65 nm poly-Si sample where oxidation times up to 30 min result in an increase of sheet resistance.

The contribution of the silicon oxide to the sheet resistance is estimated by measuring the samples sheet resistance with and without silicon oxide. The results of this experiment are shown for 25 nm dry oxidised and 25 nm wet oxidised in figure 4.10 and 4.11. Although the error in the measurements was quite significant (especially in the wet oxidised samples), the error was constant for at least two measurements. For example, the standard deviation for the 16 min dry oxidised 25 nm poly-Si sample with and without was about 150, while for the 6 min wet oxidised sample the standard deviation was about 100. The sample with a silicon oxide layer has lower resistance (better lateral conductivity) than the sample without a silicon oxide layer (slightly worse lateral conductivity). The values of the sheet resistance of the dry oxidised 25 nm poly-Si samples remained in the same range before and after removal of the oxide layer.

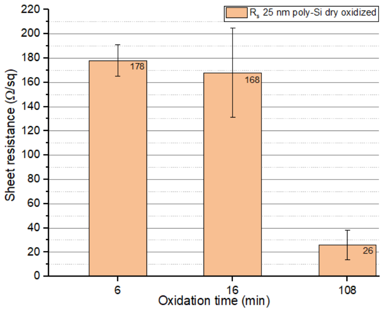

Figure 4.5: Sheet resistance of 25 nm poly-Si dry oxidised poly-Si samples.

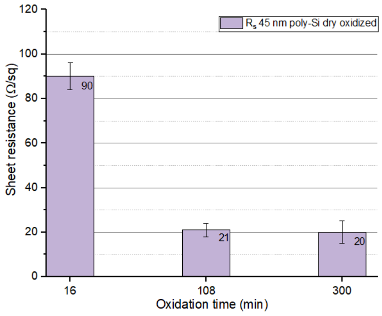

Figure 4.6: Sheet resistance of dry oxidised 45 nm poly-Si samples.

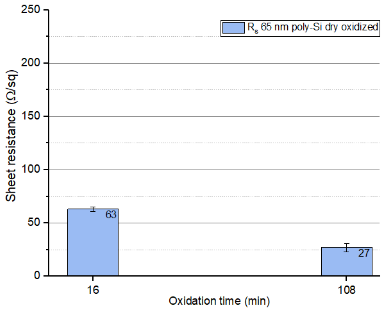

Figure 4.7: Sheet resistance of dry oxidised 65 nm poly-Si samples.

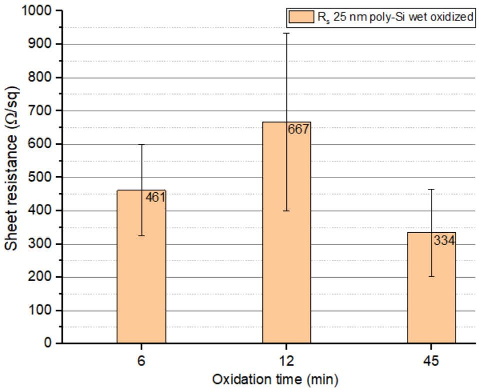

Figure 4.8: Sheet resistance of wet oxidised 25 nm poly-Si samples.

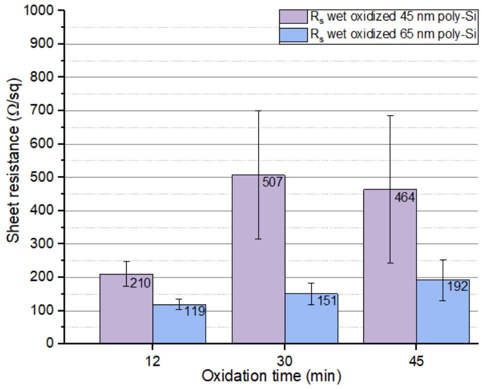

Figure 4.9: Sheet resistance of 45 nm and 65 nm poly-Si wet oxidised poly-Si samples.

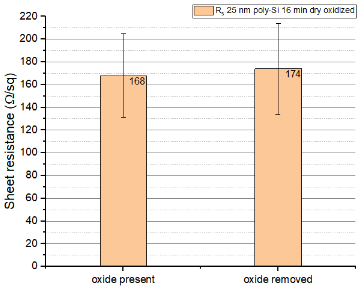

Figure 4.10: Sheet resistance values of dry oxidised 25 nm poly-Si samples, measured before and after removal of the oxide layer.

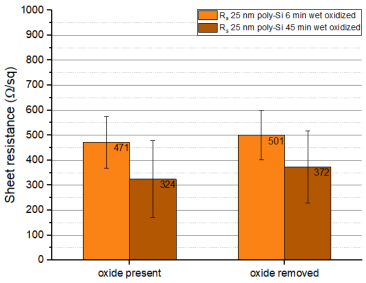

Figure 4.11: Sheet resistance values of wet oxidised 25 nm poly-Si samples, measured before and after removal of the oxide layer.

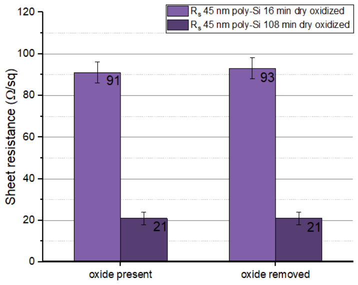

Figure 4.12: Sheet resistance values of dry oxidised 45 nm poly-Si samples, measured with and without oxide layer.

4.1.3. Thickness (ECV, SEM, SE)

ECV

The thickness of the poly-Si layers is estimated from the doping profile measurements. As explained in section 4.1.2 the thickness of the poly-Si layer is indicated by the depth of the plateau region. In figure 4.13 guidelines are indicated to show the thickness of all poly-Si layers. Table 4.1 shows information about the expected thicknesses known from previous studies and the through ECV estimated thicknesses. Since deposition time is known, the growth rate on the polished CZ wafers was determined to be 2.4 nm min^{-1}, 2.8 nm min^{-1} and 2.7 nm min^{-1} for respectively 25 nm, 45 nm and 65 nm. These values are similar to the deposition rate of poly-Si on textured CZ wafers (2.8 nm min^{-1}).

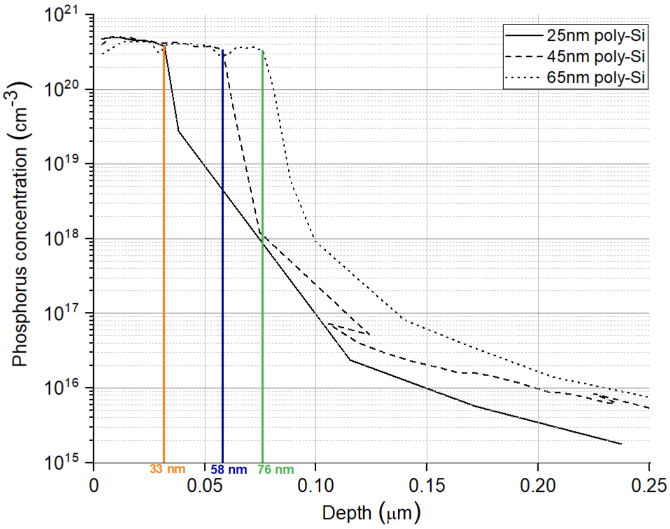

Figure 4.13: Doping profile in unoxidised poly-Si samples with guidelines for thickness estimation.

Table 4.1: Overview of expected thickness and estimated thickness by ECV.

Expected thickness (nm)	**Estimated thickness** (nm)	**Growth rate**
25	33	2.4
45	58	2.8
65	76	2.7

SEM

In figure 4.14 below, an SEM image of a 16 min dry oxidised 65 nm poly-Si sample is shown from which the thickness of the SiO_x and remaining poly-Si layer can be determined. The SiO_x layer was estimated to be on the order of 30 nm, and the remaining poly-Si thickness on the order of 80 nm. The thickness of the remaining poly-Si layer is in agreement with the estimated thickness from ECV measurements, which indicated a remaining poly-Si thickness of about 70 nm.

In figure 4.15 a cross-sectional SEM image is shown of a 65 nm poly-Si 45 min wet oxidised sample. From this cross-sectional image several areas (layers) can be distinguished. The top layer is the SiO_2 layer which has a thickness in the order of 200 nm. The layer below is the remaining poly-Si and has a thickness of about 40 nm. The high brightness areas are due to charging of less conductive areas (e.g. silicon tunnel oxide below the poly-Si layer.).

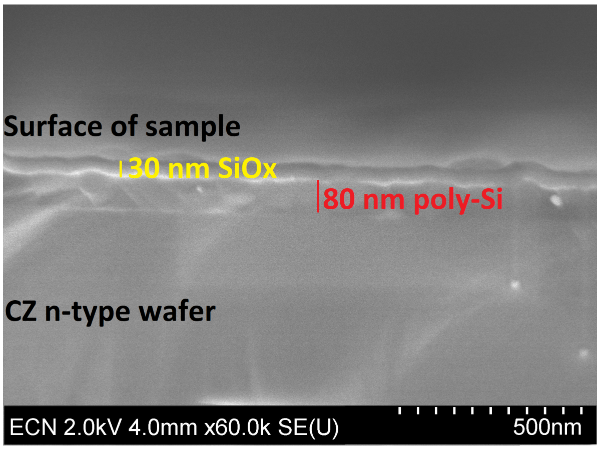

Figure 4.14: SEM cross-section of 16 min dry oxidised 65 nm poly-Si sample.

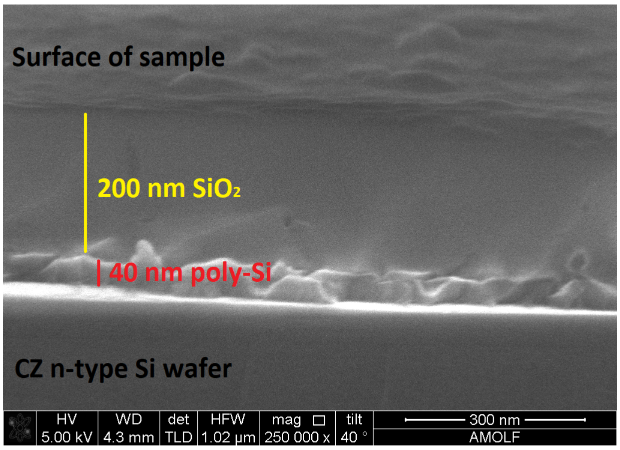

Figure 4.15: SEM cross-section of 45 min wet oxidised 65 nm poly-Si sample.

4.1.4. Oxide Content (EDX, XPS, FTIR)

Several methods have been used to determine the oxide fraction in the SiO_x layer. For the post-oxidised samples EDX, XPS and FTIR measurements were performed to determine the oxide fraction.

EDX

In figure 4.16 the elemental distribution of the 30 min wet oxidised 45 nm poly-Si sample is shown. The oxygen and silicon weight percentages in the sample are respectively 14.2% and 85.8%. The silicon peak is caused by the absorber layer, the remaining poly-Si layer (confirmed by ECV results, see for example figure 4.3c) and the silicon in the silicon oxide. It should be noted that the weight percentage oxide is the fraction oxygen in the entire symmetrical sample. Three types of silicon are contributing to this percentage, namely Si in the SiO_x layer, Si from the poly-Si and Si present in the substrate layer. With this technique it was possible to quickly confirm the presence of oxide, however exact composition can not be determined.

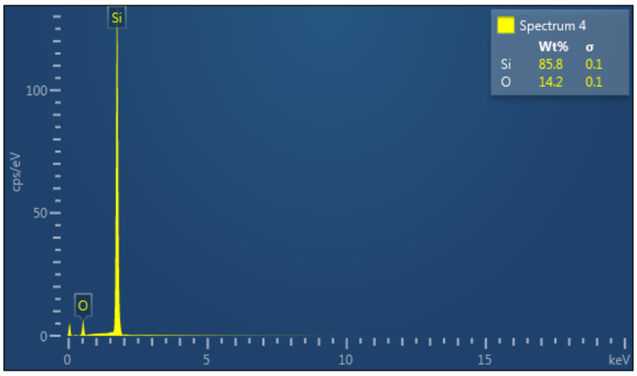

Figure 4.16: EDX spectrum showing the fractions of oxygen and silicon in 30 min wet oxidised 45 nm poly-Si sample.

XPS

In figure 4.17 the XPS spectrum of a 45 min wet oxidised 65 nm poly-Si sample is shown. Silicon is responsible for the appearance of three peaks in this spectrum; around 99 eV, 103 eV (Si2p) and 150 eV (Si2s). These peaks may be attributed to the Si^{4+} state which is indicating the Si-O bond [48]. The very small, though noteworthy peak, is present at 99 eV corresponds to the Si^{0+} state which is related to the presence of Si-Si bonds. Furthermore, a large peak exists around 530 eV (O1s), that corresponds to the Si-O bond [49]. From these peaks it was possible to calculate the surface composition. The surface SiO_x layer consists of 67% oxygen and 33% silicon, which means that stoichiometric SiO_2 is developed during 45 min wet oxidation of 65 nm poly-Si.

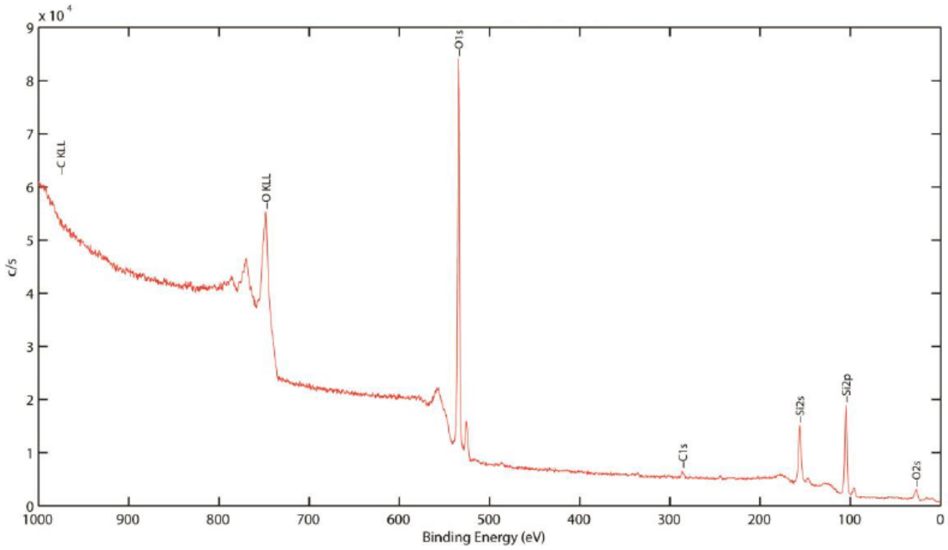

Figure 4.17: XPS spectrum of 45 min wet oxidised 65 nm poly-Si sample.

Fourier Transform Infrared Spectroscopy

The FTIR spectra of the 45 nm poly-Si wet oxidised poly-Si samples are shown in figure 4.18. All samples show obvious peaks at wavenumbers of about 1085 cm^{-1} and 830 cm^{-1}. The longer the oxidation times, the larger these absorption peaks are. The peak at 830 cm^{-1} shows a small shift towards lower wavenumbers when oxidation times are increased. Also, all samples show a shoulder at about 1140 cm^{-1}, which is characteristic for SiO_2. The FTIR measurements confirmed the presence of Si-O chemical bonds for all oxidation times.

With FTIR, the effect of hydrogenation was also determined. In figure 4.19 both an unhydrogenated and hydrogenated wet oxidised 65 nm poly-Si sample are shown. The hydrogenated sample shows an extra small peak at 2250 cm^{-1}, attributed to Si-H stretching vibration, which is absent for the unhydrogenated sample [50] [51].

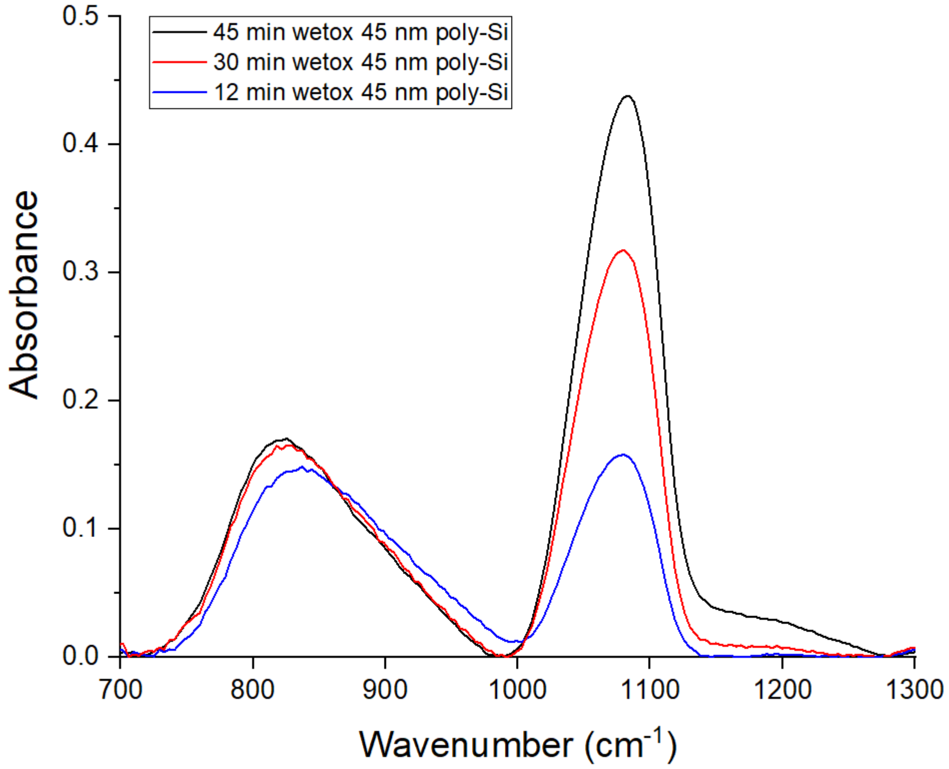

Figure 4.18: FTIR absorbance spectra of wet oxidised 45 nm poly-Si samples. An increase in oxidation time increases the Si-O absorbance peak because of increased SiO_2 thickness.

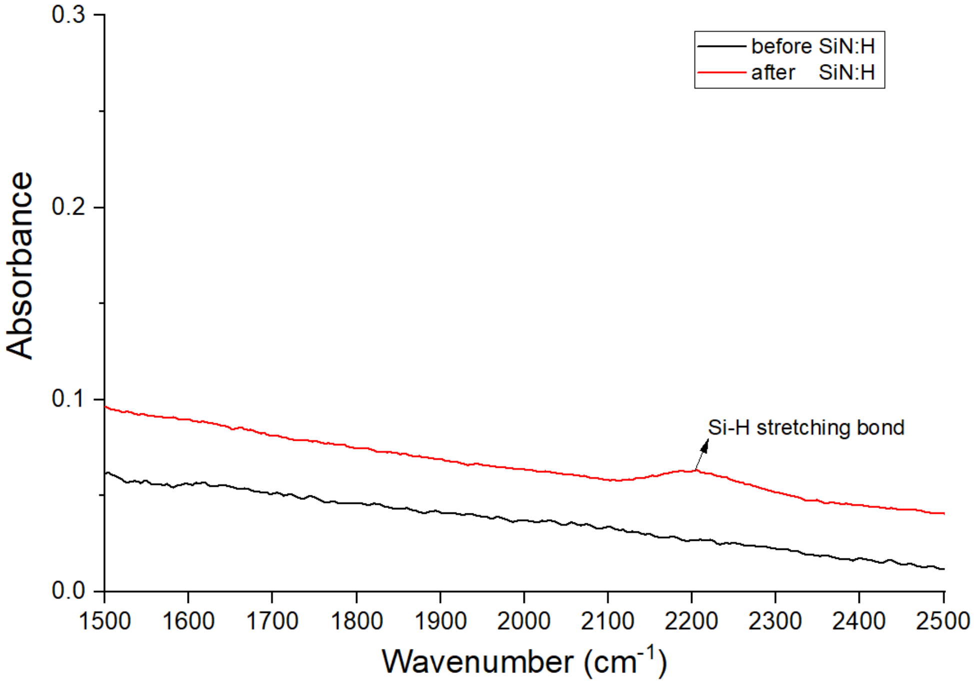

Figure 4.19: FTIR absorbance spectra of 30 min wet oxidised 65 nm poly-Si samples, before and after hydrogenation.

4.1.5. Morphology and Crystallinity (SEM, XRD)

SEM

In figure 4.20 an SEM top view image of the doped 25 nm poly-Si sample is shown and in figure 4.21 an SEM top view of a 30 min wet oxidised 45 nm poly-Si sample is shown. It should be noticed that wet oxidation does not affect the crystalline grain structure of the layer. This is a promising observation since crystallinity is desired in order to develop properly conducting layers. The grain size in the poly-Si sample is mostly smaller than 100 nm, whereas the grain size of the wet oxidised samples is slightly increased to values around 100 nm. This is indicated by the red sticks in both figures. Also, an increased amount of bright spots are visible in the wet oxidised sample compared to the 25 nm doped poly-Si sample. As the bright spots are related to less conductive areas in the material, it confirms that oxidation was successful and oxygen is incorporated into the poly-Si layer by formation of Si-O bonds.

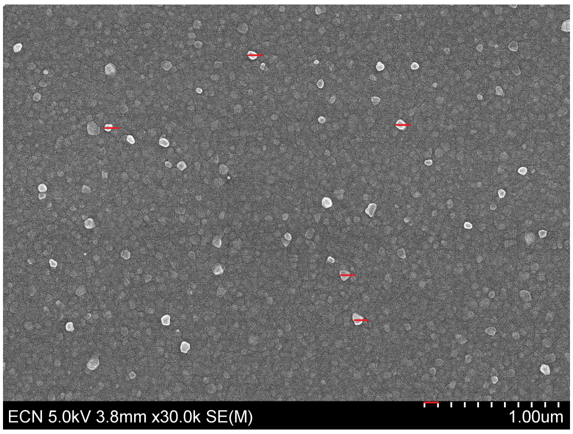

Figure 4.20: SEM top view of 25 nm n^+ poly-Si.

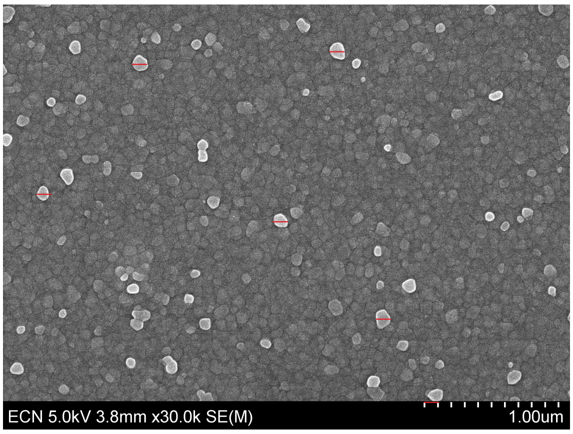

Figure 4.21: SEM top view of 30 min wet oxidised 45 nm poly-Si sample.

XRD

The X-ray Diffraction pattern of a 12 min 45 nm poly-Si wet oxidised sample is shown in figure 4.22 below. The Si (400) peak is completely caused by the substrate. The left XRD image shows the result of the conventional XRD measurements, where the right XRD image shows the result of the parallel beam XRD. Depending on the type of XRD technique applied, the silicon(oxide) peaks may be shifted. In the appendix the datasheets are added that provide information about the silicon and silicon oxide patterns for each technique. The black pattern is corresponding to the X-ray response of the analysed sample. The red and blue sticks indicate, respectively, the characteristic peak positions of poly-Si and silicon oxide. The relatively large and wide black peaks in the left image are due to the (400) oriented substrate reflections. In the right image the background was subtracted and showed that mainly poly-Si was present with orientation. The cubic structure of SiO is less symmetric than of Si and some extra small peaks might be present ($2\theta = 32.8°$, $2\theta = 58.6°$, $2\theta = 78.4°$) but were not found. From the XRD spectra it was also possible to give an estimation of the grain size (Scherrer equation) and was calculated to be in the order of 30 nm. Please note that this is the grain size of the poly-Si grains, since no contribution of silicon oxide was found.

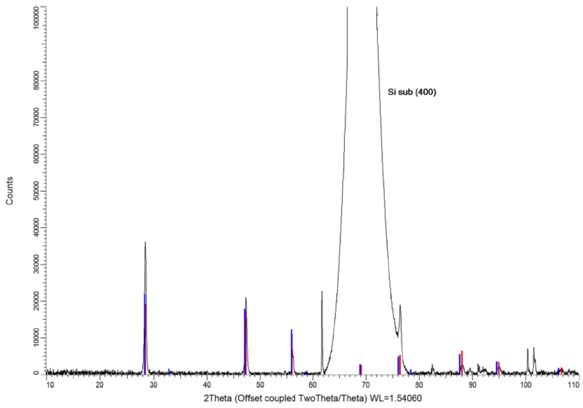

Figure 4.22: XRD spectrum of wet oxidised 45 nm poly-Si sample, measured in conventional mode.

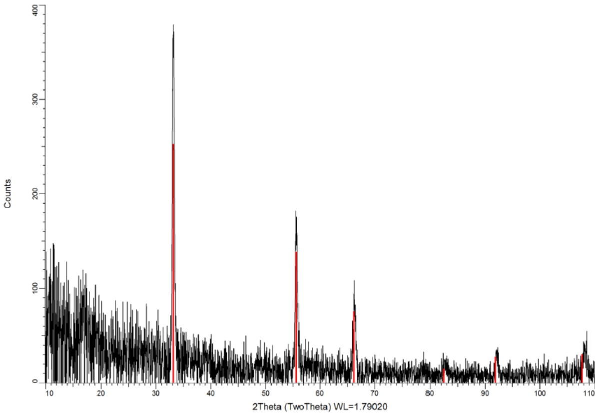

Figure 4.23: XRD spectrum of wet oxidised 45 nm poly-Si sample, measured by parallel beam.

4.2. Discussion

The initial poly-Si thicknesses were assumed to be 25 nm, 45 nm and 65 nm based on known procedures. However, from ECV measurements the thicknesses were estimated to be respectively 33 nm, 58 nm and 76 nm. To be consistent with the previous sections, in the remainder of the thesis the assumed poly-Si thicknesses are used to refer to certain samples. First the observations for unoxidised samples will be discussed, followed by the observations for dry oxidised samples and subsequently the observations for wet oxidised samples.

4.2.1. As-Deposited Poly-Si Samples

Taking into account both the lifetime results and the phosphorus profiles of the poly-Si layers, the observed trend in minority carrier lifetime as a result of poly-Si thickness could be related to the field-effect. The chemical (surface) passivation at the interface is most likely not thickness dependent, because it is based on hydrogenated SiO_x passivation of the same thermal oxide. However, the field-effect passivation is reduced when the poly-Si layer is thinner (absolute amount of active dopants is reduced). Moreover, the ECV results demonstrated that a comparable amount of in-diffusion has taken place in all poly-Si samples, which excludes a possible explanation of excessive doping in the silicon wafer in less thick poly-Si samples. Because ECV showed equal in-diffusion in the samples, Auger recombination has equal contribution in all samples with different poly-Si thickness. Thus, most likely the passivation quality is enhanced when the poly-Si thickness is increased, due to the field effect.

SiN_x capping of these layers gave a significant increase in lifetime, but after firing of the poly-Si samples, the minority carrier lifetime was reduced again to nearly the initial level. During firing hydrogen gets untrapped from the dangling bonds and diffuses through the poly-Si into the environment, whereby hydrogen passivation is reduced. As out-diffusion of hydrogen occurs during firing of poly-Si, unoxidised poly-Si samples are not firing stable [52].

The sheet resistance of the samples with unoxidised doped poly-Si layers show acceptable values in order to be applicable as passivating contact layer. Although out of scope of this research, it is interesting to investigate the implementation of these thinner poly-Si layers in, for example, the PERPoly solar cell.

4.2.2. Dry Oxidised Poly-Si Samples

The phosphorus concentration profile in the dry oxidised poly-Si samples shows that a significant amount of in-diffusion occurs. This indicates that phosphorus prefers to diffuse into the substrate layer, instead of diffusing to interstitial sites in the poly-Si or to the SiO_2 layer. From previous studies it is known that in-diffusion results in an excess of dopants in the wafer, which causes an increase in Auger recombination [53]. The increase in Auger recombination reduces the minority carrier lifetime, which was confirmed by the QSSPC measurements. Also, it is worthwile to note that the P-Si bond is shorter than the Si-Si bond, which induces local deformations upon phosphorus incorporation [54]. If high phosphorus concentrations are present this will affect the passivation quality of the SiO_x layer, as defects increase Shockley-Read-Hall recombination. High concentration of phosphorus in the poly-Si causes both Auger and SRH recombination, which mostly leads to parasitic absorption, but not to a decrease in the effective lifetime measured with the QSSPC tool.

After short dry oxidation times of every poly-Si sample only a small amount of in-diffusion is observed, which leads to an improvement in minority carrier lifetime. However, after long dry oxidation times an excess of dopants is in-diffused which has a detrimental effect on the minority carrier lifetime. Possibly, a small additional drive-in compensates for the lack of phosphorus doped region due to the poly-Si layer being too thin (lower absolute electrical active phosphorus concentration compared to thick poly-Si layers). If a small amount of phosphorus diffuses into the silicon wafer, the doped poly-Si region is slightly extended with the highly doped silicon wafer. A thicker doped layer enhances the minority carrier lifetime, as long as it is not balanced out by an increase in Auger recombination. The lifetime in the short oxidised 25 nm poly-Si layer could therefore possibly be enhanced to the level of the 45 nm poly-Si layer. The same behaviour is observed in the 45 nm and 65 nm dry oxidised samples. If the oxidation times for dry oxidation are increased to a certain transition value, the phosphorus profile does not show the kink-tail diffusion profiles anymore. The poly-Si is then completely oxidised and the phosphorus is driven into the substrate wafer.

The increase in lifetime after hydrogenation of the 45 nm and 65 nm poly-Si short dry oxidised samples may be due to hydrogen atoms trapped at the silicon surface (dangling bonds). The increased minority carrier lifetimes are ascribed mainly to hydrogen termination of silicon dangling bonds at the surface. Furthermore, SiN_x can induce additional field-effect passivation, because of its high positive fixed charge density of the order of 1011 cm^{-2} [55]. In contrast, after hydrogenation of the 25 nm dry oxidised poly-Si layer the lifetime is reduced. Only if hydrogenation leads to a reduction of defects (e.g. hydrogen trapped at dangling bonds), the hydrogenation will enhance surface passivation. Although not accurately determined, the SiO_x layers must result in similar thickness for the same oxidation time. So, the only difference between the different dry oxidised samples is the remaining poly-Si thickness. Based on this knowledge, it is suggested that a minimum remaining poly-Si thickness is required for effective hydrogenation of dry oxidised samples. If the remaining poly-Si thickness is less than approximately 30 nm the hydrogen will more easily diffuse to the environment, because of a smaller diffusion barrier compared to thicker poly-Si layers, that are present for shorter oxidation times or thicker starting poly-Si layers.

After firing of the dry oxidised samples, the minority carrier lifetime remained stable or even slightly increased. The oxide layer on top of the poly-Si probably acts as a blocking layer, so that the hydrogen remains trapped at the surface and out-diffusion is minimized. Therefore, in dry oxidised samples hydrogen passivation remains active, while the hydrogen may diffuse out for the poly-Si layers during firing. Another suggestion is that the hydrogen can decrease the defect density in the silicon oxide layer. For example, non-bridging oxygen hole centers (NBOHCs) may be present which are prone sites for hydrogen trapping [56]. This reduces the amount of defects in the silicon oxide layer and thus reduces SRH recombination. The minority carrier lifetime improvement seems more pronounced in wet oxidised samples, compared to dry oxidised samples, because of its more porous structure. The more porous wet oxidised structure contains more non-bridging oxygen hole centres than the dense dry oxidised structure which can be terminated by hydrogen during the firing step. Herewith, hydrogen may provide an additional very efficient passivation of defects in the SiO_2 layer.

The sheet resistance values of the dry oxidised samples tends to decrease with oxidation times. If the symmetrical samples are exposed to elevated temperatures (900 °C) for a longer period, most likely inactive phosphorus diffuses from the poly-Si towards active sites in unsaturated regions deeper in the wafer causing an increase in lateral conductivity. Also, the SiO_2 layer may form a capping layer which acts as barrier for phosphorus out-diffusion. It becomes energetically favourable for phosphorus to diffuse in the wafer.

4.2.3. Wet Oxidised Poly-Si Samples

Wet oxidised poly-Si samples showed a decrease in minority carrier lifetime upon oxidation time. In contrast to the dry oxidised samples, in the wet oxidised samples the minority carrier lifetime was significantly increased after hydrogenation and firing. If no in-diffusion took place at the firing step, the firing of the wet oxidised samples significantly enhanced the minority carrier lifetime. For 12 min wet oxidation of 45 nm poly-Si and 30 min wet oxidation of 65 nm poly-Si firing has much less effect on the minority carrier lifetime, compared to firing of other wet oxidised samples. For these samples the minority carrier lifetime was already quite close to the maximum value. If the hydrogen is already terminated at most dangling bonds during the hydrogenation step, firing does not enhance hydrogen passivation. The reason why hydrogen already is trapped at most dangling bonds for these samples directly after hydrogenation remains unknown. It is out of scope of this study to investigate this behaviour in detail.

The amount of phosphorus in-diffusion taking place in the 25 nm wet oxidised samples is small compared to the in-diffusion taking place in the 25 nm dry oxidised samples. Besides the 25 nm wet oxidised samples, no in-diffusion takes place in the 45 nm and 65 nm wet oxidised samples. The fact that in-diffusion does not occur in wet oxidation is explained by thermodynamics and kinetics. The dry oxidation process occurs at higher temperatures than the wet oxidation process (900 °C and 800 °C) and thus more in-diffusion of phosphorus takes place, compared to the wet oxidation process, in the same amount of time. However, since still some in-diffusion takes place for these samples upon increasing the oxidation time, the excessive dopant concentrations causes increased Auger recombination. This explains the decrease in minority carrier lifetime in observed in 25 nm wet oxidised samples.

The sheet resistance values of the 25 nm and 45 nm poly-Si wet oxidised samples increase with short oxidation times. The sheet resistance values of the 65 nm poly-Si wet oxidised sample do not show a reduction in sheet resistance when oxidation times are increased to 45 nm. Increased thickness of poly-Si most likely require longer oxidation times to cause similar type of in-diffusion as is observed for the 25 nm and 45 nm poly-Si.

It was expected that a phosphorus peak was present at 130 eV in the XPS spectrum of 45 min wet oxidised 65 nm, caused by Si-P bonds. Due to relatively low phoshporus concentrations the signal is weak and due to the plasmon loss peak of Si 2p photoelectrons the P 2p peak is overlapped. By increasing the dwell time it will be possible to detect the P 2p peak and thus indicate whether Si-P bonds are created [57].

4.3. Conclusion

The research question that can be answered after this experiment is: *Is post-oxidation of doped poly-Si a successful method to produce doped SiO_x layers?* The question will first be answered for the dry-oxidised samples, after which the question will be answered for the wet-oxidised samples. For both oxidation methods, the obtained silicon oxide was close to stoichiometric and thus significantly enhances the transparency compared to current used emitter layers (such as poly-Si).

The following conclusions can be drawn for the dry oxidised samples:

- Dry oxidation of doped poly-Si at 900 °C causes too much in-diffusion, leading to Auger recombination and thus low minority carrier lifetimes.
- The high minority carrier lifetimes (>8 ms) in the symmetrical samples were caused by the presence of remaining poly-Si.
- Dry oxidation of doped poly-Si does not result in phosphorus incorporation in the SiO_x layers.
- SiO_2 layer obtained by dry oxidation are firing stable.

Overall, post-oxidation of doped poly-Si by means of dry oxidation is not a promising route to produce doped SiO_x layers.

The following conclusions can be drawn for the wet oxidised samples:

- Wet oxidation of doped poly-Si at 800 °C shows excellent minority carrier lifetime (>10 ms).
- Wet oxidation of doped poly-Si results in phosphorus incorporation in the SiO_x.
- Firing enhances the minority carrier lifetimes, most likely because of activation of hydrogen passivation in SiO_x.
- The lateral conductivity needs to be enhanced by addition of conductive layers.

Overall, post-oxidation of doped poly-Si by means of wet oxidation seems a promising route to produce doped SiO_x layers, however some improvements are necessary to be applicable as passivating contact layer.

5

Post-Doping of LPCVD Poly-SiO$_x$

This chapter describes the results of the post doping experiment, in which poly-SiO$_x$ layers, grown by in-situ oxidation in the LPCVD furnace, are doped using a $POCl_3$ treatment. The results in terms of both the structural characterization methods (SEM, FTIR, SE and XRD) and electrical characterization (ECV, QSSPC, Sherescan and PL) methods, are described here.

5.1. Results

5.1.1. Minority Carrier Lifetime in Post-Doped Poly-SiO$_x$

In figure 5.1 the results of the minority carrier lifetime measurements for different N_2O/SiH_4 ratios and different oxidation times are shown (left and right). Both of the graphs, for 90 min and 120 min deposition times, display a slight increase in initial minority carrier lifetime as a function of increasing N_2O/SiH_4 ratio (before hydrogenation). The SiN:H hydrogenation step improves the minority carrier lifetimes slightly. The minority carrier lifetime in silicon oxide layers obtained by higher gas flow ratios is slightly more improved by hydrogenation than in silicon oxide layers obtained by low gas flow ratios. A significant increase in minority carrier lifetime can be observed after the firing step, showing an excellent firing improvement. The effect of increase in minority carrier lifetime after firing is the largest in the samples that were deposited by largest N_2O/SiH_4 flow. The effect of an increase in deposition time can be clearly seen, when the N_2O/SiH_4 ratio is kept constant. If this gas flow ratio is kept constant, but deposition time is increased, the minority carrier lifetime is significantly decreased. In all cases an increase in deposition time from 90 min to 120 min is always detrimental for the minority carrier lifetime. When the N_2O/SiH_4 ratio is increased from 0.33 to 0.58 the minority carrier lifetime is increased, whereas this enhancement deteriorates when deposition times are increased from 90 min to 120 min.

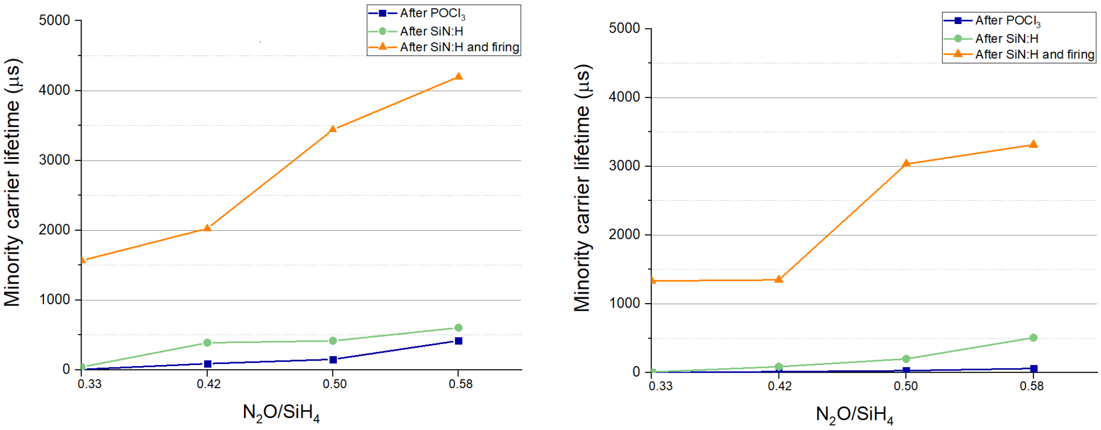

Figure 5.1: Minority carrier lifetime in the post-doped symmetrical samples. In the left graph the minority carrier lifetime of the 90 min samples are shown and in the right graph the minority carrier lifetime of the 120 min samples.

5.1.2. Doping Profile and Sheet Resistance(ECV and FPP)

Doping Profile

As with the post-oxidised samples, also for post-doped SiO_x layers, ECV measurements were done in order to obtain information about the phosphorus in-diffusion. One test sample was prepared by 30 min deposition with 0.33 gas flow ratio. The result of the ECV measurement after doping of this sample is shown in figure 5.2a. Please note that prior to the ECV measurement, the SiO_x layer was removed. This ECV measurement shows that the phosphorus diffuses easily through the SiO_x layer and into the wafer. Surprisingly, a plateau-like region is formed at the surface of the sample. In figures 5.2a and 5.2b the phosphorus concentration profile of the samples with varying deposition times, but constant N_2O/SiH_4 ratio, of respectively 0.33 and 0.42 are shown. The most clear observation is that SiO_x layers deposited in 120 min with a gas flow ratio of 0.33 and 0.42 show some sort of kink- and tail profile. A deposition time of 90 min results in a constant phosphorus doping profile with a phosphorus concentration of about $5 \times 10^{14}\,cm^{-3}$ (substrate level). For a deposition time of 120 min the phosphorus concentration is higher level at the surface, but decreases rapidly in 25 nm to the same level as the SiO_x sample with 90 min deposition time. Down to a depth of about 10 nm an increase in active phosphorus concentration is observed for the 120 min sample. At larger depths the phosphorus concentration decreases again to a level equal to the bulk concentration. The phosphorus concentration in the 90 min deposited sample has an almost constant level of about $5 \times 10^{14}\,cm^{-3}$ (equal to the substrate phosphorus concentration). Please note that the measurements were stopped when the phosphorus concentration remained constant. The phosphorus concentration stopped changing when depths of about 100 nm were reached by the etching liquid, after which the measurements were stopped.

In figure 5.2c and 5.2d the phosphorus concentration in the samples with gas flow ratios, of 0.50 and 0.58 respectively, and for both 90 min and 120 min is shown. The phosphorus profiles for both ratios show similar behaviour. The phosphorus concentration is slightly higher at the surface than at increased depths. Although small, the increase in phosphorus concentration at the surface is interesting to notice. It indicates a small amount of in-diffusion after doping of the in-situ oxidised samples. The phosphorus concentration in the SiO_x layer deposited by a gas flow ratio of 0.50 shows a similar profile as in the samples which were deposited with a 0.58 ratio. A slightly higher concentration is observed at the surface, which is gradually decreasing up to a level equal to the substrate phosphorus concentration. Again, this may be attributed to a small amount of in-diffusion in the wafer.

Sheet Resistance

Sheet resistance measurements of the post-doped SiO_x layers did not show good results, because of too high contact resistance. The oxygen incorporation in the silicon during deposition, is responsible for a large insulating fraction. In order to successfully measure the sheet resistance in the post-doped SiO_x layers, the conductivity needs to be enhanced significantly.

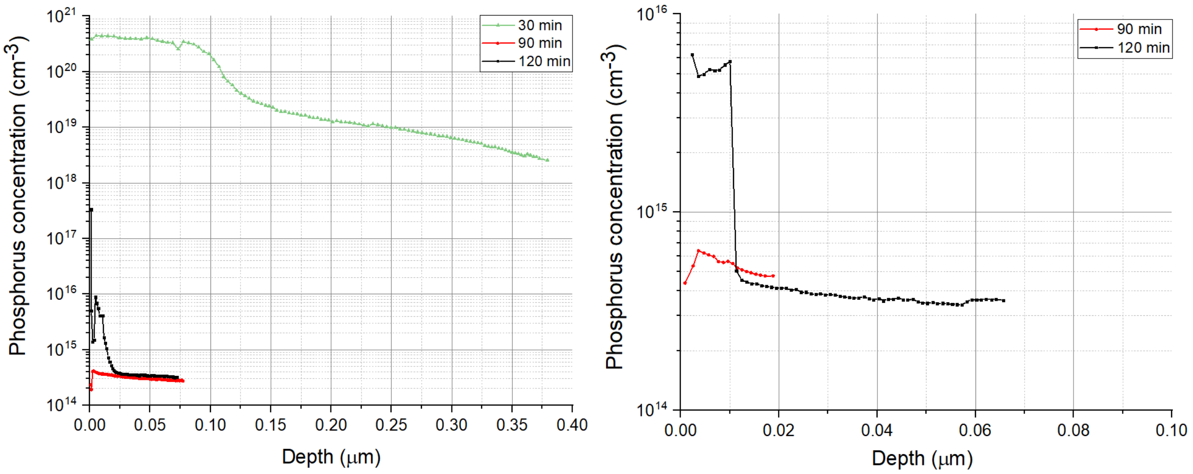

(a) Gas flow ratio of 0.33.

(b) Gas flow ratio of 0.42.

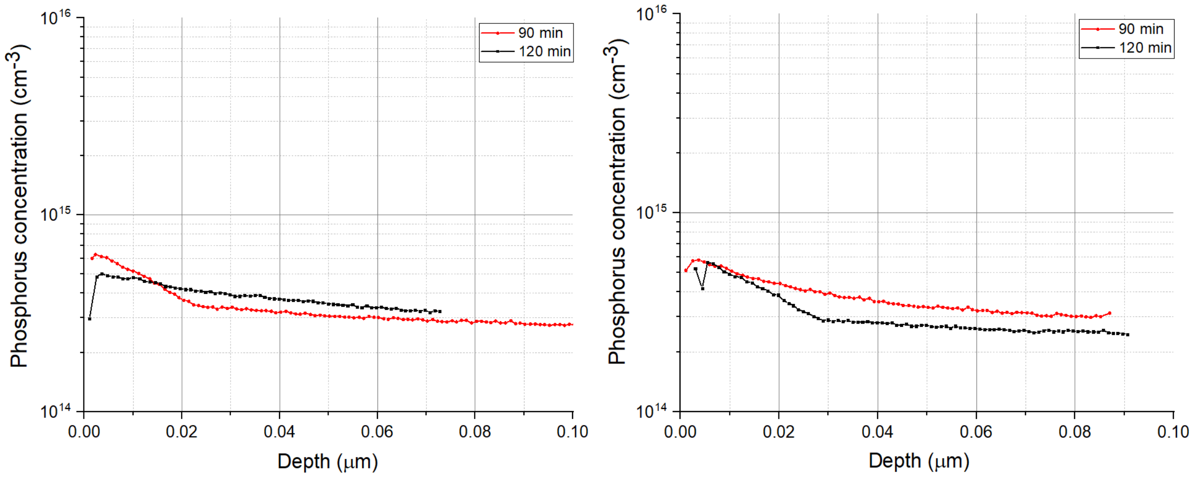

(c) Gas flow ratio of 0.50.

(d) Gas flow ratio of 0.58.

Figure 5.2: Doping profile in silicon wafer to show amount of in diffusion after doping of the SiO_x layers obtained by four different gas flow ratios. The green solid line represents the 30 min sample, the red solid line represents the 90 min sample and the black solid line the 120 min sample.

5.1.3. Thickness Determination by SEM and SE

Thickness Determination by SEM

The thickness of the deposited SiO_x layers by means of in-situ oxidation was estimated from SEM images. The thickness of a hydrogenated sample, deposited in 90 min and using 0.58 gas flow, is shown in figure 5.3, deposited in 90 min. The top layer is about 75 nm SiN:H. The SiO_x layer underneath the SiN:H layer is shown to be in the order of 45 nm. From this thickness estimation it is possible to indicate the growth rate of samples deposited by a ratio of 0.58, which is about 0.51 nm min^{-1}.

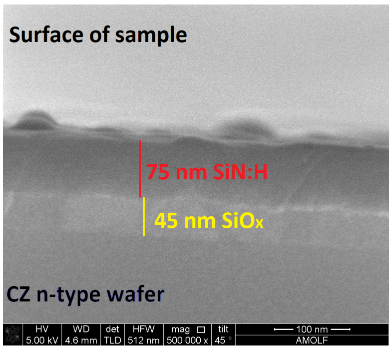

Figure 5.3: SEM cross-section of hydrogenated in-situ deposited sample, with thickness indication of the deposited layers. The applied gas flow ratio was N_2O/SiH_4=0.58 for 90 min.

Thickness Determination by SE

From ellipsometry modelling it was also possible to give an estimation of the SiO_x layer thicknesses. The thickness of the SiO_x layers was estimated for all ratios and the results are shown in 5.15. The SiO_x layers deposited in 90 min showed thicknesses in the range of 96 nm to 50 nm and the SiO_x layers deposited in 120 min showed thicknesses in the range of 67 nm to 150 nm. Clearly, the N_2O/SiH_4 ratio has an influence on the growth rate. An increase in N_2O decreases the deposition rate of the SiO_x layer.

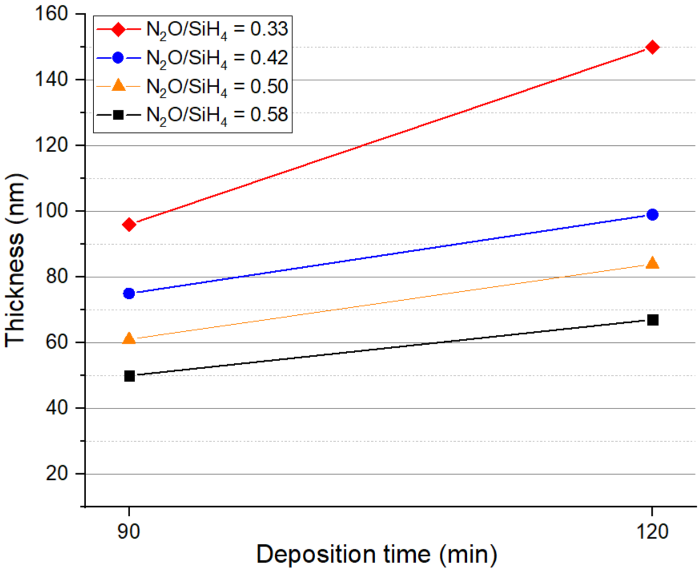

Figure 5.4: Graphical view of the thickness as function of the deposition time. Data obtained by ellipsometry modelling.

5.1.4. Oxygen Content Determination by XPS, FTIR, EDX and Weighing Methodology

The sections below contain the different measurement techniques that revealed information about the thickness of the silicon oxide layers, and are discussed in order of reliability (starting with the most reliable technique).

Oxygen Content Determination by XPS

The oxygen content in the samples that were deposited at a N_2O/SiH_4 ratio of 0.58 was determined by XPS for both 90 min and 120 min deposition times. The corresponding XPS spectra are shown in figure 5.5 and 5.6. The oxygen content at the surface of the SiO_x layer is calculated to be 57.3% for the sample deposited in 90 min. The oxygen content of the SiO_x layer which was deposited in 120 min was calculated to be 56.5%. So, as expected the deposition time did not change the oxygen content in the samples. Unfortunately it was not possible to also perform measurements on the SiO_x layers deposited at different ratios, so it is not possible to show the effect of N_2O/SiH_4 ratio on the oxygen content by means of XPS.

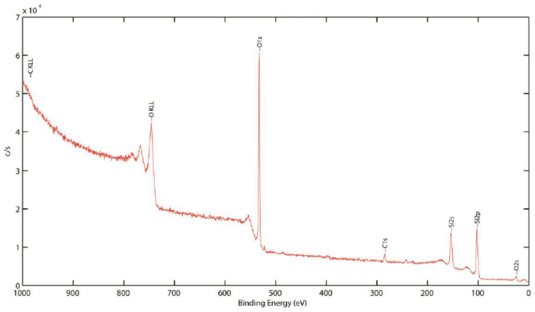

Figure 5.5: XPS spectrum of SiO_x layer deposited in 90 min using a gas flow ratio of 0.58.

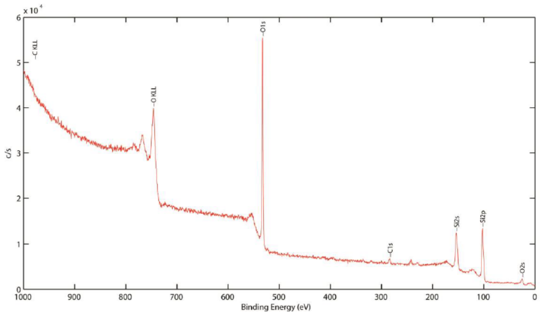

Figure 5.6: XPS spectrum of SiO_x layer deposited in 120 min using a gas flow ratio of 0.58.

Oxygen Content Determination by FTIR

In figures 5.7 and figure 5.8 the FTIR spectra of symmetrical samples with SiO_x layers deposited by varying flow ratios in 90 min and 120 min respectively . All samples show the characteristic Si-O transverse optic stretching vibration peak at wavenumber 1056 cm^{-1} and Si-O bending modes at wavenumber 800 cm^{-1} [58]. Furthermore, a peak is formed around 880 cm^{-1} that can be attributed to Si_2O_3 [59]. The absorbance peaks of Si-O around 1056 cm^{-1} increase for longer deposition times and decreases when the gas flow ratio is increased. Also, the peak intensities at wavenumber of 800 cm^{-1} and 880 cm^{-1} slightly decrease when gas flow ratios are increased. The last noteworthy observation to mention is the different shape of absorbance peak of the 0.33 samples compared to other gas flow ratios. A small peak shift of the Si-O stretching bond towards higher wavenumbers is observed. This shift is attributed to the increased thickness. In the appendix, an FTIR figure is attached which confirms that no difference in shoulder is present between the samples.

Oxygen Content Determination by EDX

In figure 5.9 and 5.10 the elemental distribution in the in-situ oxidation samples is shown. The oxygen weight percentage in the sample with smallest N_2O/SiH_4 ratio is 9.8%, whereas the oxygen weight percentage in the sample with largest N_2O/SiH_4 ratio is 4.6%. It should be noted that the elemental distribution has only be measured at one spot, and thus might be slightly different at another spot. Besides the characteristic Si and O peaks at, a small peak at 0 eV is present, which may be attributed to the noise of the electronics of the detector.

Oxygen Content Determination by Weighing Method

The oxide fraction in the SiO_x layers obtained by the weighing method, is shown in table 5.1 for different N_2O/SiH_4 ratios. The percentage of oxygen within the sample varied between 34% and 43%. From this table, two trends are clear. First, it is shown that the oxygen content seems hardly affected with increasing N_2O/SiH_4 ratio for the same deposition time. Th oxygen content in the samples where the

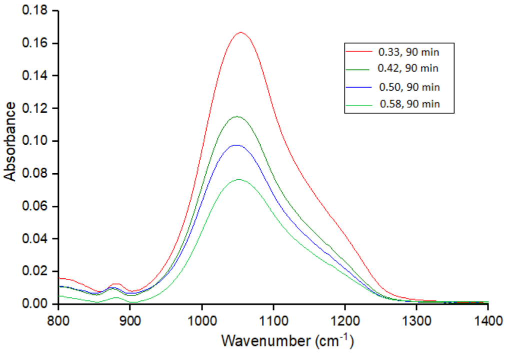

Figure 5.7: FTIR spectrum of as-deposited SiO$_x$ layers, by varying flow ratios and constant deposition time of 90 min.

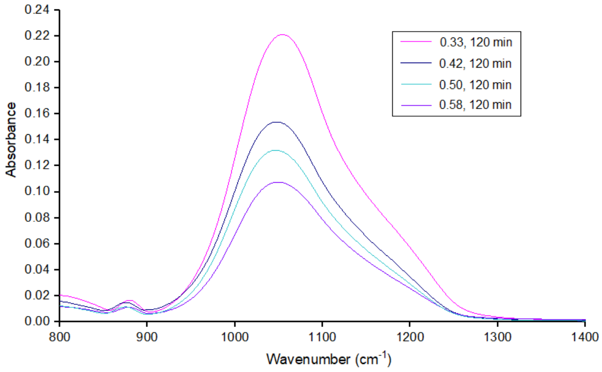

Figure 5.8: FTIR spectrum of as-deposited SiO$_x$ layers, by varying flow ratios and constant deposition time of 120 min.

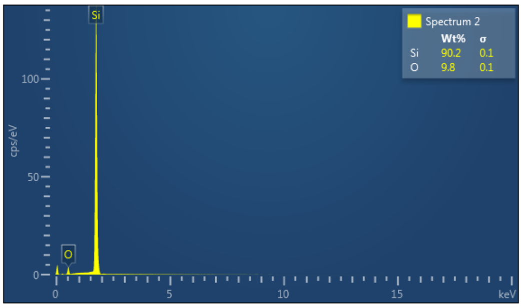

Figure 5.9: EDX spectrum showing elemental composition of sample with SiO$_x$ layer deposited in 120 min by 0.33 flow ratio.

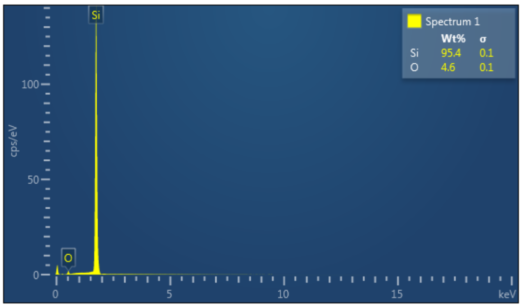

Figure 5.10: EDX spectrum showing elemental composition of sample with SiO$_x$ layer deposited in 120 min by 0.58 flow ratio.

SiO$_x$ layer was deposited in 90 min, was 42% for all N_2O/SiH_4 ratios, except for a gas flow of 0.50 for which the oxygen content was 34%. Second, for constant gas flow ratios and increasing deposition times (90 min to 120 min) the oxygen content increases.

This experiment also showed, with some uncertainty, that the oxygen content in the SiO$_x$ layers obtained by the 0.50 gas flow ratio was varying between 33% and 39% for respectively 90 min and 120 min deposition times. The oxygen content in the SiO$_x$ layers obtained by the other three gas flow ratios showed more constant oxygen content varying between 42% and 45%.

Table 5.1: Oxygen content in the SiO$_x$ layers determined by the weighing methodology.

N_2O/SiH_4	Deposition time (min)	Stoichiometry	Oxygen fraction(%)
0.33	90	SiO$_{0.72}$	42
0.33	120	SiO$_{0.81}$	45
0.42	90	SiO$_{0.71}$	42
0.42	120	SiO$_{0.80}$	44
0.50	90	SiO$_{0.52}$	34
0.50	120	SiO$_{0.65}$	39
0.58	90	SiO$_{0.71}$	42
0.58	120	SiO$_{0.76}$	43

5.1.5. Morphology and Crystallinity by XRD and SEM

X-ray Diffraction

The X-ray Diffraction pattern of a SiO_x layer deposited in 30 min by a gas flow ratio of 0.42 is shown in figure 5.11. In the appendix the datasheets are added to provide information about the silicon and silicon oxide patterns for each technique. The black pattern is corresponding to the X-ray response of the analysed sample. The red and blue sticks indicate, respectively, the characteristic peak positions of poly-Si and silicon oxide. The relatively large and wide black peaks in the left image are due to the (400) oriented substrate reflections. In the right image the background was subtracted and showed that mainly poly-Si was present with orientation. The cubic structure of SiO is less symmetric than of Si and some extra small peaks might be present ($2\theta = 32.8°$, $2\theta = 58.6°$, $2\theta = 78.4°$) but were not found. The grain size of silicon in the silicon oxide was tried to be found. By applying Scherrer's equation, infinitely large grain size was found. The grain size in poly-SiO_x is not expected to be "infinitely" large. The contribution of the monocrystalline wafer is dominating the contribution of the silicon oxide layer.

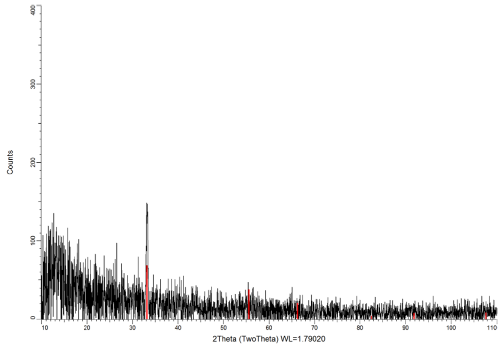

Figure 5.11: Parallel beam XRD spectrum of SiO_x layer deposited in 30 min by gas flow ratio of 0.42.

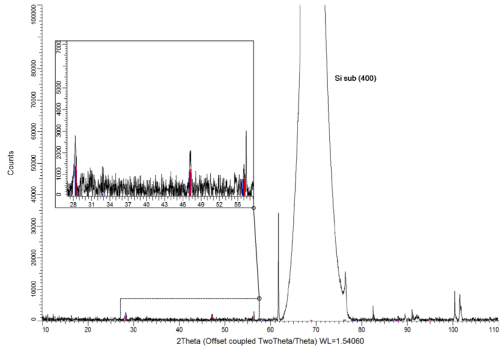

Figure 5.12: Conventional XRD spectrum of SiO_x layer deposited in 30 min by gas flow ratio of 0.42.

SEM

In figures 5.13 and 5.14 SEM top view images are shown of respectively the 0.33 and 0.58 flow ratios. In both figures crystalline phases and amorphous phases can be distinguished, the amorphous parts are indicated by red arrows for clearance. The grains in the SiO_x layer deposited by the lowest N_2O/SiH_4 flow ratio are larger than those in the layer deposited by the largest N_2O/SiH_4 flow ratio. Also, the SiO_x layer obtained by using the lowest N_2O/SiH_4 flow ratio shows a lower fraction of amorphous regions when compared to the SiO_x layer obtained by using the largest N_2O/SiH_4, because no dark spots are visible.

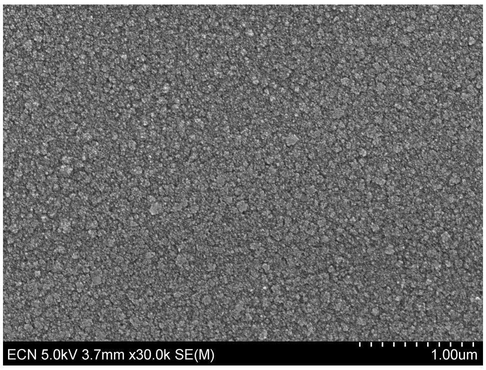

Figure 5.13: SEM top view of SiO_x layer developed after 120 min deposition of 0.33 N_2O/SiH_4.

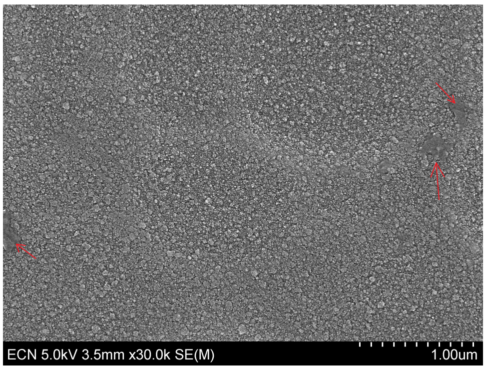

Figure 5.14: SEM top view of SiO_x layer developed after 120 min deposition of 0.58 N_2O/SiH_4.

5.2. Optical Constants Determination by SE

The ellipsometry modelling also determined the optical constants *n* and *k* of the SiO$_x$ layer. The modelling was done for all different ratios and resulted in similar ranges of values for the refractive index and extinction coefficient. In figure 5.15 the refractive indices and extinction coefficients of all different ratios are shown. The values are given for the visible solar spectrum and a part of the infrared spectrum (400 nm to 700 nm and 700 nm to 1000 nm). The refractive index was shown, with a mean square error of 10-20, to be in the range of the refractive index of Si_3N_4 [21]. With respect to application as anti-reflective coating, this is a promising result. The ellipsometry data suggests that the samples with lower gas flow ratio are less oxygen rich and have higher n and k, than the samples with higher gas flow ratio. This is expected, however, it is in contradiction with the results on the oxygen content.

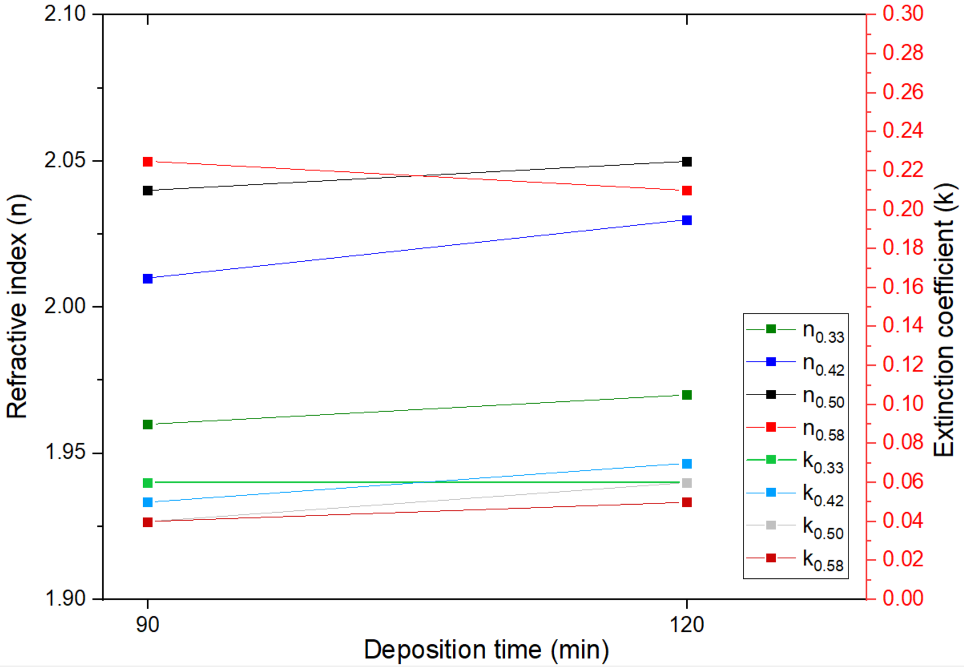

Figure 5.15: Refractive index and extinction coefficient values taken at 1000 nm.

5.3. Discussion

The post-doped SiO_x layers developed by means of in-situ LPCVD growth, were characterized in terms of minority carrier lifetime, doping profile, thickness, oxygen content and refractive index. To explain the observed behaviour of the silicon oxide layers, the information of the characterization measurements will be combined. First the thickness and oxygen content will be discussed, which will be linked to the minority carrier lifetime and doping profile.

The thickness was estimated by ellipsometry modelling. It was obtained that the thickness increased with the deposition time, but decreased with gas flow ratio. The SEM cross-section confirmed similar thickness values, as obtained by the model, for the SiO_x layer deposited in 90 min using a gas flow ratio of 0.58. Both thickness estimations were in the order of 50 nm. As similar oxide layers obtained, it may be assumed that the model is also valid, with some error, for the other silicon oxide layers. A higher fraction of N_2O inhibits the deposition which is also found by Hitchman [60]. The N_2O is adsorbed at the surface and acts as blocking sites for the poly-Si growth. Da Silva et al. also found that the growth rate increases with increase in gas flow ratio [38].

It was expected that higher N_2O fraction results in higher oxygen content. The EDX measurement indicated that higher oxygen content was measured in SiO_x layers obtained by low N_2O fraction compared to SiO_x layers obtained by high N_2O fraction. This is attributed to an increased oxide thickness and not to an increase in oxygen fraction, since growth rate is increased with lower gas flow ratio. This is in agreement with the observations of FTIR, where a change in gas flow ratio did not result in a change of the Si-O vibration.

For both deposition times it was observed that the minority carrier lifetime in the post-doped samples increases with increasing N_2O/SiH_4 ratios (before hydrogenation and firing). The increase of gas flow ratio results in thinner silicon oxide layers with smaller grain size. This combination of properties is beneficial for the minority carrier lifetime. The smaller grain size is beneficial because this will ease phosphorus doping compared to the samples with larger grain sizes, because the phosphorus diffusion coefficient along grain boundaries in silicon is 8000 times larger than the bulk diffusion coefficient [61]. A higher doping level in silicon oxide enhances the minority carrier transport and thus increases minority carrier lifetime. Also, SEM revealed that larger amorphous fraction is present in the samples deposited by exposure to the largest gas flow ratio. The amorphous fraction is not desired since this is known to decrease the conductivity and should be reduced [11].

Hydrogenation enhances the minority carrier lifetime in all samples because of the earlier discussed hydrogen passivation at interface of SiO_x and the silicon wafer. The positive hydrogenation effect becomes more pronounced in the 120 min upon an increase in gas flow ratio. It is suggested that in thinner and more amorphous SiO_x layers, hydrogen can diffuse more easily from SiN:H through the SiO_x layer and gets trapped at the dangling bonds at the interface of the silicon oxide and silicon wafer. During firing, the hydrogen which still is in the SiN:H layer, gets released and diffuses to the $SiO_x|Si$ interface. As the firing effect is so extreme, it is suggested that not only hydrogen passivation at the interface, but also hydrogenation in bulk is contributing to the increase in minority carrier lifetime (reducing SRH).

The phosphorus concentration profile of the SiO_x layer deposited in 30 min with gas ratio of 0.33 showed a curve similar to that of poly-Si [62]. It is suggested that first poly-Si is grown, before oxidation can take place. The deposition time of 30 min is too short to oxidise the poly-Si completely and thus some poly-Si is remained. Complete in-diffusion is observed, which is explained by a combination of high temperature during the doping process and relatively thin layer. This greatly enhances the diffusion of phosphorus to the silicon wafer. It is also suggested that longer deposition times are required in order to activate the oxidation by N_2O. Most surprisingly, the SiO_x layers deposited in 120 min with a gas flow ratio of 0.33 and 0.42 show some sort of kink- and tail profile. This indicates that the phosphorus can diffuse through the silicon oxide into the wafer, probably by the interstitial (kick-out) mechanism, as it is located at electrical active sites.

This is in agreement with doping profiles in the samples deposited in 90 min and 120 min, where no plateau region and in-diffusion is observed. There are two suggestions for the fact that no in-diffusion has taken place in these samples. One suggestion is that phosphorus is only present in the silicon oxide layer and the second suggestion is that phosphorus did not enter the silicon oxide. However, since the phosphorus diffuses into the silicon wafer in the 30 min sample, it is suggested that the second suggestion is less probable.

The oxygen content determined by the weighing method does not show similar trends as was observed by EDX and FTIR measurements. It was expected that the oxygen content does not change with deposition time, but with gas flow ratio. However, the oxygen fraction in the SiO_x layers is, according to the weighing method calculation, increased when longer deposition times are applied and remained more or less constant with increase in gas flow ratio. It is suggested that the SiN_x capping layer is not protecting the silicon wafer from oxidation. Therefore, also oxygen in the silicon wafer is contributing to the calculated oxygen fraction. The oxygen fractions are similar for all different ratios and only a function of deposition time.

It is expected that an increase in deposition time does not effect the composition in the SiO_x. The FTIR spectra of SiO_x layers deposited in 120 min showed higher absorbance peaks than the FTIR spectra of SiO_x layers deposited in 90 min, indicating a larger amount of Si-O bonds. However, the shape of the FTIR spectra did not change with deposition time, which indicates that the oxygen content is the same for both deposition times. Furthermore, it is expected that upon increasing the N_2O flow, the oxygen content increases accordingly. However, no real change in shape of FTIR spectra is observed for SiO_x layers obtained with different gas flow ratio. If the gas flow N_2O/SiH_4 is increased, the Si-O stretch vibration peak is decreased due to decreased thickness.

5.4. Conclusion

The research question which can be answered after this experiment is: *Is post-doping of in situ oxidised* SiO_x *layers a successful method to produce doped* SiO_x *layers?* The conclusions which can be drawn from this experiment are the following:

- Promising minority carrier lifetimes are observed in the SiO_x layers obtained by largest N_2O/SiH_4 ratio and shortest deposition time (>4 ms after firing).
- Hydrogenation enhances the passivation quality in all SiO_x layers.
- Firing enhances the passivation quality in all SiO_x layers and had greatest effect on the SiO_x layers obtained by largest N_2O/SiH_4.
- Substoichiometric SiO_x layers were formed by in-situ oxidation.
- The refractive index of the SiO_x varied between 1.96-2.51, which makes the layer a promising candidate as passivating contact layer with extra anti-reflection function.

The SiO_x layers deposited in 90 min by gas flow ratio of 0.58 in this experiment seems the most promising for application in passivating contacts.

6

Conclusion and Future Recommendations

Based on the outcomes of the previous chapters, a complete conclusion on the research will be drawn in this chapter followed by an outlook of future work.

6.1. Conclusion

In this work, two different routes to fabricate doped silicon oxide layers were investigated. Throughout this exploratory research, material properties of SiO_x layers were linked to its passivation behaviour and a lot of insight was gained into which techniques are suitable to characterize SiO_x layers.

The most promising post-oxidation route is based on wet oxidation. Excellent minority carrier lifetimes (>10 ms, after firing) were obtained in wet oxidised 65 nm poly-Si samples. Sheet resistance measurements showed that phosphorus is most likely electrically active in the silicon oxide layer. Also, in-diffusion was kept to a minimum. The silicon oxide layers were furthermore proven to be firing stable in terms of minority carrier lifetime. The hydrogen passivation was most likely enhanced because of the SiO_2 capping layer effect. These are promising results in terms of selectivity and passivation. Dry oxidation of the post-oxidation at 900 °C did not result in a promising substitute for current existing passivation layers. Phosphorus atoms were not incorporated in the silicon oxide layer, but mainly in-diffused to the silicon wafer leading to Auger recombination.

The passivation quality of the post-doped silicon oxide layers was shown to be good enough for future applicability as passivating contact layer (>4 ms after firing). The increase in gas flow ratio results in SiO_x layers with comparable oxygen content, but with different thicknesses. Firing of the hydrogenated post-doped silicon oxide layers significantly improved the minority carrier lifetime. SiO_x layers which are fabricated by using a gas flow ratio of 0.58 showed the best results in terms of minority carrier lifetime.

It is important to conduct more research on this topic, towards the successful realisation of silicon oxide as a passivating contact layer. This study gave insight as to why, or why not, a certain route is successful to form doped silicon oxide layers for passivating contact layers.

6.2. Future Recommendations

Throughout this thesis work a continuous stream of information was gathered and analysed to understand the behaviour of the silicon oxide layers. The future recommendations for this research consists of a general outlook that applies for each investigated route and of an outlook specifically for the post-oxidation and the post-doped routes. Doors might be opened to more follow-up research on this topic.

The doping level in the silicon oxide layer remained unknown, due to lack of suitable analysis techniques to study phosphorus doping in silicon oxide. Since it is crucial to determine the amount of electrically active phosphorus in the silicon oxide layer, it is necessary to find a way to determine active phosphorus concentration in the SiO_x layer. Secondary Ion Mass Spectroscopy can reveal information about any type of phosphorus present in the SiO_x, but cannot distinguish between electrically active and inactive phosphorus. High Resolution Transmission Electron Microscopy and Scanning-Transmission Electron Microscopy are more expensive analysis techniques, but will very accurately determine the elemental mappings of specific elements, for example phosphorus. The latter two mentioned techniques are not only useful in terms of quantification of elements, but will also indicate the location of specific elements, e.g. segregated at grain boundaries or within the grain. Since the electrolyte in ECV measurements (NH4F-HF) is not able to etch silicon oxide, another suggestion is to find an electrolyte which is able to etch the silicon oxide uniformly and create a Schottky barrier with the silicon oxide. XPS measurements can also be useful in the determination of presence of electrically active phosphorus. The P 2p signal in the XPS spectrum might be detectable when dwell times are signifcantly increased (should be about 70 times higher than dwell times for C 1s and O 1s) [57].

Another requirement for further investigation is to determine if it is possible to fire through silicon oxide and make it contactable. This is of great importance before solar cell devices can be made. In the most favourable situation there is low contact resistivity between the metal contact and the passivating contact. This might be possible by depositing a layer of silicon oxide which is terminated below the metal layer and locally replaced with a more conductive material (such as poly-Si).

Next, lateral conductivity needs to be improved after which it becomes possible to replace the currently used poly-Si with SiO_x in the PERC solar cell configuration. This might be possible by annealing the post-doped samples. Hereby the fraction of amorphous phase might be crystallised, so that the crystalline fraction in the sample increases. Crystallised silicon oxides will result in more conductive SiO_x layers [11].

Since hydrogenation and firing are increasing the minority carrier lifetime in wet oxidised and post-doped silicon oxide layers so significantly, it becomes interesting to study in further detail which mechanism affects this. It is suggested to investigate the hydrogen diffusion profile by STEM. STEM measurements may show where the hydrogen has diffused to after hydrogenation and firing. Also, it is interesting to analyse a wet oxidised 65 nm sample after firing with FTIR to verify if the characteristic Si-H absorbance peak is increased. It is expected that this peak becomes more pronounced due to enhanced dangling bond passivation. This will confirm the made suggestion that firing improves the minority carrier lifetime due to increased hydrogen surface passivation.

Due to the lack of quartz substrates, optical constants (n,k) of the developed SiO_x layers were estimated by ellipsometry modelling. However, it should be emphasized that the optical properties of SiO_x layers can be more easily and accurately determined when quartz wafers are used as substrate. By using quartz glass it becomes possible to do transmission-reflection measurements which will reveal both information about the optical constants and the transparency of the silicon oxides. Unfortunately, due to wafer availability in the laboratory and lack of time it was not yet possible to do these measurements.

The oxygen content was determined by different methods but not even one was shown to give conclusive results. Therefore the measurements need to be improved, or different measurement techniques need to be applied. In order to improve reliability of the weighing methodology, it needs to be investigated if a proper SiN_x (i.e. Si_3N_4) capping layer has been produced which prevents oxidation of the wafer. If Si_3N_4 has been deposited the wafer will be protected and oxygen determination is reliable. Another way to determine the oxide content is to perform Rutherford Backscattering Spectrometry measurements. In previous studies this technique has successfully determined the oxide fraction in SiO_x layers.

To summarize, a fundamental basis has been formed for further development of SiO_x layers as passivating contact layers. The results are definitely useful, however it is not a conclusive research. It is important to conduct more research on the SiO_x layers, especially in terms of doping efficiency and lateral conductivity. When this is better understood, the next step is to investigate the applicability of doped SiO_x layers in a device test structure.

Acknowledgements

I would like to thank three important groups of people, without whom it would not have been possible to complete this master thesis with success: my thesis supervisors, specific members of the solar cell department and my family.

First of all I would like to thanks Paula Bronsveld for providing the opportunity to perform my master thesis at ECN, it was a great adventure and pleasure. Furthermore, I am very grateful for the fact that you were my daily supervisor. Without your experience and knowledge I would not have been able to make such a progress within this research. Also, I appreciate the trust you gave me to work so independently.

Many thanks to Amarante Böttger, my TU Delft supervisor, who always showed interest in my proceedings and helped me to think in the right direction. Thank you for being supportive in the ideas I came up with, but also for being critical. This kept me sharp and helped me to develop my ideas further.

Special thanks to John Anker who showed so much assistance and patience in the laboratory. Also, I would like to thank Martijn Lenes who modified the LPCVD tool in such a way that I could run my process. To both of you, also thanks for your shared thoughts and insights on this project. Furthermore, I would like to thank Pi Danzl for assisting me during the Spectroscopic Ellipsometer measurements and doing the Terrahertz measurements.

Upon reading other acknowledgements I always feel a little bit melodramatic when writers start to thank their family. But actually they are always right. Dear mom, dad and Go, without your support I would not have been able to stand where I stand today. Although your main interests lay in a different field (Law), you showed tremendous amount of sympathy and concern in my developments towards an engineer. A huge thanks to you!

Kinge, I (sometimes) might have been unreachable and not able to talk about many other things than my graduation project, but I cannot thank you enough for your unconditional support. You were able to turn every negative aspect into something positive again!

And finally, last but by no means least, thanks to everyone who I forgot to mention. If you feel addressed, you might be right and I would like to thank you for your help and insights as well!

Appendix

Cauchy model

For spectroscopic ellipsometry modelling, a Cauchy model is applied, since this model works best for materials that have no or weak optical absorption of the visible spectrum. The refractive index is decreasing with increasing wavelength. The refractive index (n) and extinction coefficient are calculated as follows:

$$\boxed{\begin{aligned} n(\lambda) &= A + \frac{10^4 \times B}{\lambda^2} + \frac{10^9 \times C}{\lambda^4} \\ k(\lambda) &= 10^{-}5 \times D + \frac{10^4 \times E}{\lambda^2} + \frac{10^4 \times F}{\lambda^4} \end{aligned}} \tag{1}$$

where:

- A is a dimensionless parameter.
- B (nm^2) is a parameter that affects the curvature and the amplitude of the refractive index in the visible spectrum.
- C (nm^4) is a parameter affecting the curvature and amplitude in the UV spectrum.
- D is dimensionless parameter, similar to A.
- E (nm^2) is a parameter that affects the curvature and the amplitude of the refractive index in the visible spectrum.
- F (nm^4) is a parameter affecting the curvature and amplitude in the UV spectrum.

Appendix

Weighing methodology

In the equation below the derivation of the oxygen content calculation is shown.

$$\boxed{\begin{aligned} m_{\mathrm{SiO_2}} &= m_3 - m_1 \\ &= (28 + 32) \times n \\ &= 60n \\ n &= \frac{m_3 - m_1}{60} \end{aligned}}$$

$$\boxed{\begin{aligned} & m_{SiO_{\mathrm{x}}} \\ &\qquad = m_2 - m_1 \\ &\qquad = (28 + 16x) \times n \\ &\qquad = (28 + 16x) \times \frac{m_3 - m_1}{60} \end{aligned}}$$

$$\boxed{\begin{aligned} 16x &= 60 \times \frac{m_2 - m_1}{m_3 - m_1 - 28} \\ x &= \frac{60}{16} \times \frac{m_2 - m_1}{m_3 - m_1} - \frac{28}{16} \end{aligned}} \tag{2}$$

in which: $m_{\mathrm{SiO_2}}$ is the mass of the SiO_2 layer, m_3 is the mass of the wafer after complete oxidation, m_1 is the mass of the wafer with SiNx. This will give the number of moles in the SiO_2 as a function of the mass of the wafer after complete oxidation and the mass of the wafer with SiNx.

Appendix

Photoluminescence

As the SiO_x layers were deposited after manual modification of the LPCVD tool manually, it was required to determine whether the SiO_x layers were deposited homogeneously on the substrate. PL imaging indeed showed that the deposition of SiO_x was not homogeneously distributed. A photoluminescence measurement was done on an as-deposited symmetrical sample with SiO_x layer deposited in 90 min using a gas flow ratio of 0.5. As can be seen in the figure below, the lower left corner is showing higher conductivity which may be caused by larger phosphorus concentration, or lower oxygen content.

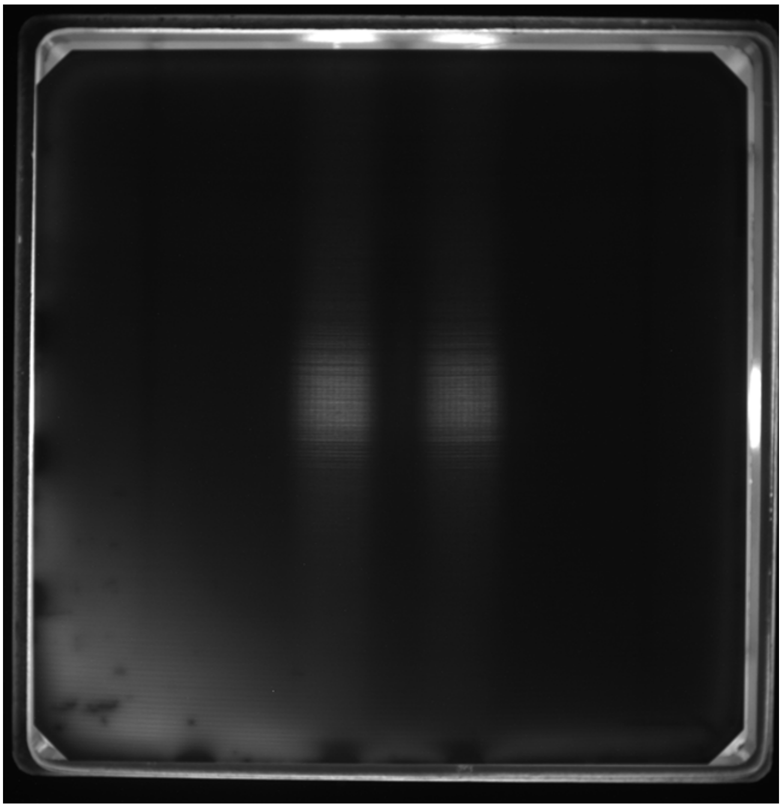

Appendix

Terahertz (THz) Sheet resistance measurements were in principle done by the Sherescan apparatus, but due to high contact resistance this technique was not suitable to obtain sheet resistance values. Terahertz measurements are able to measure the resistance without making contact with the silicon oxide layer, however the sheet resistance value of at least one point needs to be known. Unfortunately not even one reliable measurement point was obtained from the sherescan. So, the measurement done with Terahertz only reveals information about the homogeneity of the sample. The inhomogeneity observed in the image below is caused by thickness variations of the SiN:H deposition. Due to a processing error, the SiN:H was not homogeneously deposited on the sample. However, it is noteworthy that the SiN:H affected the response to the Terahertz.

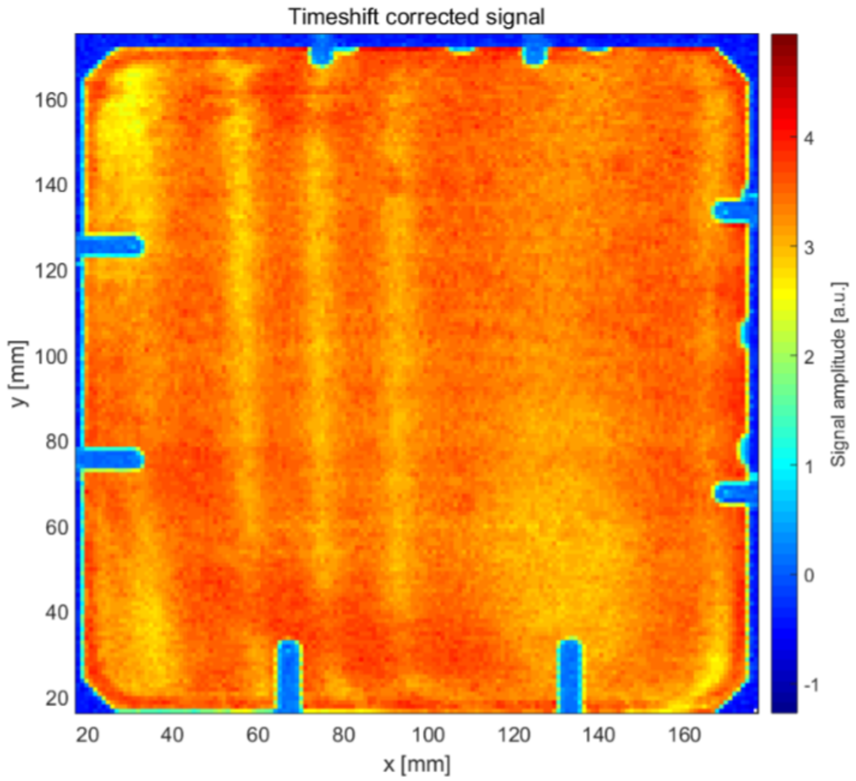

Appendix

FTIR post-doped 90 min

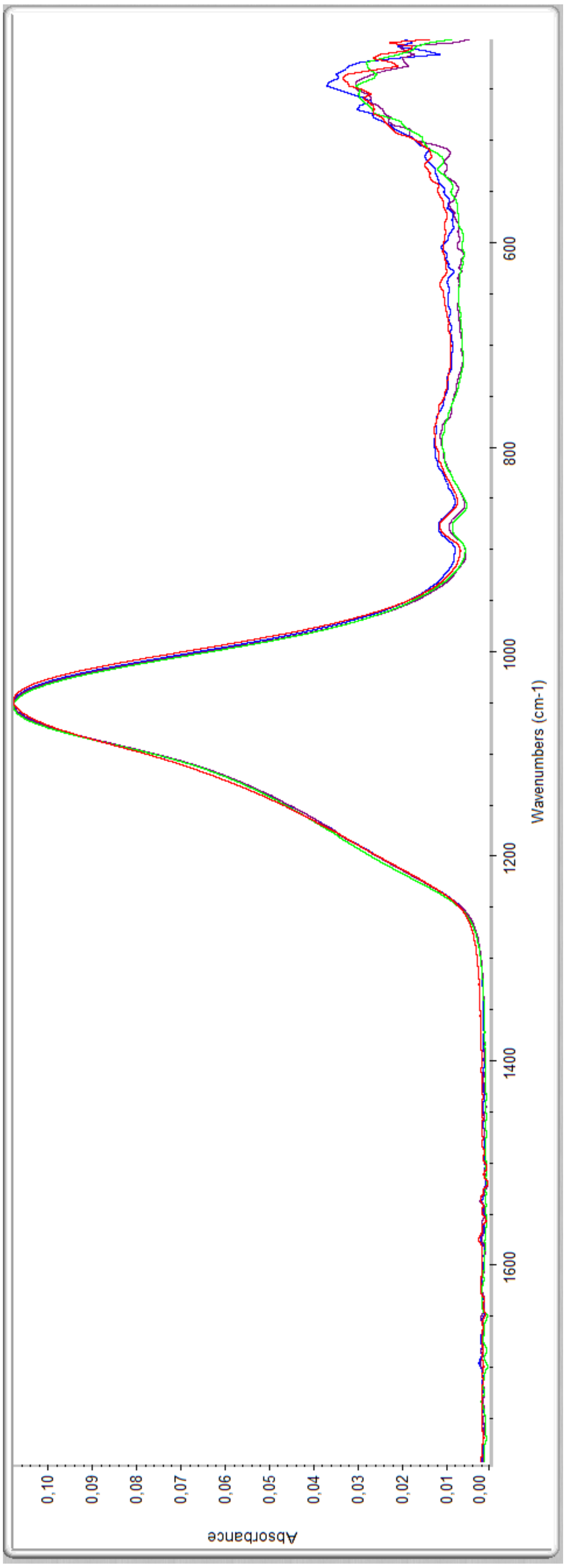
Absorbance
0,10
0,09
0,08
0,07
0,06
0,05
0,04
0,03
0,02
0,01
0,00
Wavenumbers (cm-1)
1600
1400
1200
1000
800
600

Appendix

QSSPC datasheet

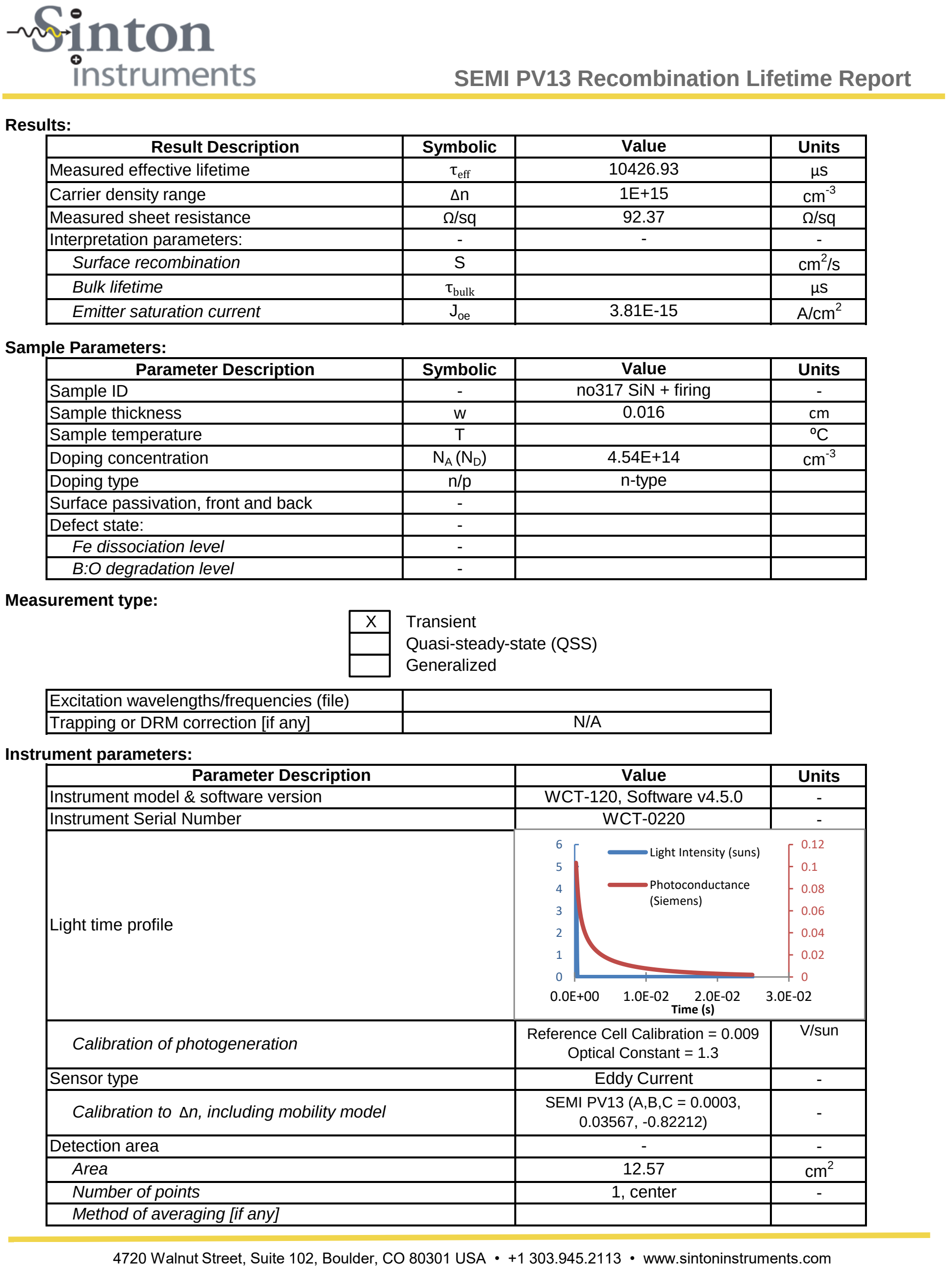

SEMI PV13 Recombination Lifetime Report

Results:

Result Description	Symbolic	Value	Units
Measured effective lifetime	τ_{eff}	10426.93	µs
Carrier density range	Δn	1E+15	cm^{-3}
Measured sheet resistance	Ω/sq	92.37	Ω/sq
Interpretation parameters:	-	-	-
Surface recombination	S		cm^2/s
Bulk lifetime	τ_{bulk}		µs
Emitter saturation current	J_{oe}	3.81E-15	A/cm^2

Sample Parameters:

Parameter Description	Symbolic	Value	Units
Sample ID	-	no317 SiN + firing	-
Sample thickness	w	0.016	cm
Sample temperature	T		ºC
Doping concentration	N_A (N_D)	4.54E+14	cm^{-3}
Doping type	n/p	n-type	
Surface passivation, front and back	-		
Defect state:	-		
Fe dissociation level	-		
B:O degradation level	-		

Measurement type:

☒ Transient
☐ Quasi-steady-state (QSS)
☐ Generalized

Excitation wavelengths/frequencies (file)	
Trapping or DRM correction [if any]	N/A

Instrument parameters:

Parameter Description	Value	Units
Instrument model & software version	WCT-120, Software v4.5.0	-
Instrument Serial Number	WCT-0220	-
Light time profile		
Calibration of photogeneration	Reference Cell Calibration = 0.009 Optical Constant = 1.3	V/sun
Sensor type	Eddy Current	-
Calibration to Δn*, including mobility model*	SEMI PV13 (A,B,C = 0.0003, 0.03567, -0.82212)	-
Detection area	-	-
Area	12.57	cm^2
Number of points	1, center	-
Method of averaging [if any]		

4720 Walnut Street, Suite 102, Boulder, CO 80301 USA • +1 303.945.2113 • www.sintoninstruments.com

Appendix

X-Ray Diffraction (XRD)

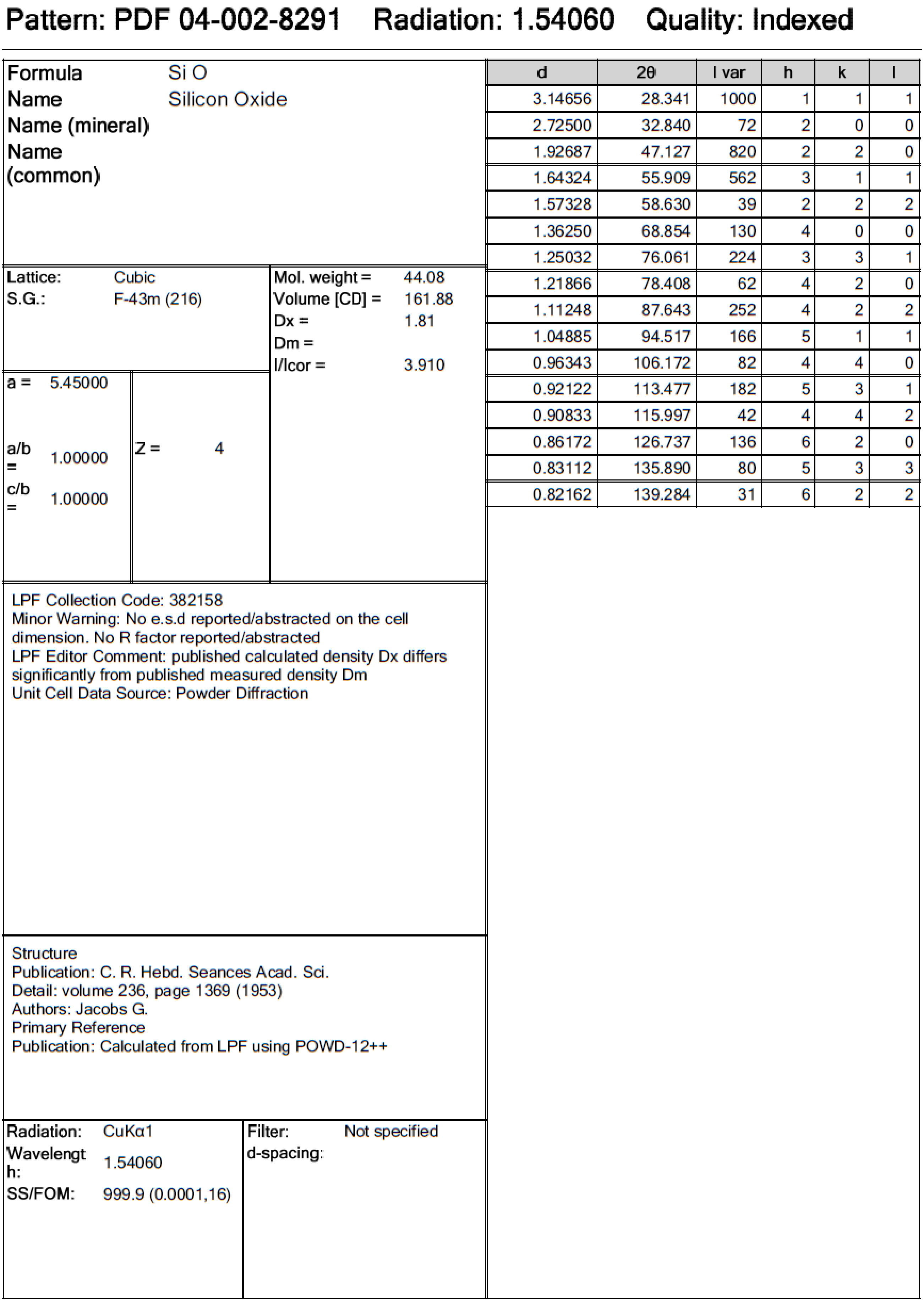

Pattern: PDF 04-002-8291 Radiation: 1.54060 Quality: Indexed

Formula Si O
Name Silicon Oxide
Name (mineral)
Name (common)

Lattice: Cubic
S.G.: F-43m (216)

Mol. weight = 44.08
Volume [CD] = 161.88
Dx = 1.81
Dm =
I/Icor = 3.910

a = 5.45000
a/b = 1.00000
c/b = 1.00000

Z = 4

d	2θ	I var	h	k	l
3.14656	28.341	1000	1	1	1
2.72500	32.840	72	2	0	0
1.92687	47.127	820	2	2	0
1.64324	55.909	562	3	1	1
1.57328	58.630	39	2	2	2
1.36250	68.854	130	4	0	0
1.25032	76.061	224	3	3	1
1.21866	78.408	62	4	2	0
1.11248	87.643	252	4	2	2
1.04885	94.517	166	5	1	1
0.96343	106.172	82	4	4	0
0.92122	113.477	182	5	3	1
0.90833	115.997	42	4	4	2
0.86172	126.737	136	6	2	0
0.83112	135.890	80	5	3	3
0.82162	139.284	31	6	2	2

LPF Collection Code: 382158
Minor Warning: No e.s.d reported/abstracted on the cell dimension. No R factor reported/abstracted
LPF Editor Comment: published calculated density Dx differs significantly from published measured density Dm
Unit Cell Data Source: Powder Diffraction

Structure
Publication: C. R. Hebd. Seances Acad. Sci.
Detail: volume 236, page 1369 (1953)
Authors: Jacobs G.
Primary Reference
Publication: Calculated from LPF using POWD-12++

Radiation: CuKα1
Wavelength: 1.54060
SS/FOM: 999.9 (0.0001,16)

Filter: Not specified
d-spacing:

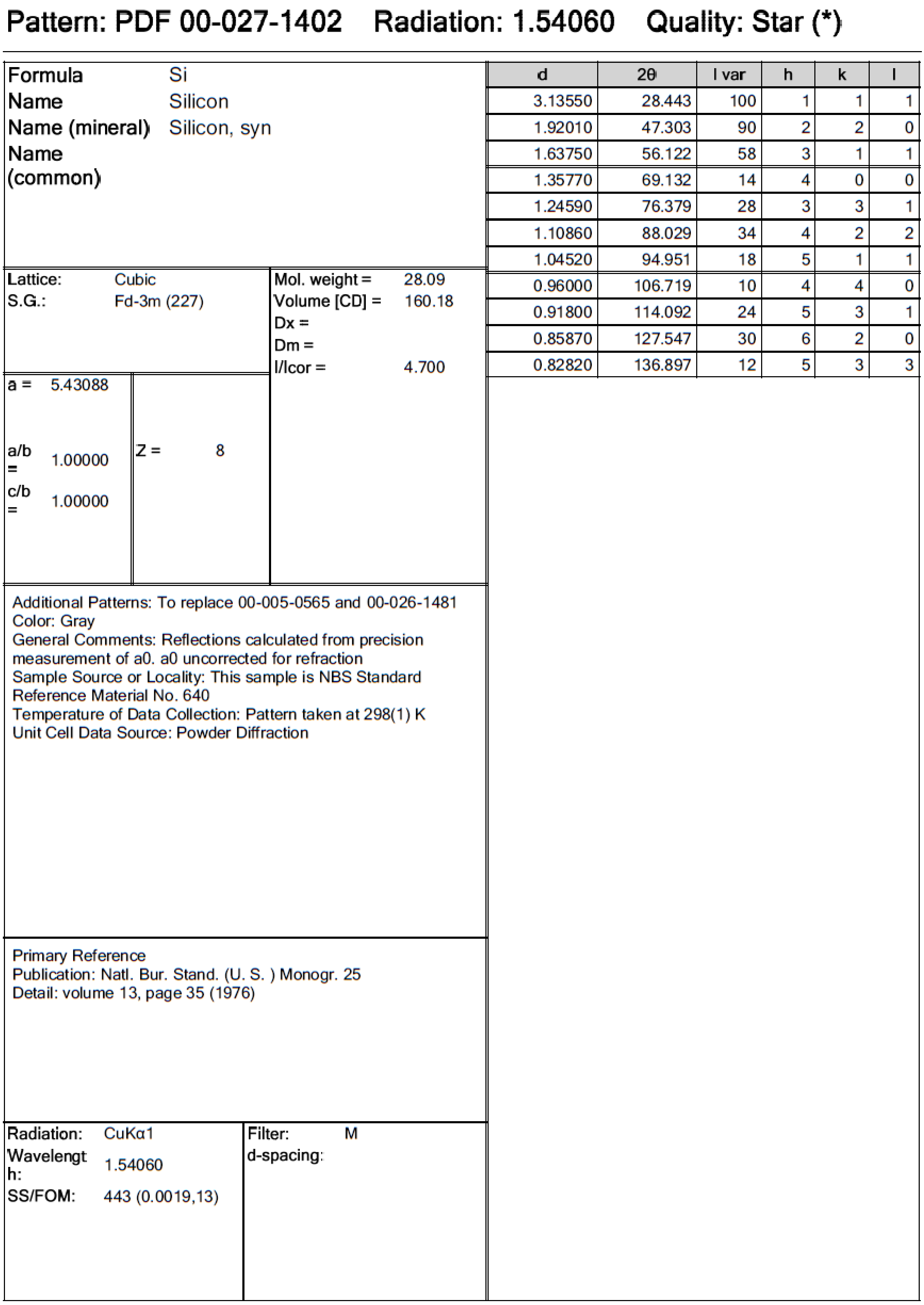

Pattern: PDF 00-027-1402 Radiation: 1.54060 Quality: Star (*)

Formula: Si
Name: Silicon
Name (mineral): Silicon, syn
Name (common):

Lattice: Cubic
S.G.: Fd-3m (227)

Mol. weight = 28.09
Volume [CD] = 160.18
Dx =
Dm =
I/Icor = 4.700

a = 5.43088
a/b = 1.00000
c/b = 1.00000
Z = 8

d	2θ	I var	h	k	l
3.13550	28.443	100	1	1	1
1.92010	47.303	90	2	2	0
1.63750	56.122	58	3	1	1
1.35770	69.132	14	4	0	0
1.24590	76.379	28	3	3	1
1.10860	88.029	34	4	2	2
1.04520	94.951	18	5	1	1
0.96000	106.719	10	4	4	0
0.91800	114.092	24	5	3	1
0.85870	127.547	30	6	2	0
0.82820	136.897	12	5	3	3

Additional Patterns: To replace 00-005-0565 and 00-026-1481
Color: Gray
General Comments: Reflections calculated from precision measurement of a0. a0 uncorrected for refraction
Sample Source or Locality: This sample is NBS Standard Reference Material No. 640
Temperature of Data Collection: Pattern taken at 298(1) K
Unit Cell Data Source: Powder Diffraction

Primary Reference
Publication: Natl. Bur. Stand. (U. S.) Monogr. 25
Detail: volume 13, page 35 (1976)

Radiation: CuKα1
Wavelength: 1.54060
SS/FOM: 443 (0.0019,13)

Filter: M
d-spacing:

References

[1] "Paris Agreement 2015," https://treaties.un.org/pages/ViewDetails.aspx?src=TREATY&mtdsg_no=XXVII-7-d&chapter=27&clang=_en, accessed: 2018-04-05.

[2] ITRPV, "International technology roadmap for photovoltaic results 2017(ninth edition)," 2018.

[3] K. Masuko, M. Shigematsu, T. Hashiguchi, D. Fujishima, M. Kai, N. Yoshimura, T. Yamaguchi, Y. Ichihashi, T. Mishima, N. Matsubara *et al.*, "Achievement of more than 25% conversion efficiency with crystalline silicon heterojunction solar cell," *IEEE Journal of Photovoltaics*, vol. 4, no. 6, pp. 1433–1435, 2014.

[4] M. Taguchi, A. Yano, S. Tohoda, K. Matsuyama, Y. Nakamura, T. Nishiwaki, K. Fujita, and E. Maruyama, "24.7% record efficiency hit solar cell on thin silicon wafer," *IEEE Journal of Photovoltaics*, vol. 4, no. 1, pp. 96–99, 2014.

[5] S. Pillai, K. Catchpole, T. Trupke, and M. Green, "Surface plasmon enhanced silicon solar cells," *Journal of applied physics*, vol. 101, no. 9, p. 093105, 2007.

[6] A. W. Blakers, A. Wang, A. M. Milne, J. Zhao, and M. A. Green, "22.8% efficient silicon solar cell," *Applied Physics Letters*, vol. 55, no. 13, pp. 1363–1365, 1989.

[7] M. Stodolny, M. Lenes, Y. Wu, G. Janssen, I. Romijn, J. Luchies, and L. Geerligs, "n-type polysilicon passivating contact for industrial bifacial n-type solar cells," *Solar Energy Materials and Solar Cells*, vol. 158, pp. 24–28, 2016.

[8] M. Tanaka, M. Taguchi, T. Matsuyama, T. Sawada, S. Tsuda, S. Nakano, H. Hanafusa, and Y. Kuwano, "Development of new a-si/c-si heterojunction solar cells: Acj-hit (artificially constructed junction-heterojunction with intrinsic thin-layer)," *Japanese Journal of Applied Physics*, vol. 31, no. 11R, p. 3518, 1992.

[9] M. A. Green, Y. Hishikawa, W. Warta, E. D. Dunlop, D. H. Levi, J. Hohl-Ebinger, and A. W. Ho-Baillie, "Solar cell efficiency tables (version 50)," *Progress in Photovoltaics: Research and Applications*, vol. 25, no. 7, pp. 668–676, 2017.

[10] K. Yoshikawa, H. Kawasaki, W. Yoshida, T. Irie, K. Konishi, K. Nakano, T. Uto, D. Adachi, M. Kanematsu, H. Uzu *et al.*, "Silicon heterojunction solar cell with interdigitated back contacts for a photoconversion efficiency over 26%," *Nature Energy*, vol. 2, p. 17032, 2017.

[11] A. Lambertz, "Development of doped microcrystalline silicon oxide and its application to thin-film silicon solar cells," 2015.

[12] I. Mack, J. Stuckelberger, P. Wyss, G. Nogay, Q. Jeangros, J. Horzel, C. Allebé, M. Despeisse, F.-J. Haug, A. Ingenito *et al.*, "Properties of mixed phase silicon-oxide-based passivating contacts for silicon solar cells," *Solar Energy Materials and Solar Cells*, 2018.

[13] C. Shin, S. Iftiquar, J. Park, Y. Kim, S. Kim, J. Jung, and J. Yi, "Development of highly conducting n-type micro-crystalline silicon oxide thin film and its application in high efficiency amorphous silicon solar cell," *Materials Science in Semiconductor Processing*, vol. 66, pp. 223–231, 2017.

[14] J. Geissbühler, J. Werner, S. Martin de Nicolas, L. Barraud, A. Hessler-Wyser, M. Despeisse, S. Nicolay, A. Tomasi, B. Niesen, S. De Wolf *et al.*, "22.5% efficient silicon heterojunction solar cell with molybdenum oxide hole collector," *Applied Physics Letters*, vol. 107, no. 8, p. 081601, 2015.

[15] G. Nogay, J. Stuckelberger, P. Wyss, E. Rucavado, C. Allebe, T. Koida, M. Morales-Masis, M. Despeisse, F.-J. Haug, P. Löper *et al.*, "Interplay of annealing temperature and doping in hole selective rear contacts based on silicon-rich silicon-carbide thin films," *Solar Energy Materials and Solar Cells*, vol. 173, pp. 18–24, 2017.

[16] K. Ding, U. Aeberhard, V. Smirnov, B. Holländer, F. Finger, and U. Rau, "Wide gap microcrystalline silicon oxide emitter for a-siox: H/c-si heterojunction solar cells," *Japanese Journal of Applied Physics*, vol. 52, no. 12R, p. 122304, 2013.

[17] J. Plans, G. Diaz, E. Martinez, and F. Yndurain, "Theoretical study of oxygen in silicon: Breaking of the si—si bond," *Physical Review B*, vol. 35, no. 2, p. 788, 1987.

[18] S. Iftiquar, "The roles of deposition pressure and rf power in opto-electronic properties of a-sio: H films," *Journal of Physics D: Applied Physics*, vol. 31, no. 14, p. 1630, 1998.

[19] W. Bludau, A. Onton, and W. Heinke, "Temperature dependence of the band gap of silicon," *Journal of Applied Physics*, vol. 45, no. 4, pp. 1846–1848, 1974.

[20] M. Houssa, "High k gate dielectrics," 2003.

[21] K. Luke, Y. Okawachi, M. R. Lamont, A. L. Gaeta, and M. Lipson, "Broadband mid-infrared frequency comb generation in a si 3 n 4 microresonator," *Optics letters*, vol. 40, no. 21, pp. 4823–4826, 2015.

[22] "Energy band of silicon," http://optique-ingenieur.org/en/courses/OPI_ang_M05_C02/co/Contenu.html, accessed: 2018-04-16.

[23] A. H. Smets, K. Jäger, O. Isabella, R. A. van Swaaij, and M. Zeman, "Solar energy: The physics and engineering of photovoltaic conversion, technologies and systems," 2016.

[24] E. Becquerel, "On electric effects under the influence of solar radiation," *Compt. rend.*, vol. 9, p. 561, 1839.

[25] W. Shockley and H. J. Queisser, "Detailed balance limit of efficiency of p-n junction solar cells," *Journal of applied physics*, vol. 32, no. 3, pp. 510–519, 1961.

[26] S. Rühle, "Tabulated values of the shockley–queisser limit for single junction solar cells," *Solar Energy*, vol. 130, pp. 139–147, 2016.

[27] A. G. Aberle, "Overview on sin surface passivation of crystalline silicon solar cells," *Solar energy materials and solar cells*, vol. 65, no. 1-4, pp. 239–248, 2001.

[28] J. Melskens, B. W. van de Loo, B. Macco, M. F. Vos, J. Palmans, S. Smit, and W. Kessels, "Concepts and prospects of passivating contacts for crystalline silicon solar cells," pp. 1–6, 2015.

[29] V. Boeisenko and S. Yudin, "Steady-state solubility of substitutional impurities in silicon," *physica status solidi (a)*, vol. 101, no. 1, pp. 123–127, 1987.

[30] F. A. Trumbore, "Solid solubilities of impurity elements in germanium and silicon," *Bell Labs Technical Journal*, vol. 39, no. 1, pp. 205–233, 1960.

[31] F. A. Wolf, A. Martinez-Limia, D. Grote, D. Stichtenoth, and P. Pichler, "Diffusion and segregation model for the annealing of silicon solar cells implanted with phosphorus," *IEEE Journal of Photovoltaics*, vol. 5, no. 1, pp. 129–136, 2015.

[32] H. Wagner, A. Dastgheib-Shirazi, B. Min, A. E. Morishige, M. Steyer, G. Hahn, C. del Cañizo, T. Buonassisi, and P. P. Altermatt, "Optimizing phosphorus diffusion for photovoltaic applications: Peak doping, inactive phosphorus, gettering, and contact formation," *Journal of Applied Physics*, vol. 119, no. 18, p. 185704, 2016.

[33] M. Rüdiger, J. Greulich, A. Richter, and M. Hermle, "Parameterization of free carrier absorption in highly doped silicon for solar cells," *IEEE Transactions on Electron Devices*, vol. 60, no. 7, pp. 2156–2163, 2013.

[34] B. Deal and M. Sklar, "Thermal oxidation of heavily doped silicon," *Journal of the Electrochemical Society*, vol. 112, no. 4, pp. 430–435, 1965.

[35] "Growth kinetics of silicon dioxide," http://www.iue.tuwien.ac.at/phd/filipovic/node29.html#fig:oxidation_100_dry, accessed: 2017-11-02.

[36] B. E. Deal and A. Grove, "General relationship for the thermal oxidation of silicon," *Journal of Applied Physics*, vol. 36, no. 12, pp. 3770–3778, 1965.

[37] A. Stoffel, A. Kovacs, W. Kronast, and B. Müller, "Lpcvd against pecvd for micromechanical applications," *Journal of Micromechanics and Microengineering*, vol. 6, no. 1, p. 1, 1996.

[38] L. da Silva Zambom, D. G. Lantin, E. Onoda, and P. Verdonck, "Non-stoichiometric silicon oxide deposited at low gaseous n2o/sih4 ratios," *Thin solid films*, vol. 459, no. 1-2, pp. 220–223, 2004.

[39] R. E. Leoni, "An electrochemical capacitance-voltage technique for the determination of pseudomorphic high electron mobility transistor material parameters," 1995.

[40] U. Hashima, S. N. M. Bajuria, N. H. A. Halima, and B. Y. Majlisb, "Shallow junction determination and boron profiling using electrochemical capacitance-voltage (ecv)," *JURNAL FIZIK MALAYSIA*, vol. 30, no. 1-4, 2009.

[41] M. Udhayasankar, J. Kumar, and P. Ramasamy, "Chemical beam epitaxial growth of alinas and investigations of electrolytes for ecv profiling," *Journal of crystal growth*, vol. 268, no. 3-4, pp. 389–395, 2004.

[42] R. Hall, "Recombination processes in semiconductors," *Proceedings of the IEE-Part B: Electronic and Communication Engineering*, vol. 106, no. 17S, pp. 923–931, 1959.

[43] N. Rouhi, B. Esfandyarpour, S. Mohajerzadeh, P. Hashemi, M. Robertson, and K. Raffel, "Low temperature growth of silicon dioxide using hydrogenation assisted nano-crystallization and plasma enhanced oxidation," *Journal of Non-Crystalline Solids*, vol. 356, no. 20-22, pp. 1027–1031, 2010.

[44] N. Tomozeiu, "Silicon oxide (siox, 0&ltx&lt2): a challenging material for optoelectronics," in *Optoelectronics-Materials and Techniques*. InTech, 2011.

[45] M. Fitzsimmons, J. Eastman, M. Müller-Stach, and G. Wallner, "Structural characterization of nanometer-sized crystalline pd by x-ray-diffraction techniques," *Physical Review B*, vol. 44, no. 6, p. 2452, 1991.

[46] S. Hüfner, *Photoelectron spectroscopy: principles and applications*. Springer Science & Business Media, 2013.

[47] E. Kleimenov, "High-pressure x-ray photoelectron spectroscopy applied to vanadium phosphorus oxide catalysts under reaction conditions," 2005.

[48] F. Himpsel, F. McFeely, A. Taleb-Ibrahimi, J. Yarmoff, and G. Hollinger, "Microscopic structure of the sio 2/si interface," *Physical review B*, vol. 38, no. 9, p. 6084, 1988.

[49] J. Finster, D. Schulze, F. Bechstedt, and A. Meisel, "Interpretation of xps core level shifts and structure of thin silicon oxide layers," *Surface Science*, vol. 152, pp. 1063–1070, 1985.

[50] T. Jana, S. Mukhopadhyay, and S. Ray, "Low temperature silicon oxide and nitride for surface passivation of silicon solar cells," *Solar energy materials and solar cells*, vol. 71, no. 2, pp. 197–211, 2002.

[51] M. Kim and J. Lee, "Characterization of amorphous sic: H films deposited from hexamethyldisilazane," *Thin Solid Films*, vol. 303, no. 1-2, pp. 173–179, 1997.

[52] N. Nickel, "Hydrogen diffusion through silicon/silicon dioxide interfaces," *Journal of Vacuum Science & Technology B: Microelectronics and Nanometer Structures Processing, Measurement, and Phenomena*, vol. 18, no. 3, pp. 1770–1772, 2000.

[53] J. Oh, H.-C. Yuan, and H. M. Branz, "An 18.2%-efficient black-silicon solar cell achieved through control of carrier recombination in nanostructures," *Nature nanotechnology*, vol. 7, no. 11, p. 743, 2012.

[54] Y. Wang, X. Chen, and R. J. Hamers, "Atomic-resolution study of overlayer formation and interfacial mixing in the interaction of phosphorus with si (001)," *Physical Review B*, vol. 50, no. 7, p. 4534, 1994.

[55] S. Xiao and S. Xu, "High-efficiency silicon solar cells—materials and devices physics," *Critical Reviews in Solid State and Materials Sciences*, vol. 39, no. 4, pp. 277–317, 2014.

[56] L. Skuja, "Optically active oxygen-deficiency-related centers in amorphous silicon dioxide," *Journal of NON-crystalline Solids*, vol. 239, no. 1-3, pp. 16–48, 1998.

[57] W. Ying, Y. Mizokawa, Y. Kamiura, K. Kawamoto, and W. Yang, "The chemical composition changes of silicon and phosphorus in the process of native oxide formation of heavily phosphorus doped silicon," *Applied Surface Science*, vol. 181, no. 1-2, pp. 1–14, 2001.

[58] P. Pai, S. Chao, Y. Takagi, and G. Lucovsky, "Infrared spectroscopic study of sio x films produced by plasma enhanced chemical vapor deposition," *Journal of Vacuum Science & Technology A: Vacuum, Surfaces, and Films*, vol. 4, no. 3, pp. 689–694, 1986.

[59] J. Luna-López, J. Carrillo-López, M. Aceves-Mijares, A. Morales-Sánchez, and C. Falcony, "Ftir and photoluminescence of annealed silicon rich oxide films," *Superficies y vacío*, vol. 22, no. 1, pp. 11–14, 2009.

[60] M. L. Hitchman and J. Kane, "Semi-insulating polysilicon (sipos) deposition in a low pressure cvd reactor: I. growth kinetics," *Journal of Crystal Growth*, vol. 55, no. 3, pp. 485–500, 1981.

[61] P. Holloway, "Grain boundary diffusion of phosphorus in polycrystalline silicon," *Journal of Vacuum Science and Technology*, vol. 21, no. 1, pp. 19–22, 1982.

[62] A. Bentzen, A. Holt, J. Christensen, and B. Svensson, "High concentration in-diffusion of phosphorus in si from a spray-on source," *Journal of applied physics*, vol. 99, no. 6, p. 064502, 2006.